



universität
wien

DIPLOMARBEIT

Carbon Stars, Hydrostatic Models and Optical / Near Infrared Interferometry

Angestrebter akademischer Grad

Magister der Naturwissenschaften (Mag. rer. nat.)

Verfasser:	DI Stefan Schneiderbauer
Matrikel-Nummer:	9940129
Studienrichtung (lt. Studien- blatt):	Astronomie
Betreuer:	Ass. Prof. Dr. Josef Hron

Wien, im Oktober 2008

Contents

1	Introduction	5
1.1	Late Stellar Evolution - The Asymptotic Giant Branch (AGB)	5
1.1.1	AGB Stars	5
1.1.2	Carbon Stars	6
1.2	Modelling a Star - Hydrostatic Atmospheres	8
1.3	Interferometry	11
2	Aims of this Thesis	17
3	Carbon Stars with Interferometric Observations	18
3.1	List of Investigated Stars	18
3.2	CHARM Catalogue	20
3.3	Stars with Interferometric Observations	20
4	Fundamental Parameters of the Selected Stars	21
4.1	V460 Cyg	21
4.1.1	Photometric Data	21
4.1.2	Spectroscopic Data	21
4.1.3	Interferometric Data	22
4.1.4	Effective Temperature	22
4.1.5	Distance	25
4.1.6	Further Data	27
4.2	Z Psc	28
4.2.1	Photometric Data	28
4.2.2	Spectroscopic Data	28
4.2.3	Interferometric Data	28
4.2.4	Effective Temperature	28
4.2.5	Distance	30
4.2.6	Further Data	30
5	Hydrostatic Models	31
5.1	Filters	31
5.1.1	Intensity Distributions and Visibility Profiles - Narrow Band Filters	31
5.1.2	Influences of Different Filter Widths on the Intensity Distributions .	41
5.1.3	Intensity Distributions and Visibility Profiles - Broad Band K-Filter	44
5.2	Models and the HRD	52
5.3	Model Structure	53

6	Best-Fit Model	59
6.1	Interpolation of Spectra	59
6.2	V460 Cyg - Fit of ISO Spectrum	60
6.3	Model Spectra and Visible Spectra of V460 Cyg	69
6.4	Model Spectra and Visible Spectrum of Z Psc	75
6.5	V460 Cyg and Z Psc - Best-Fit Model	76
7	Comparing Observations and Models	78
7.1	V460 Cyg	78
7.2	Z Psc	82
8	Appendix	88
8.1	Interesting Stars for Further Studies	88
8.2	Abstract	93
8.3	Abstract - German	95

List of Figures

1.1	Scematic representation of an AGB star	7
1.2	Interference fringes of a point source.	12
1.3	Michelson fringe visibility	13
1.4	Idealized interferometer	14
1.5	Image plane and pupil plane interferometry	15
4.1	Observed visible spectra of V460 Cyg	23
4.2	ISO SWS spectrum of V460 Cyg	24
4.3	Visible spectrum of Z Psc	29
5.1	Narrow band filters	32
5.2	Intensity distributions of different models in some narrow band filters - I	34
5.3	Intensity distributions of different models in some narrow band filters - II	35
5.4	Intensities and visibilities of different models	37
5.5	Intensity distributions and visibility functions in different narrow band filters	38
5.6	Intensity distributions and visibility functions in the $3.775\mu\text{m}$ narrow band filter	40
5.7	Intensity distributions for different filter widths	42
5.8	Intensity distributions for different filter widths	42
5.9	Opacity sampling spectra	43
5.10	K-band filter transmission	44
5.11	Intensity distributions and visibility functions of the splitted K-band	45
5.12	Schematic sketch of the weighted filter transmission calculation	47
5.13	Differences between the different visibility calculations for the models with 2800 K and 3200 K	48
5.14	Differences between the different visibility calculations for the models with 2900 K and 3000 K	49
5.15	Influences of band-width smearing on the model visibility functions	51
5.16	HRD with AGB evolutionary tracks and our models	52
5.17	Profiles of the density, the Rosseland mean opacity, the temperature and the total gas pressure along the stars' radius	54
5.18	Spectral energy distributions of carbon stars	56
5.19	Profiles of the total gas pressure and the partial pressures of the diatomic molecules CO , CH , CN and C_2 along the stars' radius	57
5.20	Profiles of the total gas pressure and the partial pressures of the polyatomic molecules C_2H_2 , HCN , C_3 (and CO) along the stars' radius	58
6.1	Validation of the linear interpolation in temperature	61
6.2	Absorption bands and their sensitivity to the temperature and to the C/O ratio	63

6.3	Root mean square error calculated from differences between the interpolated models and the ISO-SWS spectrum	65
6.4	Comparison between the best-fit model and the ISO spectra	66
6.5	Models with different metallicities	68
6.6	Comparison between the Tereshchenko spectrum of V460 Cyg and the interpolated model spectra	71
6.7	RMSEs obtained from the differences between the interpolated models and the Tereshchenko observations of V460 Cyg	72
6.8	Comparison between the Barnbaum observations of V460 Cyg and the interpolated model spectra	73
6.9	RMSEs obtained from the differences between the interpolated models and the Barnbaum observations of V460 Cyg	74
6.10	RMSEs between the interpolated models and the visible spectrum of Z Psc	76
6.11	Comparison between the Barnbaum spectrum of Z Psc and the interpolated model spectra	77
7.1	Comparison between the model visibilities and the observed ones for V460 Cyg and Z Psc	79
7.2	Comparison between the visibility function of the best-fit model for V460 Cyg and the observed visibility for V460 Cyg	81
7.3	Spectrum of the best-fit model of V460 Cyg	81
8.1	ISO-SWS01 spectra of the investigated stars	91
8.2	Visible spectra of the investigated stars	92

Chapter 1

Introduction

1.1 Late Stellar Evolution - The Asymptotic Giant Branch (AGB)

The following section is mainly from the book "Evolution of Stars and Stellar Populations" from Salaris and Cassisi (2005, [61]).

1.1.1 AGB Stars

The AGB is an evolutionary sequence of stars with low and intermediate mass. It begins either for population I stars when they leave the red clump on the red giant branch (RGB) or for population II stars when they leave the horizontal branch in a Hertzsprung-Russel diagram.

The AGB phase begins when the Helium burning (3α -process) in the core region of the star stops due to Helium exhaustion. A core consisting of carbon and oxygen is formed in the center of the star. The Helium burning continues in a shell around this C/O core. The energy, which is set free in these thermonuclear reactions, leads to an expansion and a decrease in temperature of the star. The drop in temperature results in an extinction of the hydrogen burning shell. This phase is called the early AGB. Quiescent He-shell burning around an inactive C/O core is significant for this stadium.

There is an upper mass limit (M^{UP}) for stars that evolve on the AGB. For masses $M > M^{UP}$ carbon ignites in the C/O core. M^{UP} is a function of the electron degeneracy of the core and is influenced by the initial chemical composition. It varies from $4 M_{\odot}$ for a metallicity of $Z = 0.001$ to $8 M_{\odot}$ for a solar metallicity ($Z = 0,018$) and very metal poor objects. Stars with masses $M < M^{UP}$ enter the next evolutionary phase on the AGB, the so called thermal pulse asymptotic giant branch (TPAGB).

The He-burning shell is surrounded by the material which was formerly produced due to hydrogen burning (mostly helium). It moves continuously outwards in this layer until it reaches the hydrogen/helium discontinuity. The He-burning stops there. This marks the beginning of the second AGB phase, the TPAGB. The lack of the now missing radiation pressure of the thermonuclear reactions leads to a gravitational contraction and an associated increase in temperature and pressure of the layers, which are above the former H/He discontinuity. The contraction continues until the temperature is high enough to ignite hydrogen in a shell around the C/O core. The ashes of this hydrogen burning (helium) are enriched between the burning shell and the core. When this He-shell reaches a critical value (approximately $10^{-3} M_{\odot}$ for a core mass of $0.8 M_{\odot}$) it ignites again. Because of the small thickness of the shell a thermonuclear runaway (increasing

temperature leads to an increasing energy production rate) occurs. This is called the helium shell flash or thermal pulse. The released energy results in an expansion and cooling of the outer layers. The hydrogen burning shell is switched off a second time. The He burning shell moves outwards until it reaches the H/He discontinuity again. The scenario of contraction and following hydrogen burning restarts. The alternating between hydrogen- and He-shell-burning as described here can occur many times. The intensity of these pulses rises from pulse to pulse.

AGB stars are cool and very extended objects, reaching radii up to several $100 R_{\odot}$. Most of these stars are long period variables. Depending on the regularity of their lightcurves they are separated into Miras (M), semiregular (SRa and SRb) and irregular (Lb) variables). The large extension of these stars results in a low gravitational acceleration in the outer parts of the atmosphere. This leads in combination with dynamic phenomena like pulsation and shock fronts to a high mass loss rate of these stars. Hence AGB stars are important for the enrichment of the ISM with heavy elements. The heavy elements are transported in convection zones from the interior of a star to the surface. This process is called dredge up and is explained in detail in the next section. Due to the mass loss AGB stars can lose a high amount of their initial mass. This explains the fact that most of the observed white dwarfs show masses of about $0.6 M_{\odot}$. Another effect of mass loss is the formation of circumstellar gas and dust shells around these stars.

The mass loss results in a mass decrement of the hydrogen rich envelope. The hydrogen burning shell is switched off when the envelope mass decreases below a critical value. The star leaves the AGB and develops towards hotter temperatures. The following gravitational contraction leads direct or about detours (e.g. born again AGB scenario) to one of the endproducts of stellar evolution - a white dwarf.

Radius	200 – 600 R_{\odot}
effective temperature	2500 – 3500 K
luminosity	$M_{bol} < -7.5$ mag, $10^3 - 10^4 L_{\odot}$
mass loss rates	$10^{-8} - 10^{-4} M_{\odot}/\text{year}$ ^a
variability period	30 – 2800 days
AGB timescale	$\approx 5 \cdot 10^6$ years

Table 1.1: Typical global parameters of AGB stars.

^ae.g. Schöier & Olofsson (2001, [62]), Groenewegen et al. (2002a,b, [26])

1.1.2 Carbon Stars

Some phenomena occur in combination with the thermal pulses which change the chemical composition of the star's atmosphere: A convection zone is formed after the thermal pulses (Fig. 1.1). It mixes the interior of the star with the atmosphere. This convective region could penetrate deeper in the star and exceed the H/He discontinuity when the hydrogen burning shell is switched off. If the convective envelope extends deep enough into the intershell region, elements which were processed through the CNO cycle, products of He burning (carbon) and heavy s-elements, could be dredged up into higher layers. This enrichment of heavy elements at the star's surface due to the formation of large convection zones is called 3^{rd} dredge up. The thermal pulses are the driver of this 3^{rd} dredge up. The depth of penetration of the convective envelope in the star is correlated with the strongness of the thermal pulse (the greater the pulse, the deeper the convection zone penetrates in).

The main effect of this dredge up is that carbon is transported into the atmospheres. All available carbon is fixed in the CO molecule at the beginning of the TPAGB because of the high binding energy of the CO molecule. There is more oxygen than carbon on the surface of a star at the beginning of the TPAGB. Hence, the remaining free oxygen atoms are available for other chemical bonds. When the carbon/oxygen ratio (C/O) is smaller than one, i.e. less carbon than oxygen is on the surface, an oxygen dominated chemistry is predominant. The absorption features of CO , TiO , VO , SiO , CO_2 and H_2O can be observed in spectra of these stars, which are M- and K-type giants.

Each thermal pulse may result in an enrichment of carbon at the surface due to convection. The amount of oxygen in the atmosphere remains roughly constant during the AGB phase. This results in an increasing C/O ratio with an increasing age on the TPAGB. At some point the C/O ratio may exceed the value one ($C/O > 1$). This means that more free carbon is available in the atmosphere than oxygen (because the oxygen is bound in CO). Now a carbon dominated chemistry prevails in the atmosphere. The molecules which dominate the spectra at $C/O > 1$ are CO , C_2 , CN , HCN , C_3 and C_2H_2 . Stars with $C/O > 1$ are called carbon stars. The structure of an AGB star with the distinction between oxygen and carbon rich is shown in Fig. 1.1.

An interesting fact about carbon stars is that very luminous carbon stars have not been observed until now. This was also called the carbon star mystery (Iben (1981, [34])). The solution of this mystery is that the bottom of the convective envelope is hot enough for running the CNO cycle. C^{12} is first converted into C^{13} (the relative amount of ^{12}C is decreased in the convective envelope) and then into N^{14} . This process is called hot bottom burning (HBB, e.g. Marigo et al. (1998, [48] and references therein)). Another effect of HBB is that the surface luminosity increases significantly (the core-mass/luminosity relation is broken).

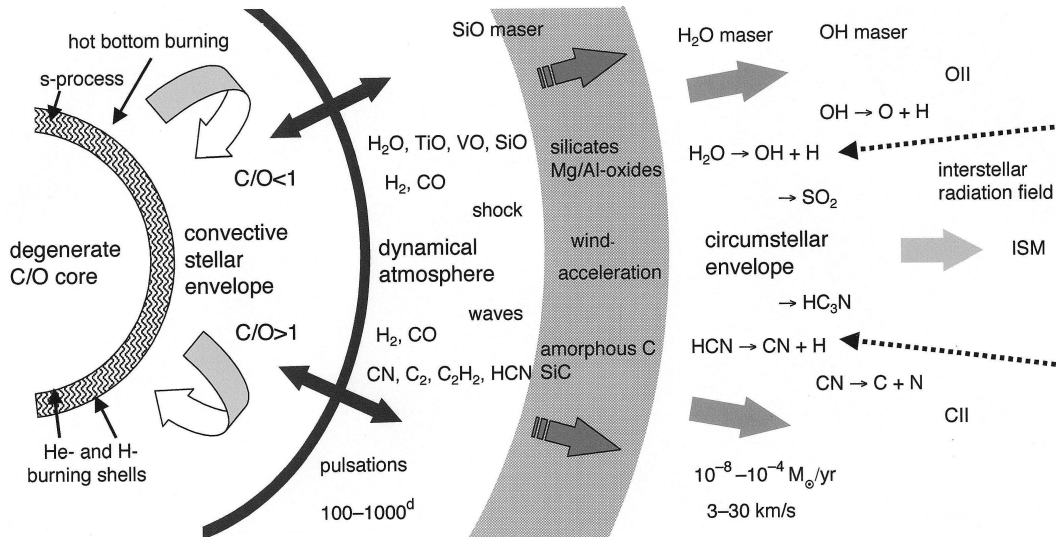


Figure 1.1: Schematic representation of an AGB star. 4 main parts can be identified: 1.) The degenerate C/O core. 2.) The convective envelope with the distinction between oxygen rich $C/O < 1$ and carbon rich $C/O > 1$. 3.) The dynamical atmosphere containing the typical molecules (carbon dominated chemistry for $C/O > 1$ and oxygen dominated chemistry for $C/O < 1$) and the pulsation period in the range of 100 up to 1000 days. 4.) The stellar wind. Figure taken from Habing & Olofsson (2003, [30]).

1.2 Modelling a Star - Hydrostatic Atmospheres

The following overview on modelling stellar atmospheres is mainly from chapter 4 (Atmospheres of AGB Stars written by Bengt Gustafsson and Susanne Höfner) in the book Asymptotic Giant Branch Stars (Habing & Olofsson (2003, [30])).

The basic equations are the equations of hydrodynamics and the energy equations. The Euler equation (momentum equation or the equation of motion) reduces in the hydrostatic case (assuming radially symmetric and homogenous stratified layers) to

$$\frac{\partial p_{gas}}{\partial r} = -G\rho\frac{M}{r^2} + \frac{1}{c} \int_0^\infty \chi_\nu \mathbf{F}_\nu d\nu, \quad (1.1)$$

where p_{gas} is the gas pressure, G the gravitational constant, r the radius, ρ is the mass density, M the mass, c the speed of light and the last term on the right is the radiation pressure (χ_ν is the extinction coefficient per unit length, $\chi_\nu = \kappa_\nu + \sigma_\nu$, where κ_ν is the true absorption coefficient and σ_ν is the continuous scattering coefficient) and F_ν is the net radiative energy flux. Equ. 1.1 is the hydrostatic equilibrium equation with an extra term which contains the radiation force. The specific intensity I_ν integrated over all directions n leads to the net radiative flux F_ν :

$$F_\nu = \oint_{\Omega} I_\nu(n) n d\omega \quad (1.2)$$

The energy equation in the hydrostatic case can be simplified as follows: The terms containing derivatives with respect to time and the terms containing the velocity are zero. The resulting equation is then equal to the condition of radiative equilibrium. It is the difference between radiative heating by absorption and cooling by emission. This difference is zero for hydrostatic equilibrium:

$$\int_0^\infty \chi_\nu (J_\nu - S_\nu) d\nu = 0, \quad (1.3)$$

where J_ν is the radiative mean intensity and S_ν is the source function ($S_\nu = \eta_\nu/\chi_\nu$, η_ν is the emissivity).

The equation of radiation transport in the time independent and spherically symmetric case can be written as

$$\left(\mu \frac{\partial}{\partial r} + \frac{1 - \mu^2}{r} \frac{\partial}{\partial \mu} \right) I(r, \mu, \nu) = \eta(r, \mu, \nu) - \chi(r, \nu) I(r, \mu, \nu) \quad (1.4)$$

where $\mu = \cos(\theta)$. θ is the angle between the line of sight and the connecting line from the stellar centre to the point where the radiation transport is calculated. The connection between the radiative mean intensity J_ν and the specific intensity I_ν is

$$J_\nu = \frac{1}{4\pi} \int I_\nu d\Omega, \quad (1.5)$$

where Ω is the solid angle. I_ν , J_ν and F_ν is obtained from Equ. 1.4 and 1.2.

The last required equations describe the microscopic state of the gas. They are called rate equations. There is one equation for each atomic or molecular transition. Considering the electronic transitions in atoms and the electronic, vibrational and rotational transitions in molecules this results in a huge number of coupled equations. They could be

solved numerically in many realistic cases. The system of rate equations for the condition of statistical equilibrium is

$$\sum_{j \neq i} (n_j R_{ji} + n_j C_{ji} - n_i R_{ij} - n_i C_{ij}) = 0, \quad (1.6)$$

where n_i are the populations for each atomic/molecular state i of the gas, R_{ij} and C_{ij} are the radiation and collision-induced transitions from any state i to any state j , $j \neq i$. The extinction coefficient χ , the emissivity η and the source function S_ν can be calculated with these rate coefficients. The R_{ij} terms couple the rate equations (Equ. 1.6) to the equation of radiation transport (Eqs. 1.5 and 1.4):

$$R_{ij} = 4\pi \int_0^\infty \alpha_{ij}(\nu) \frac{J_\nu}{h\nu} d\nu, \quad (1.7)$$

where α_{ij} is the absorption cross section and h is the Planck constant.

The collision induced transitions C_{ij} are:

$$C_{ij} = n_c \int_{v_0}^\infty \sigma_{ij}(v) v f(v) dv, \quad (1.8)$$

where n_c is the number density of particles under consideration, σ_{ij} is the cross section and v is the relative velocity between the atoms/molecules under consideration. Elastic collisions dominate between the particles in AGB atmospheres. Therefore, the velocities of the particles are assumed to have a Maxwellian velocity distribution ($f(v)$).

The Eqs. 1.1, 1.3, 1.4 and 1.6 must be solved together. This is despite the assumption of hydrostatic equilibrium not trivial because of the high number of radiative transitions especially in cool stars.

In practice two major problems occur when producing a grid of hydrostatic model atmospheres:

1. The first is to get atomic and molecular data of high quality and completeness (the absorption coefficients are calculated with these data). Molecules dominate the spectra and structure of AGB atmospheres. The typical number of absorption lines per molecule is in the range of $10^5 - 10^7$. The line strength and the position of these lines is derived either from quantummechanics or from laboratory measurements under terrestrial conditions (or with a combination of both of them). Hence, the accuracy of this data are often very limited (Aringer (2005, [2])).
2. The second problem is the treatment of the radiation field. Several 1000000 frequency points are required to get a fully resolved spectrum. This implicates a long computing time to solve the radiative transfer. Therefore a statistical treatment of the opacities is required to reduce the number of frequency points (and hence the computing time) in the calculation. There are two different approaches to do this: The first is called the opacity distribution function (ODF, e.g. Jørgensen (1992, [37])) and is used for F, G and K stars (and therefore not discussed here). The second one is the opacity sampling (OS) method (e.g. Jørgensen (1992, [37])) and is mainly used for cool stars (because in cool stars the opacities show different wavelength dependencies at different atmospheric depths). The OS method is a statistical approach where for each individual spectral line a detailed line profile can be taken into account. The line opacity is sampled in a fine grid of wavelength points. Opacity tables can then be constructed at the sampling wavelengths for every used species. The radiative transfer is calculated with these opacity tables at each sampling point and further on the other equations can be solved numerically.

Further problems in modelling AGB stars are that most of the stars are extended and pulsating. This involves phenomena like shock waves, mass loss and the formation of dust particles, which can not be treated within hydrostatic models. Models which include these hydrodynamical phenomena are described in e.g. Fleischer et al. (1992, [23]) or Höfner and Dorfi (1997, [33]). Sphericity effects cannot be neglected because of the star's large extension. The limit for plane parallel atmospheres is $R_{tot}/R_* \approx 1.05$ in models (where R_{tot} is the radius in molecular bands and R_* is the radius in the continuum). This ratio R_{tot}/R_* reaches values up to 1.4 in AGB stars (Scholz and Takeda (1987, [63])). Even the assumption of sphericity in a 1-dimensional approach is somewhat problematic due to the formation of large convection cells (e.g. Freytag et al (2002, [24])) in AGB stars.

Spherical hydrostatic model atmospheres are completely described by four parameters: Effective temperature T_{eff} , mass M , gravitational acceleration g (often expressed in logarithmic values) and the chemical composition. A model grid can be produced by a systematic variation of one of these parameters (the other 3 parameters are fixed).

MARCS Code

The MARCS (Model Atmospheres in a Radiative Convective Scheme) code is a code to model the atmospheres of cool stars (Gustafsson et al. (1975, [29])). It is fully self-consistent and the relevant variables are computed under the assumption of hydrostatic equilibrium, local thermodynamic equilibrium and chemical equilibrium. Convection is described over a local mixing length theory (Heney et al. (1965, [32])). Microturbulent velocity, which leads to line broadening, is considered within the OS. The original MARCS code was developed to deal with plane parallel stratifications.

An updated version of the MARCS code is used for the models in this thesis. This code is able to compute spherical models (Jørgensen et al. (1992, [38]), Plez et al. (1992, [56])). The spherical radiative transfer routines are taken from Windsteig et al. (1997, [74]). The treatment of the absorption is performed with the OS technique. The model calculation is done with approximately 5000 sampling points at 71 depth layers covering an opacity range of $\tau_{Ross} \approx 10^{-5}$ to 10^2 . τ_{Ross} is the Rosseland mean opacity and is defined as a weighted mean of the opacity κ_ν with the weight function dB_ν/dT over all frequencies. The frequencies are weighted stronger at a larger radiation flux:

$$\frac{1}{\kappa_R} = \frac{\int_0^\infty \frac{1}{\kappa_\nu} \cdot \frac{dB_\nu(T)}{dT} d\nu}{\int_0^\infty \frac{dB_\nu}{dT}}, \quad (1.9)$$

where κ_ν is the opacity at the frequency ν , B_ν is the Planck function and T is the temperature.

The input data to calculate the radiative transfer are computed with the COMA program (Aringer et al. (2000, [3])). COMA stands for Copenhagen Opacities for Model Atmospheres. COMA calculates the wavelength dependent absorption coefficients and weighted mean opacities. For a given temperature pressure (or density/pressure) structure, the abundances (and the partial pressures) of many molecules, atoms and ions are computed assuming chemical equilibrium. The partial pressures are then used to determine the continuous line opacities at each frequency point. COMA consists of three parts:

1. Chemistry: Two different methods are used to calculate the chemical equilibrium.
 - (a) The first one is the classical approach from Tsuji (1973, [70]). Therein, the equilibrium constant for every chemical reaction is described with a polynomial. The resulting system of equations is then solved numerically.

- (b) The second one is called GEM (Gibbs Energy Minimization (Falckesgaard (2001, [22])), which describes the free energy of each reaction. This approach tries to minimize the energy of the whole system.
2. The scattering and continuous opacities are calculated with routines corresponding to the MARCS code.
 3. The molecular opacities can be taken from:
 - (a) a direct calculation from the linelists.
 - (b) the OS data.

The molecules that are involved in the model calculations are listed in Cristallo et al. (2007, [15]).

With COMA, opacity tables can be calculated for each chemical abundance. The model atmospheres are then computed with COMARCS. The opacities between the opacity tables are therein calculated with a two-dimensional spline interpolation (in temperature and pressure).

COMARCS atmospheres are also used to produce synthetic opacity sampling spectra (R=10000). The therefore required opacities are again computed with COMA. The stellar flux at each wavelength is then obtained with these opacities and radiative transport routines from Windsteig et al. (1997, [74]).

1.3 Interferometry

The following section is mainly adopted from the PhD thesis of Verhoelst (2005, [73]) and from the Course Notes from the 1999 Michelson Summer School (Lawson (1999, [46])).

The theoretically attainable resolution of a telescope is given by the Rayleigh criterion $\theta = 1.22 \cdot \lambda / D$, which corresponds to the distance from the maximum to the first minimum of the Airy-function (θ is the angular resolution in radians, λ is the wavelength and D is the aperture diameter of the telescope). Thus the resolution of a 10 m telescope at a visible wavelength (e.g. at $0.5 \mu\text{m}$) is 13 mas (mas stands for milliarcseconds). The biggest stars show an angular extension of only a few 10 mas. The star with the largest photospheric angular diameter is α Ori (Betelgeuze) with 43.21 mas in the K-band filter at $2.2 \mu\text{m}$ (Perrin et al. (2004, [53])). From this it follows that we can hardly resolve stars even if we use the nowadays biggest telescopes. Note that θ is only a physically reachable lower limit for earth-bound observations. Turbulent effects in the earth's atmosphere result in much lower resolutions.

It is possible to reach higher resolution with the technique of interferometry. Following Thomas Young's 2-slit experiment (1807) a superposition of monochromatic light of two or more apertures (in astronomy: telescopes) results in an interference pattern (fringes). These fringes contain some information of the observed object. When the incoming wave front originates from a monochromatic point the fringes show a contrast of 1 at the focal plane of the optical system. This means that the source is unresolved. The interference fringes of an unresolved monochromatic source are shown in Fig. 1.2. There, the light (the wavefront is assumed to be orthogonal to the optical axis of the system) from the source passes the 2 slits (diameter D) at the distance B and is then focussed through a lens to produce a superposition of the light from the 2 slits at the focal plane. The intensity distribution of this superposition (interference fringes) is shown in Fig. 1.2. The envelope airy function (with the first zero points at a distance of $1, 22 \cdot \lambda / D$ from the optical axis)

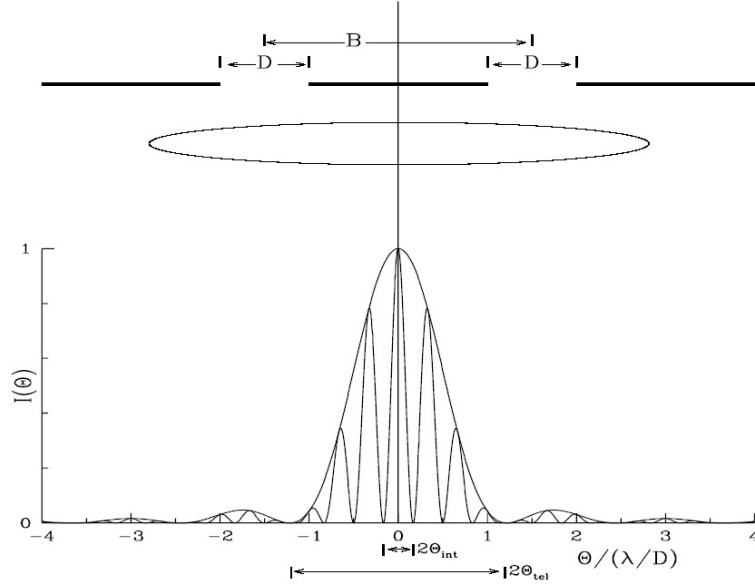


Figure 1.2: Interference fringes of a point source. The envelope interference fringes result from the diffraction limit of a single aperture (resolution $\Theta_{tel} = 1,22 \cdot \frac{\lambda}{D}$). The fringes inside this envelope result from the beam combination of the two apertures (resolution of the interferometer $\Theta_{int} = 1,22 \cdot \frac{\lambda}{B}$). Figure taken from Lawson (1999, [46]).

results from the diffraction at the edge of one slit (or aperture). The interference fringes inside this envelope result from the superposed waves. Therefore they have their first zero point at a distance of $1,22 \cdot \lambda/B$ to the optical axis.

The maxima of the interference fringes have the same intensities as the envelope airy function at equal distances to the optical axis. They have a contrast of 1. This is only the case for a plane parallel (a point source at infinity), monochromatic wave front. A deviation of a plane parallel wave front produces fringes with lower contrast. The maxima of these interference fringes are lower than the intensities of the envelope airy function and the minima have intensities higher than zero. Fringes with a contrast lower than 1 can either come from an extended source or from a non-monochromatic source. A source which is totally resolved through the interferometer has the contrast zero and therefore shows no interference pattern.

A star's angular diameter can be determined by measuring this contrast under the assumption of a monochromatic filter. Michelson (1920, [50]), for instance, defined the contrast (the Michelson fringe visibility V_M) of the interference fringes (Fig. 1.3) produced from the Michelson interferometer as follows:

$$V_M \equiv \frac{P_{Max} - P_{Min}}{P_{Max} + P_{Min}}, \quad (1.10)$$

where P_{Max} and P_{Min} are the measured maximum and minimum power of the interference fringes. Unresolved sources show a Michelson visibility of one because P_{Max} corresponds with the full received power ($2AF$ in Fig. 1.3) and P_{Min} is zero. An extended source, which is resolved by the interferometer, shows interference fringes with lower contrast and therefore a visibility < 1 .

The relation between the interference pattern and the observed light is expressed in the Van Cittert Zernike theorem: It states, that *the contrast and phase of the interference pattern, i.e. the complex visibility, corresponds to the Fourier transform of the source intensity distribution on the sky at the spatial frequencies corresponding to the baseline*

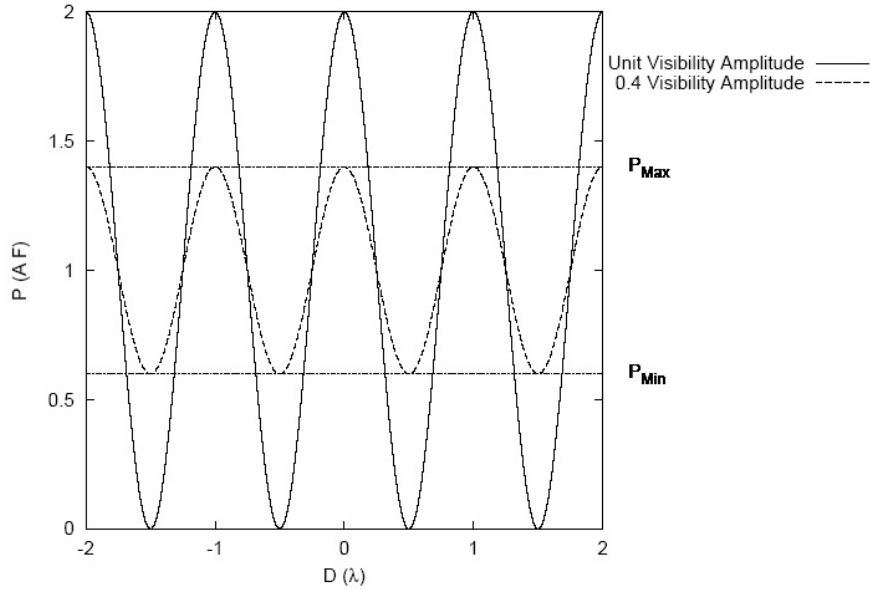


Figure 1.3: Michelson fringe visibility. P is the detected power and $D(\lambda)$ is distance to the optical axis. The solid line shows an unresolved source ($V_M = 1$) and the dashed line shows a resolved source with a visibility lower than 1. Figure taken from Lawson (1999, [46]).

projected to the sky (Verhoelst (2005, [73], p. 16)).

The spatial frequencies are Fourier space coordinates and defined in terms of B/λ , where B is the on the sky projected baseline (the distance between the two telescopes). They are most often expressed in 1/arcseconds in astronomy. The relation between the visibility and the source intensity distribution (Van Cittert Zernike theorem) is given by the following Fourier-transform:

$$\nu(u, v) = \int d\alpha d\beta A(\alpha, \beta) F(\alpha, \beta) e^{-2\pi i(\alpha u + \beta v)}, \quad (1.11)$$

where $\nu(u, v)$ is the complex visibility (which has the dimension of power), $u = B_x/\lambda$ and $v = B_y/\lambda$ are the spatial frequencies, B_x and B_y are the on the sky projected baselines in the x and y directions. α and β are the spatial coordinates on the sky, A is the aperture and F is the source intensity distribution. For an exact derivation of Equ. 1.11 see, for example, Lawson (1999, [46]). The visibility value at a spatial frequency of zero only depends on the source net flux. For this reason and for a better comparability normalized visibilities are used in astronomy:

$$V(u, v) = \frac{\nu(u, v)}{\nu(0, 0)} \quad (1.12)$$

Circular Symmetry

In this thesis circular symmetric models are used. This simplification, which is most often close to reality for stars, allows a simpler calculation of the visibility (Equ. 1.11). The 2 spatial coordinates (u, v) can be replaced by one for radial symmetry. This is the distance to the optical axis ρ :

$$\rho = \sqrt{\alpha^2 + \beta^2} \quad (1.13)$$

The spatial frequency is:

$$r = \sqrt{u^2 + v^2} \quad (1.14)$$

The visibility normalized with the total flux reduces to

$$V(r) = \frac{\int_0^\infty I(\rho) J_0(2\pi\rho r) \rho d\rho}{\int_0^\infty I(\rho) \rho d\rho}, \quad (1.15)$$

where $V(r)$ is the normalized visibility, $I(\rho)$ is the intensity profile of the star and J_0 is the 0th order Bessel function of the first kind. A derivation of Equ. 1.15 can again be found in Lawson (1999, [46]). Equ. 1.15 is a so called Hankel transform. Mathematically, it is a 2-dimensional Fourier transform of an axialsymmetric function.

The intensity distribution of a star can be obtained from model calculations (see Sec. 1.2). The visibility can then be calculated as a function of the spatial frequency with Equ. 1.15.

Astronomical Interferometers

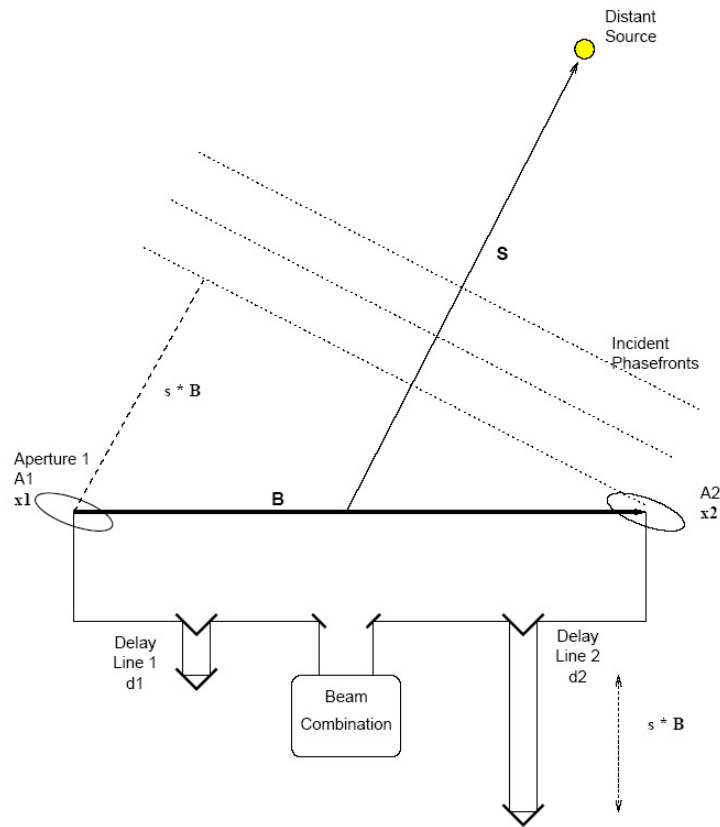


Figure 1.4: Idealized Interferometer. A1 and A2 are the telescope apertures. The delay lines d1 and d2 compensate a phase difference to reconstitute temporal coherence. The phase differences ($s \cdot B$) are produced from an off axis source. Figure taken from Lawson (1999, [46]).

An astronomical interferometer consists of at least two light collecting apertures (A1 and A2 in Fig. 1.4), which are located at an adjustable distance (baseline B). This baseline, which is used in the spatial frequency calculation, changes due to the rotation of the earth. That's because the on the sky projected baseline is used in the visibility calculation.

The apertures A1 and A2 collect the light of the distant source. The collected light is then transported to the beam combination. If the incident phase fronts of the observed source are not parallel to the baseline of the interferometer (this is the case when the source is off the optical axis), equal phase fronts arrive later at one aperture (in Fig. 1.4 this is the aperture A1; the additional distance is $s \cdot B$). This delay results in a phase difference of

the collected light between the two apertures. Adjustable delay lines are located between the beam combiner and the apertures to compensate this phase differences. In Fig. 1.4, the delay line 2 compensates the phase differences.

The next element in an interferometer is the beam combination. In astronomical interferometry there are two methods to do this::

- Image-plane interferometry or Fizeau interferometry (left graph in Fig. 1.5): The images of the two apertures are superposed to produce interference fringes.
- Pupil-plane interferometry or Michelson interferometry (right graph in Fig. 1.5): There, the parallel beams of the apertures are superposed (e.g. with a half silvered mirror). Each resulting beam is then focussed on a detector with one pixel.

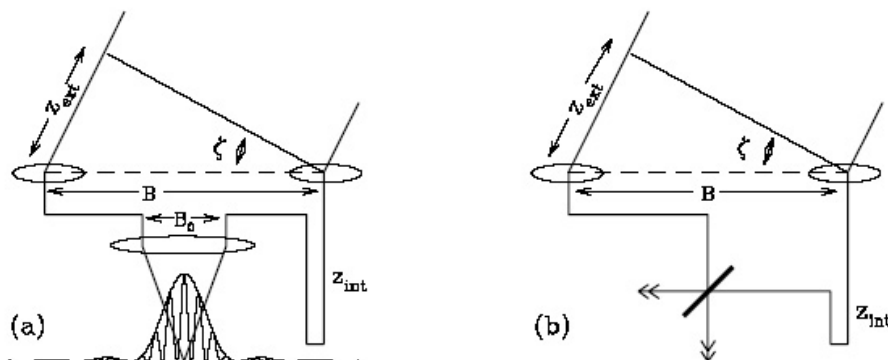


Figure 1.5: Image plane (left) and pupil plane (right) interferometry. Figure taken from Lawson (1999, [46])

When the two light beams of each telescope are combined, an interferometer measures one component of the spatial frequency spectrum (i.e. the visibility function) of the object's intensity distribution. This means that measuring at one baseline (one spatial frequency B/λ) leads to one corresponding visibility value. If the distance between the two telescopes can be changed, further visibility values at different spatial frequencies are obtained and the visibility function can be approximated. This observed visibility function can then be compared to calculated ones (Equ. 1.15) and it can be verified how good the model describes the intensity distribution of the star.

The following itemization gives examples of the results which were obtained with the technics of astronomical interferometry (this summary is from the book 'An Introduction to Optical Stellar Interferometry' (Labeyrie et al. (2006, [44]))):

- *Measuring stellar diameters and the limb darkening of stars with long-baseline interferometry.* The angular diameter of a star could be calculated by fitting a well known visibility function (e.g. a uniform disk, a limb darkened disk or a Gaussian disk) to the observed visibility. If the distance to the star is known, the diameter of the star can easily be calculated with

$$D = \Theta \cdot d, \quad (1.16)$$

where D is the star's diameter, Θ is the angular diameter and d is the distance.

- *To give an accurate estimation of the orbits of binarys.* If the distance to the system is known, the absolute masses of the components can be calculated.

- *Producing images of supergiant stars.* The resolution of these images is good enough to identify star spots.
- *Measuring the angular diameter change of nearby Cepheids* has been used to reduce the zero point error in the period luminosity relation.
- *Measuring the geometry of disks around giants, young stars and galactic nuclei.*

Chapter 2

Aims of this Thesis

In this thesis we test the consistency of two different approaches to describe carbon stars. The first method is the calculation of hydrostatic model atmospheres and the comparison of the corresponding synthetic model spectra to observed ones. The parameters of the best-fit model (the effective temperature, the mass, the gravitational acceleration and the chemical composition) can be determined by this approach. Another output of the model calculation in addition to the synthetic spectrum is the intensity distribution. It gives the wavelength dependent center to limb intensity variation which is needed for the second method.

The second method uses the interferometric observation of stars. The measured quantity is the visibility (or the squared visibility) which can be compared to computed visibility functions. The latter are obtained from the intensity distributions of the models. They are the Fourier transform of the source intensity distribution as a function of the spatial frequencies (Van Cittert Zernike theorem). The visibility function of the best-fit model from the spectroscopic approach calculation can then be compared to the observed visibility of a given carbon star.

The main question in this thesis is if carbon stars with low pulsation amplitude can be described with hydrostatic model atmospheres and how good the results from the model calculations agree with observed spectra and with interferometric measurements.

This thesis can be divided into four main parts:

- Searching for carbon stars with low pulsation amplitudes for which interferometric measurements exist (Ch. 3).
- Searching the literature for fundamental parameters and spectra of the stars identified above. These parameters are for example the effective temperature, the distance, the C/O ratio, the bolometric flux and interferometric quantities like the visibility and the corresponding spatial frequency (Ch. 4).
- Calculation of a hydrostatic model grid (Ch. 5). The fundamental parameters of the stars from Ch. 4 are used to get a first estimate of the required parameters for the model grid. The best-fit model is then obtained by a comparison between observed and model spectra (Ch. 6).
- The visibility function of the best-fit model is obtained from the intensity distribution of the star. The observed visibility can then be compared to the computed visibility function of the best fit model and checked for accordance (Ch. 7).

Chapter 3

Carbon Stars with Interferometric Observations

3.1 List of Investigated Stars

The smaller the variability amplitude of the star, the more the assumption of hydrostatic equilibrium is justified. For this reason our list of investigated carbon stars is limited by a maximum amplitude of 3 mag. The objects are taken from the AGB database (Kerschbaum (1993, [40])) and listed in Tab. 3.1. The amplitudes in this Table are either photographic ones or measured in the V- or B filter. The differences between these amplitudes are low for carbon stars. The last column gives some information about the availability of interferometric data (see Sec. 3.3 for details). In some cases only the angular diameter θ has been measured. For our study the visibility and the corresponding spatial frequency are required. Hence these stars could not be used further in this thesis.

GCVS	type	ampl. [mag]	spectrum	dist. [pc]	comments
AB Ant	Lb	0.10 [V]	C6,3(N0)	301.20	
AC Pup	Lb	1.20 [V]	C5,4(N)	353.36	
AQ And	SR	1.90 [P]	C5,4(NB)	12500.00	Vis + sp. Fr.
AQ Sgr	SRb	2.30 [P]	C7,4(N3)	4761.90	
AV Tr	Lb	0.70 [P]	C5,5(NB)	462.96	
AX Tr	Lb	1.38 [V]	C5,5(NB)	458.72	
BE CMa	Lb	1.30 [P]	C5,5J(N)	909.09	
BF Sge	Lb	1.80 [B]	C4,4(N3)		
BL Ori	Lb	1.80 [P]	C6,3(NB,TC)	398.41	only Θ available
CR Gem	Lb	1.20 [B]	C8,3E(N)	323.62	only Θ available
DR Ser	Lb	2.99 [B]	C6,4(N)	1694.92	
EL Aur	Lb	0.80 [P]	C5,4(N3)	207.90	
GK Ori	SR	1.50 [V]	C4-5,4-5(N)	480.77	
HK Lyr	Lb	1.80 [V]	C6,4(N4)	1369.86	only Θ available
HX Gem	Lb	1.50 [P]	C4,4(N)	78.00	
NP Pup	Lb	0.27 [V]	C7,2(N0)	418.41	
NQ Cas	Lb	0.92 [B]	C4,5J(R5)	1785.71	
RT Cap	SRb	2.80 [P]	C6,4(N3)	561.80	
RT Ori	SRb	2.10 [P]	C6,4(NB)	286.53	
RU Pup	SRb	1.90 [P]	C5,4(N3)	218.34	
RV Cyg	SRb	1.60 [P]	C6,4E(N5)	2439.02	Vis + sp. Fr.
RV Mon	SRb	2.19 [B]	C4,4-C6,2(NB/R9)	450.45	
RY Dra	SRb	1.97 [V]	C4,5J(N4P)	487.80	

GCVS	type	ampl. [mag]	spectrum	dist. [pc]	comments
RY Mon	SRa	1.70 [V]	C5,5-C7,4:(N5/R)	454.55	
S Set	SRb	1.27 [B]	C6,4(N3)	395.26	
ST Cam	SRb	2.80 [P]	C5,4(N5)	2777.78	
SX Sco	SR	0.90 [P]	C5,4(N3)	363.64	
SY Eri	SRb	1.00 [P]	C6,3(N0)		
T Cnc	SRb	2.90 [V]	C3,8-C5,5(R6-N6)	6666.67	
T Ind	SRb	1.70 [P]	C7,2(NA)	571.43	
T Lyr	Lb	1.76 [V]	C6,5(R6)	632.91	
T Mus	SRb	2.60 [P]	C(NP)	1724.14	
TT CVn	SRb	0.71 [B]	C3,5CH(R6P)		
TT Cyg	SRb	1.70 [B]	C5,4E(N3E)	510.20	only Θ available
TT Tau	SRb	2.00 [P]	C4,2-C7,4(N3)	1282.05	
TV Lac	Lb	0.80 [P]	C4,5(N3)	534.76	
TW Hor	SRb	0.43 [V]	C5,5J(R8)		
TW Oph	SRb	2.20 [P]	C5,5(NB)	280.11	
TX Psc	Lb	0.41 [V]	C7,2(N0)(TC)	233.10	not spherical
U Ant	Lb	1.60 [P]	C5,3(NB)	256.41	
U Aps	Lb	0.60 [P]	C(NB)	1694.92	
U Cam	SRb	1.80 [P]	C3,9-C6,4E(N5)	1265.82	
U Hya	SRb	2.40 [B]	C6.5,3(N2)(TC)	161.81	
UU Aur	SRb	2.17 [B]	C5,3-C7,4(N3)	555.56	
UV Aql	SRa	1.30 [P]	C5,4-5(N4)		
UX Cen	SRb	0.50 [P]	C(NB)	398.41	
UX Dra	SRa	1.16 [V]	C7,3(N0)	571.43	
V460 Cyg	SRb	1.43 [V]	C6,4(N1)	613.50	Vis + sp. Fr.
V1942 Sgr	Lb	0.26 [V]	C6,4(N2/R8)	396.83	
V Aql	SRb	1.80 [V]	C5,4-C6,4(N6)	370.37	
V Pav	SRb	1.90 [P]	C6,4(NB)	301.20	
VX And	SRa	1.50 [V]	C4,5(N7)	280.90	Vis + sp. Fr.
VY UMa	Lb	1.13 [V]	C6,3(N0)	347.22	
W CMa	Lb	1.55 [V]	C6,3(N)	2272.73	
W Sex	SR	2.20 [B]	C6,3E(NBE)	389.11	
WW Cas	Lb	2.60 [V]	C5,5(N1)	371.75	
WZ Cas	SRb	2.00 [P]	C9,2JLI(N1P)	787.40	
X Cnc	SRb	1.90 [V]	C5,4(N3)	1111.11	Vis + sp. Fr.
X Vel	SR	1.23 [B]	C4-5,4-5(NB)	526.32	
Y CVn	SRb	2.60 [P]	C5,4J(N3)	217.86	Vis + sp. Fr.
Y Pav	SRb	1.70 [P]	C7,3(N0)	362.32	
Y Tau	SRb	2.70 [V]	C6.5,4E(N3)	268.82	
Z Psc	SRb	1.30 [P]	C7,2(N0)	323.62	Vis + sp. Fr.

Table 3.1: List of the investigated stars. These carbon stars are selected from the AGB database (Kerschbaum (1993, [40])) up to a photographic, B or V amplitude of 3 mag. The GCVS name is the star's name in the general catalogue of variable stars, type is the variability type, ampl. is the amplitude (photometric amplitude...[P], measured in the V-filter...[V], measured in the B-filter...[B]), spectrum is the carbon star spectral classification, dist. is the distance and the last column gives some information about the interferometric data. The references for the comments are given in Sec. 3.3.

3.2 CHARM Catalogue

The search for stars with existing interferometric observations was performed using the CHARM 2 (Richichi (2005, [57])) catalogue. This is an updated version of the Catalog of High Angular Resolution Measurements (CHARM, Richichi & Percheron (2002, [59])). It includes direct measurements of stellar angular diameters, binary stars separations and the size of extended sources such as circumstellar shells or extragalactic systems. The observations listed were done using the techniques of lunar occultations, long baseline interferometry and it includes estimates by indirect methods (e.g. fits to spectrophotometric data). The data also include catalogs of interferometric calibrators. The CHARM catalog contains a total of 3238 unique sources. We went through this list and looked for those carbon stars with a photometric amplitude smaller than 3 mag. The carbon stars with interferometric measurements are the ones with a comment in the last column of Tab. 3.1.

3.3 Stars with Interferometric Observations

For the following carbon stars interferometric observations are listed in the CHARM catalogue:

- TX Psc: There is evidence that this famous carbon star shows significant asymmetries (Jørgensen et al. (2000, [36])). The assumption of spherical symmetry is therefore problematic. Visibility and corresponding spatial frequency are available in Dyck et al. (1996, [18]).
- AQ And and Z Psc: Visibility and spatial frequency are available in Dyck et al. (1996, [18]), Only the angular diameter Θ is published for these stars in Van Belle & Thompson (2000, [72]).
- RV Cyg, V460 Cyg, VX And and Y CVn: Visibility and corresponding spatial frequency are available in Dyck et al. (1996, [18]).
- X Cnc: Visibility and corresponding spatial frequency are available in Richichi & Calamai (2003, [58]).
- BL Ori, CR Gem, HK Lyr and TT Cyg: The "raw data" of interferometry, visibility and corresponding spatial frequency, could not be found in the literature. The angular diameter Θ is published for these stars in Van Belle & Thompson (2000, [72]).

The stars that are chosen to deal with in more detail in this thesis are V460 Cyg and Z Psc. This is because they have photometric amplitudes which seem to permit the assumption of hydrostatic equilibrium and because the interferometric data are available in appropriate form.

Chapter 4

Fundamental Parameters of the Selected Stars

The following section contains a detailed listing of the measurements of the parameters of V460 Cyg and Z Psc, which could be found in the literature. A comparison to the results of our work is given in Ch. 7.

4.1 V460 Cyg

V460 Cyg is a carbon star with the Yamashita (1972, [78]) spectral type C6,3. The first number in this classification scheme stands as in the Morgan Keenan classification for the temperature and the second one for the carbon abundance. It has the variability type SRb (data from the AGB database (Kerschbaum (1993, [40]))).

4.1.1 Photometric Data

The Tabs. 4.1 and 4.2 contain some photometric data in the visible and infrared spectral range and some bolometric fluxes of V460 Cyg. The bolometric fluxes are either derived from multiband photometry or from spectroscopic data.

B [mag]	V [mag]	J [mag]	H [mag]	K [mag]
8.682	5.992	1.802±0.220	0.583±0.192	0.270±0.184
F12 [Jy]	F25 [Jy]	F60 [Jy]	F100 [Jy]	
76.04	21.26	9.19	4.95	

Table 4.1: Photometric data of V460 Cyg, taken from the Simbad database. The J, H and K magnitudes are originally from the 2MASS All Sky Catalog of point sources (Cutri et al. ((2003), [16])). F12, F25, F60 and F100 are the colour corrected IRAS fluxes at 12, 25, 60 and 100 μm (taken from the AGB database (Kerschbaum (1993, [40]))).

4.1.2 Spectroscopic Data

Two spectra in the visible spectral range could be found in the literature (Fig. 4.1): Tereshchenko (1999, [65]) and Barnbaum (1996, [6]). The Tereshchenko spectrum was observed in the nights of September 2nd - 4th, 1986. The measured V-magnitude was 6.07 on the date of observation. The resolution is 50 \AA and the relative root mean square error is 2 - 5%. It covers a wavelength range from 3225 \AA to 7575 \AA .

F_{bol} [W/cm^2]:	[67]	[72]	[18]	[8]
	$1.25 \cdot 10^{-13}$	$1.113 \cdot 10^{-13}$	$1.45 \cdot 10^{-13}$	$1.32 \cdot 10^{-13}$

Table 4.2: Bolometric fluxes (F_{bol}) of V460 Cyg. The numbers in the squared brackets give the references from which the data were taken ([67]...Tsuji (1981), [72]...VanBelle & Thompson (2000), [18]...Dyck et al. (1996), [8]...Bergeat et al. (2001)).

The Barnbaum spectrum (3993 - 7019 Å) was observed with the Shane (3m) telescope and the Kast spectrograph at Lick observatory in the night of September 4th - 5th, 1994. The resolution is 1.6 Å at 4000 - 5000 Å.

Another spectrum in the short infrared wavelength range was found in Lazaro (1994, [47]). Because of the very low resolution, this spectrum is not used further in this thesis.

Infrared Space Observatory (ISO)

Two low resolution spectra of V460 Cyg, which were observed with the Infrared Space Observatory (Kessler et al. (1996, [41])) are available on the ISO data archive. The used spectrograph was the Short Wavelength Spectrometer (SWS, de Graauw et al. (1996, [17])) in the operation mode 01.

The spectrum which is used in this thesis was observed on November 1st, 1997 and published in Aoki et al. (1998, [5]). It is shown in Fig. 4.2). The covered wavelength range is 2.38 to 45,2 μ m. The on target time was 1140 sec. The resolution is $R \approx 200$

4.1.3 Interferometric Data

A visibility measurement of V460 Cyg could be found in Dyck et al. (1996, [18]). The observation took place at the Infrared and Optical Telescope Array (IOTA) on Mt. Hopkins in Arizona on July 10th, 1995. IOTA is a Michelson stellar interferometer, which consists of three 45 cm telescopes with a maximum reachable baseline of 38 m. A detailed description of the data reduction used to calculate the visibilities at the IOTA interferometer can be found in Carleton et al. (1994, [13]) or in Dyck et al. (1995, [20]). The obtained visibility value is 0.704 ± 0.051 at a corresponding baseline of 37.08 m. The derived uniform disc diameter is 6.3 ± 0.6 mas. The used filter was the K-broadband filter: $\lambda = 2.2 \mu$ m, $\Delta\lambda = 0.4 \mu$ m.

4.1.4 Effective Temperature

The effective temperature of a star is the temperature a blackbody with the same size and luminosity as the star would have. Knowing the radius of the star, the effective temperature can then easily be calculated following Stefan-Boltzmanns-law $F \propto T^4$:

$$T_{eff} = \left(\frac{L_{bol}}{4\pi\sigma R^2} \right)^{1/4}, \quad (4.1)$$

where T_{eff} is the effective temperature, L_{bol} is the bolometric luminosity, σ is the Stefan Boltzmann's constant and R is the radius of the star. The radius is normally defined where the Rosseland mean opacity is 1 or 2/3 and can therefore exactly only be determined from model atmospheres. In praxis it is determined from the uniform disc diameter and a small multiplicative factor (e.g. Dyck et al. (1996, [18]))

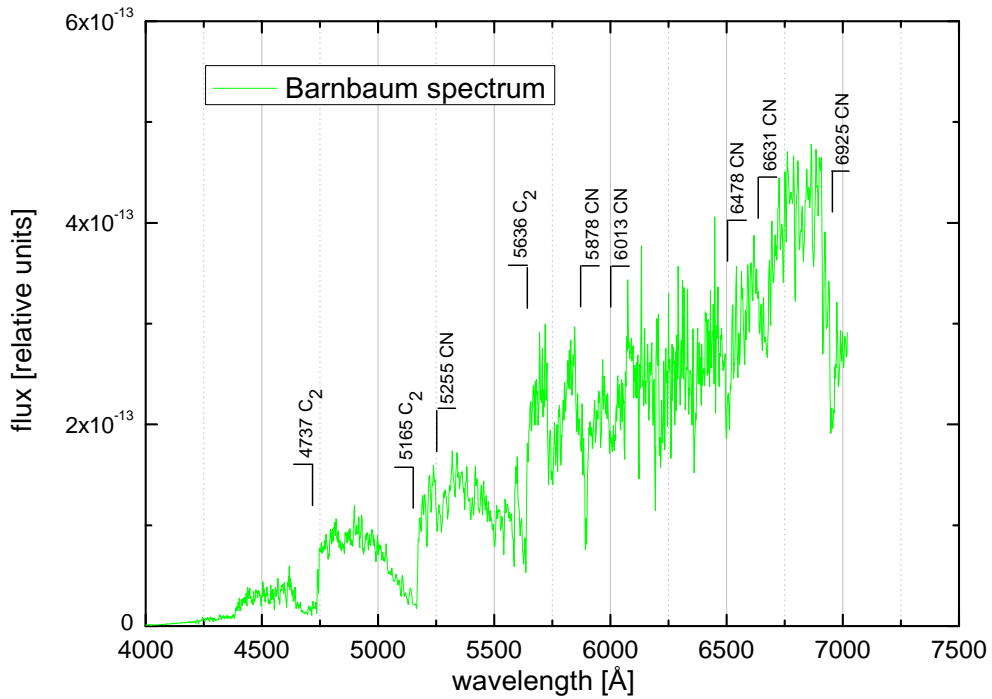
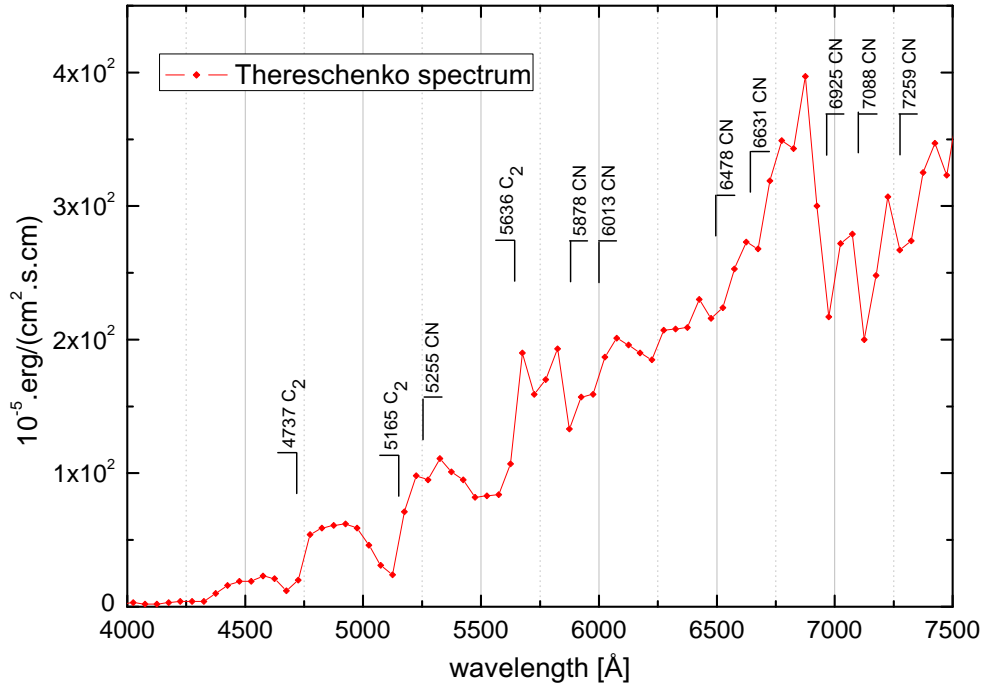


Figure 4.1: Observed Spectra of V460 Cyg from Tereshchenko (1999, [65], upper graph) and from Barnbaum (1999, [6], lower graph). Also indicated are the main absorption features of the molecules CN and C_2 , which are dominant in this spectral range.

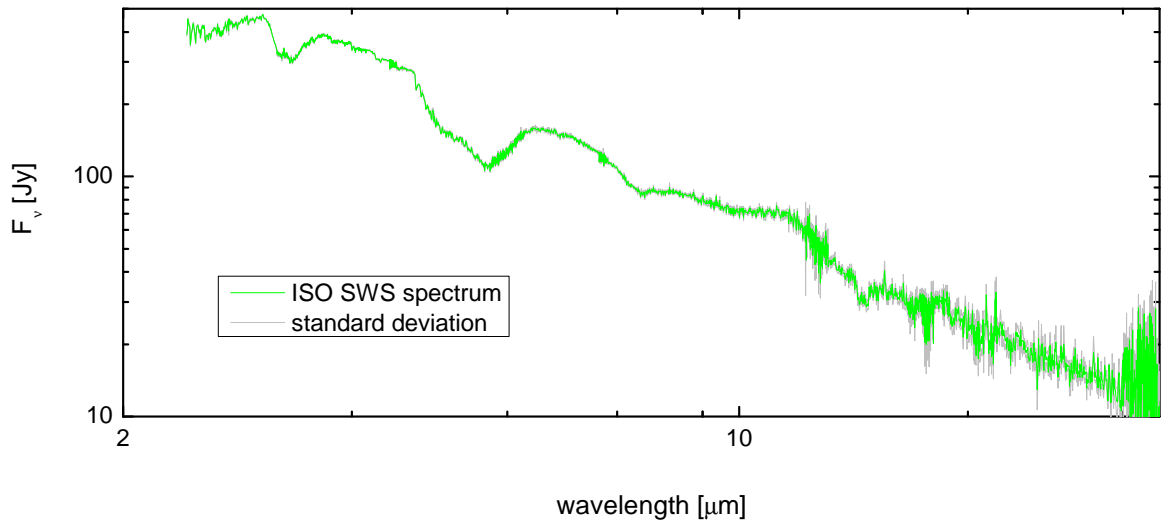


Figure 4.2: ISO SWS spectrum of V460 Cyg in the wavelength range from 2,38 to 30 μm . The standard deviation of the data is also shown (grey area). The spectrum was taken from the ISO data archive at the ESA homepage (<http://iso.esac.esa.int/ida/>).

The effective temperatures of V460 Cyg and Z Psc, which were found in the literature, have been estimated either by using the techniques of interferometry, lunar occultations, the infrared flux method, colour indices, bolometric fluxes, model atmospheres or by a combination of them. These different methods to estimate the temperature of stars are shortly explained in the following subsections.

Interferometry and Lunar Occultation

An observation involving interferometry (or lunar occultation) leads to the angular diameter of the star. If the distance to the star is known, this quantity can be converted into the radius. The angular diameter and thus the radius is wavelength dependent. This is because the opacity is also a function of the wavelength. Most interferometric measurements were taken in the K-band (2.2 μm). The advantages of the K-band given by the authors are (e.g. Dyck et al. (1996, [18]):

- In carbon stars, the wavelength of 2.2 μm lies near but on the Rayleigh Jeans side of the flux maximum.
- This band is little contaminated by dust emission. This assumption is based upon following considerations: Dust emission originates from circumstellar envelopes. Dust shells exist around many AGB stars. Because of the small grain sizes of the dust, the absorption and extinction is higher at shorter wavelengths (Tsuji (1978, [69])). Therefore, longer wavelengths should be preferred in interferometric observations. On the other hand, the thermal re-emission peak of a circumstellar dust envelope with a temperature of $< 1000\text{ K}$ lies at $> 3\ \mu\text{m}$ (Rowan-Robinson & Harris (1983, [60])). Hence, the wavelength to observe the star's photosphere should be between the optical wavelength range and $< 3\ \mu\text{m}$.

- The interstellar dust extinction at ($2.2 \mu\text{m}$) is ≈ 1 mag weaker than in optical wavelengths (Claussen et al. (1987, [14]).

The second parameter required to determine temperatures from interferometry is the bolometric luminosity. It can be obtained either from multicolor photometry or from a filter magnitude and the corresponding correction. Equation (4.1) can be rewritten with the usage of measurable quantities:

$$T_{eff} = 1.316 \cdot 10^7 \cdot \left(\frac{F_{bol}}{\theta_R^2} \right)^{1/4}, \quad (4.2)$$

where θ_R is the Rosseland mean angular diameter expressed in mas and F_{bol} is the bolometric flux expressed in W/cm^2 . This temperature calculation does not need a distance determination (except for the estimation of the interstellar reddening).

Infrared Flux Method

The infrared flux method (Blackwell & Shellis (1977, [11])) is a method to determine the effective temperature with the ratio of the bolometric flux to the one in a near infrared band (mostly the K-band). The IR flux method is calibrated with model atmospheres. It is applied to carbon stars by Tsuji (1981a, [67] and 1981b, [68]).

Model Atmospheres

One can find the best fitting model by comparing a grid of synthetic spectra with an observed one. The temperature of this best fitting model atmosphere is then the effective temperature of the star. Note that the spectral appearance of an object depends on many parameters (C/O , $\log(g)$, chemical abundances). The spectra depend on these parameters often highly non-linear and ambiguously. Hence, there could be more models with a different combination of the input parameters, that show a spectra similar to the observed one (see Ch. 6).

Another problem in modelling atmospheres is, at which radius the temperature is assigned to be the effective temperature of the star. The effective temperature of models is often defined as the temperature where the Rosseland mean opacity is unity (or 2/3).

The effective temperatures of V460 Cyg, which were found in the literature, are listed in Tab. 4.3.

4.1.5 Distance

A direct distance measurement (parallax from Hipparcos satellite) exists for V460 Cyg. Nevertheless, the parallaxes of objects such as carbon stars are affected with some uncertainties resulting from their relative large distance, their huge extension, the radius variation due to the pulsation of the stars and their red colors (e.g. Knapp (2003, [43])). The distances found in the literature are listed in Tab. 4.4.

T_{eff} [K]	$\sigma_{T_{eff}}$ [K]	Determination	Reference
2950	-	Combination of spectral energy (SED) distributions, color indices, model atmospheres and interferometry	Bergeat et al (2001, [8])
3000	-	^a SED and model atmospheres	Jørgensen et al. (2000, [36])
3100	-	^b SED and model atmospheres	Jørgensen et al. (2000, [36])
2900	-	^c SED and model atmospheres	Jørgensen et al. (2000, [36])
3160	160	Interferometry	Bergeat et al. (2001, [8])
2996	147	Interferometry	Van Belle & Thompson (2000, [72])
3112	-	bolometric fluxes and angular diameters	Ohnaka & Tsuji (1998, [51])
3230	-	Infrared flux method	Ohnaka & Tsuji (1996, [52])
3200	157	Interferometry	Dyck et al. (1996, [18])
2845	-	Infrared flux method	Tsuji (1981, [67])
2840	-	Total fluxes and interferometry	Mendoza & Johnson (1965, [49])

Table 4.3: The effective temperatures and their standard deviations ($\sigma_{T_{eff}}$) of V460 Cyg in the literature.

^abest fit model with $\log(g [\text{cm/s}^2]) = -0.5$ and $C/O = 1.2$

^bbest fit model with $\log(g [\text{cm/s}^2]) = -0.5$ and $C/O = 1.023$ or $\log(g [\text{cm/s}^2]) = -0.0$ and $C/O = 1.2$ (depending on which $K_P(C_3)$ value is chosen. The $K_P(C_3)$ value gives the equilibrium between atomic carbon, C_2 and C_3)

^cbest fit model with $\log(g [\text{cm/s}^2]) = -1.5$ and $C/O = 1.1$

distance [pc]	determination	Reference
613, 5	^a parallax	Perryman (1997, [55])
635	^b parallaxes and proper motions	Bergeat Chevallier (2005, [7])
230	^c period luminosity relation	Schöier and Olofsson (2001, [62])
480	^d $M(K) = -8.1$ mag	Claussen et al. (1987, [14])
449	^d mean luminosity $7500 L_{\odot}$	Blanco (2000, [12])

Table 4.4: The distances of V460 Cyg in the literature.

^aThe exact value of the parallax is 1.63 ± 0.73 . This corresponds to a minimum distance of 423.7 pc and a maximum distance of 1111.1 pc.

^bThis estimation combines the measured Hipparcos parallax and the proper motion of the carbon star. It is assumed that the star's proper motion decreases linearly with the distance. This implies a uniform velocity distribution of carbon stars. Hanson (1979, [31]) showed that this is close to reality.

^cThis estimation depends on the observed period luminosity relations (Groenewegen & Whitelock (1996, [28])) for AGB stars. V460 Cyg has a photometric amplitude in the V-filter of 1.43 mag. This distance estimation could be very uncertain due to the small amplitude of V460 Cyg (the period luminosity relation in this amplitude range is not well known).

^dThese two determinations depend on the observed fact that all carbon stars have similar absolute luminosities in the K-band. Measuring the apparent magnitude in this band leads in combination with a determination of the interstellar reddening to the distance of the carbon star.

4.1.6 Further Data

- Coordinates of V460 Cyg (from the Hipparcos catalogue, $eq = 2000$ (Perryman (1997, [55]))): right ascension $\alpha = 21h\ 42'\ 01.084''$, declination $\delta = +35\ 30'\ 36.72''$.
- C/O abundance ratio:
 - $C/O = 1.062$, from Lambert (1986, [45]), determination with near infrared spectra and model atmospheres.
 - $C/O = 1.2$ for the best fit model $T_{eff} = 3000\text{ K}$ and $\log(g [cm/s^2]) = -0.5$, from Jørgensen et al. (2000, [36]).
 - $C/O = 1.023/C/O = 1.2$ (depending on the which $K_P(C_3)$ value is chosen) for the best fit model $T_{eff} = 3100\text{ K}$ and $\log(g [cm/s^2]) = -0.5/\log(g [cm/s^2]) = 0.00$, from Jørgensen et al. (2000, [36]).
 - $C/O = 1.1$ for the best fit model with $T_{eff} = 2900\text{ K}$ and $\log(g [cm/s^2]) = -1.5$, from Jørgensen et al. (2000, [36]).
- Radius: $R = 333 R_\odot$, from Van Belle & Thompson (2000, [72]), with Hipparcos distance and the angular diameter.
- Luminosity: $L = 7700 L_\odot$ from Claussen et al. (1987, [14]).
- Mass loss rate: $dM/dt = 1.62 \cdot 10^{-6} M_\odot/\text{yr}$, from Claussen et al. (1987, [14]). The time-averaged mass-loss rate therein was calculated after the formulae of Jura (1987, [39]).
- V460 Cyg is a monoperoiodic variable with a photometric period of 180 days (Kiss et al. (1999, [42])).

4.2 Z Psc

Z Psc is a carbon star with the Yamashita (1972, [78]) spectral classification C7,2. It has the variability type SRb (data from the AGB database).

4.2.1 Photometric Data

Photometric data of Z Psc are listed in Tab. 4.5, bolometric fluxes in Tab. 4.6.

B [mag]	V [mag]	J [mag]	H [mag]	K [mag]
9.58	6.76	2.380 ± 0.312	1.098 ± 0.220	0.865 ± 0.202
F12 [Jy]	F25 [Jy]	F60 [Jy]	F100 [Jy]	
33.42	11.20	3.29	1.72	

Table 4.5: Photometric data of Z Psc, taken from the Simbad database. The J, H and K magnitude are originally from the 2MASS All Sky Catalog of point sources (Cutri et al. (2003, [16])). F12, F25, F60 and F100 are the colour corrected IRAS fluxes at 12, 25, 60 and 100 μm (taken from the AGB database (Kerschbaum (1993, [40]))).

F_{bol} [W/cm^2]:	[8]	[8]	[18]	[72]
	$7.35 \cdot 10^{-14}$	$7.53 \cdot 10^{-14}$	$8.84 \cdot 10^{-14}$	$5.57 \cdot 10^{-14}$

Table 4.6: Bolometric (F_{bol}) fluxes of Z Psc. The numbers in the squared brackets give the references from where the data were taken ([8]...Bergeat et al. (2001), [18]...Dyck et al. (1996), [72]...VanBelle & Thompson (2000)).

4.2.2 Spectroscopic Data

Two visual spectra could be found for Z Psc. The first is from Barnbaum (1996, [6], Fig. 4.3). It has the same resolution than the spectrum for V460 Cyg. The second one is from Lazaro (1994, [47]) and is not used in this work (because of its very low resolution). Unfortunately, no ISO spectry exists for this star.

4.2.3 Interferometric Data

A visibility measurement is available from the IOTA interferometer (Dyck et al. (1996, [18])): Visibility $V = 0.810 \pm 0.123$, Baseline $B = 38.21$ m, $\lambda = 2.2 \mu\text{m}$, $\Delta\lambda = 0.4 \mu\text{m}$, $\Theta_{UD} = 4.8 \pm 0.7$ mas.

Another interferometric observation was done at the Palomar Testbed Interferometer (PTI). Unfortunately, no visibility and corresponding spatial frequency value could be found in the literature. The Rosseland mean angular diameter resulting from this measurement is $\Theta_R = 4.38 \pm 0.21$ mas (Van Belle & Thompson (2000, [72])).

4.2.4 Effective Temperature

The effective temperatures estimates for Z Psc are listed in Table 4.7. An explanation of the different methods to determine the effective temperatures of stars is given in the previous section (4.1.4).

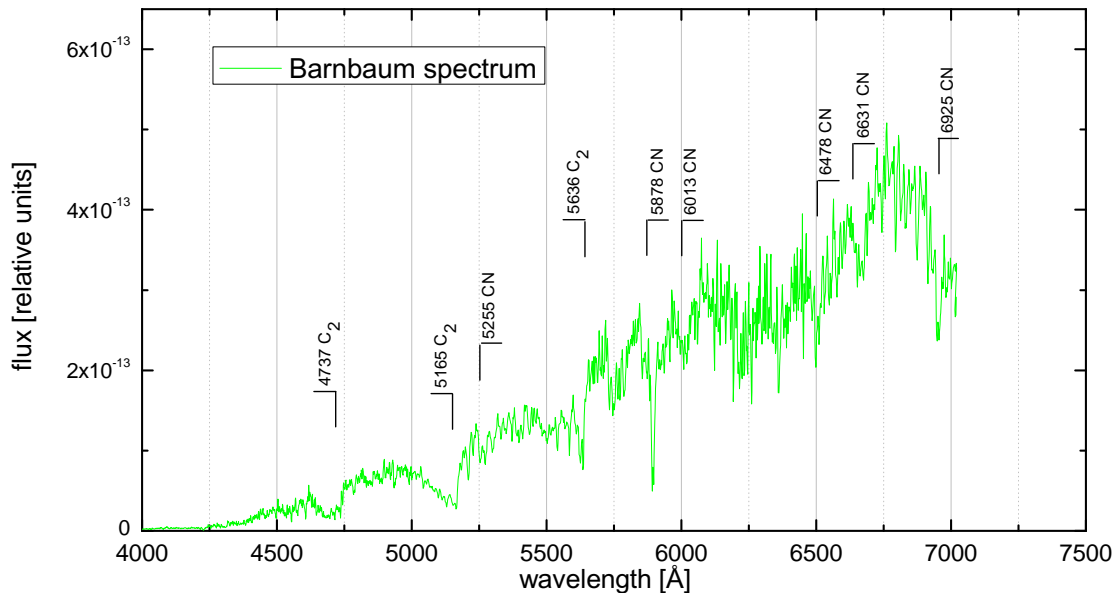


Figure 4.3: Visible Spectrum of Z Psc from Barnbaum (1996, [6]) in the wavelength range from 4000Å to 7019Å.

T_{eff} [K]	$\sigma_{T_{eff}}$ [K]	Determination	Reference
3095	-	Combination of spectral energy distributions, color indices, model atmospheres and interferometry	Bergeat et al. (2001, [8])
3130	230	Interferometry	Bergeat et al. 2001, [8])
3051	114	Interferometry, with $\Theta_R = 4,38$ mas	Van Belle & Thompson (2000, [72])
2913	228	Interferometry, with $\Theta_R = 4,91$ mas	Van Belle & Thompson (2000, [72])
3145	-	Bolometric fluxes and angular diameters	Ohnaka & Tsuji (1998, [51])
3145	-	Infrared flux method	Ohnaka & Tsuji (1996, [52])
3240	239	Interferometry	Dyck et al. (1996, [18])
2870	-	NIR photometry	Lambert et al. (1986, [45])

Table 4.7: The effective temperatures and their standard deviations ($\sigma_{T_{eff}}$) of Z Psc in the literature.

distance [pc]	determination	Reference
323.6	^a parallax	Hipparcos (1997, [55])
465	^b parallaxes and proper motions	Bergeat Chevallier (2005, [7])
600	^c $M(K) = -8.1$ mag	Claussen et al. (1987, [14])
662	^c mean luminosity $7500 L_{\odot}$	Blanco (2000, [12])
270	radial velocity and galactic rotation	Yuasa et al. (1999, [79])

Table 4.8: The distances of Z Psc in the literature.

^aThe exact value of the parallax is 3.09 ± 0.83 . This corresponds to a minimum distance of 255.1 pc and a maximum distance of 442.5 pc.

^bThis estimation combines the measured Hipparcos parallax and the proper motion of the carbon star. It is assumed that the star's proper motion decreases linearly with the distance. This implies a uniform velocity distribution of carbon stars. Hanson (1979, [31]) showed that this is close to reality.

^cThese two determinations depend on the observed fact that all carbon stars have similar absolute luminosities in the K-band. Measuring the apparent magnitude in this band leads in combination with a determination of the interstellar reddening to the distance of the carbon star.

4.2.5 Distance

The distances for Z Psc are listed in Tab. 4.8

4.2.6 Further Data

- Coordinates of Z Psc (from the Hipparcos catalogue, $eq = 2000$): right ascension $\alpha = 01h16'05.030''$, declination $\delta = +2546'09.69''$ (Perryman et al. (1997, [55])).
- C/O abundance ratio: $C/O = 1.014$, from Lambert et al. (1986, [45]), determination with near infrared spectra (1.5 - 2.5 μm) and model atmospheres.
- Radius: $R = 317 R_{\odot}$, from Van Belle & Thompson (2000, [72]), with the Hipparcos distance and the angular diameter $\Theta_R = 4.91$ mas from Dyck et al. (1996, [18]).
- Radius: $R = 283 R_{\odot}$, from Van Belle and Thompson (2000, [72]), with the Hipparcos distance and the angular diameter $\Theta_R = 4.38$ mas from Van Belle & Thompson (2000, [72]).
- Luminosity: $L = 7500 L_{\odot}$ (Claussen et al. (1987, [14])).
- Mass loss rate: $dM/dt = 0.93 \cdot 10^{-6} M_{\odot}/\text{yr}$ (Claussen et al. (1987, [14])). The time-averaged mass-loss rate therein was calculated after the formulae of Jura (1987, [39]).
- Z Psc seems to be a biperiodic object with periods of 156 days and 269 days (Percy et al. (2001, [54])).

Chapter 5

Hydrostatic Models

In this chapter, the model calculations are presented. The hydrostatic models are computed using a MARCS code (Sec. 1.2). In Sec. 5.1 we start with the intensity distributions and the visibility profiles in some narrow band filters and in the K-band filter. In Sec. 5.2 we compare our models to AGB evolutionary tracks and in Sec. 5.3 we show the behaviour of the partial pressures of important molecules with depth.

The hydrostatic models listed in Tab. 5.1 are used in this thesis to compare the observed data of V460 Cyg and Z Psc to our model calculations (Ch. 7 and 8).

The effective temperature of the models ranges from 2800 to 3200 K. We studied models with 1 and 2 M_{\odot} , a C/O ratio of 1.1 and 1.4, a $\log(g [cm/s^2])$ from 0.00 to -0.70 and a metallicity of 0.33 and 1 Z_{\odot} .

$T_{eff} [K]$	$M [M_{\odot}]$	C/O	$\log(g [cm/s^2])$	$Z [Z_{\odot}]$	$T_{eff} [K]$	$M [M_{\odot}]$	C/O	$\log(g [cm/s^2])$	$Z [Z_{\odot}]$
2800	1	1.1	-0.70	1	3075	2	1.4	-0.50	1
2800	2	1.1	-0.70	1	3100	2	1.1	-0.50	1
2800	1	1.4	-0.65	1	3100	2	1.4	-0.50	1
2800	2	1.4	-0.65	1	3100	2	1.4	0.00	1
2800	2	1.4	0.00	0.33	3100	2	1.4	0.00	0.33
2900	2	1.1	-0.70	1	3200	1	1.1	-0.50	1
2900	2	1.1	-0.70	1	3200	1	1.1	0.00	1
2900	2	1.4	0.00	0.33	3200	2	1.4	0.00	1
3000	2	1.1	-0.50	1	3200	2	1.1	0.00	1
3000	2	1.4	-0.50	1	3200	2	1.1	-0.50	1
3000	2	1.4	0.00	1	3200	2	1.4	-0.50	1
3000	2	1.4	0.00	0.33	3200	2	1.4	0.00	0.33
3050	2	1.4	-0.50	1					

Table 5.1: The parameters of the models which are used in this thesis.

5.1 Filters

5.1.1 Intensity Distributions and Visibility Profiles - Narrow Band Filters

The narrow band filters which are used to calculate the intensity distributions and visibility profiles of the models are shown in Fig. 5.1. The bandwidth of these filters ranges from 20 to 50 nm. They are placed in transparent atmospheric windows and they cover important absorption features as well as pseudo-continuum regions of carbon stars. The location in atmospheric windows allows a comparison of the synthetic intensity distributions and visibility profiles to earth bound observations. For this reason no narrow band filter was placed in the wavelength region between 5 and 10 μm and in the other regions which contain no filter. Mainly, the absorption of water vapor in the earth's atmosphere makes these regions intransparent to earth bound observations.

Filters f. synth. Interferometry: hydrostatic C-rich MARCS-model $L=7000L_{\odot}$, $T_{\text{eff}}=2650\text{K}$, $\log g=-0.76$

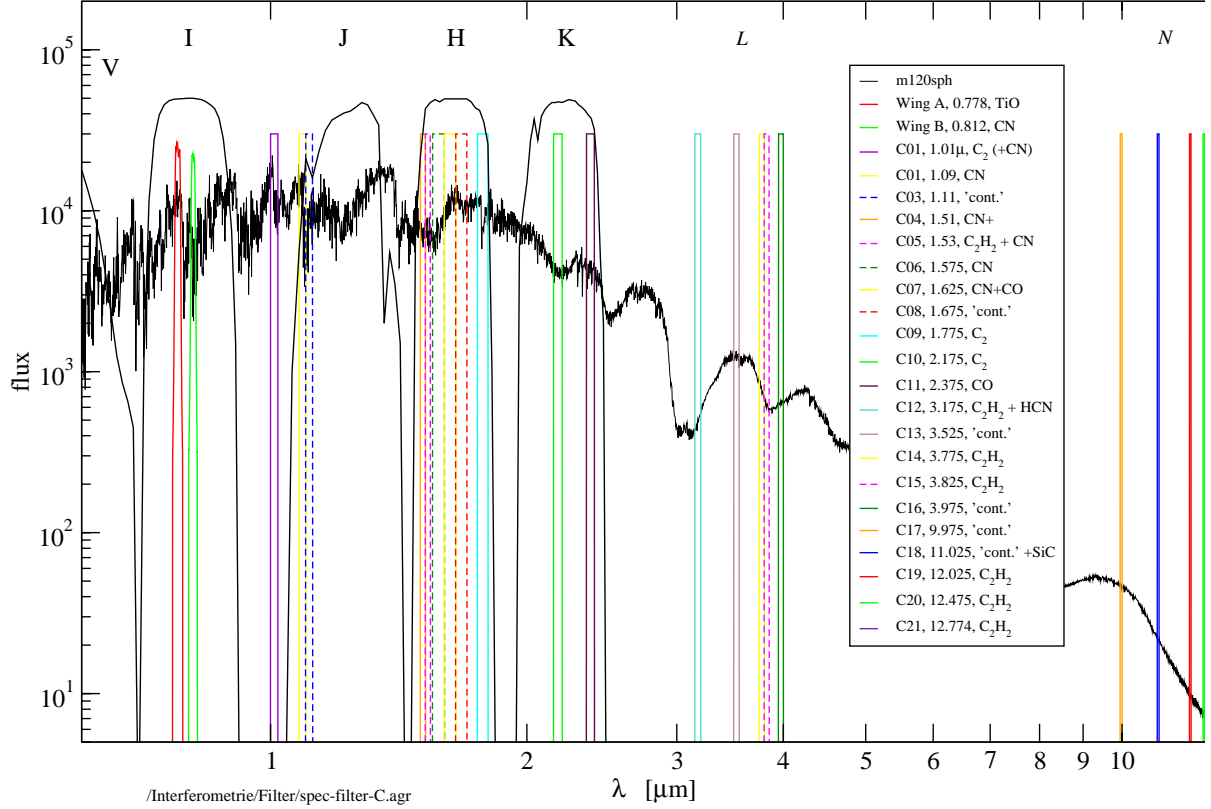


Figure 5.1: The narrow band filters are shown with a spectrum of a cool carbon star ($L = 7000L_{\odot}$, $T_{\text{eff}} = 2650\text{K}$, $\log(g [cm/s^2]) = -0.76$). The filters are placed in transparent atmospheric windows and they cover different absorption features of carbon stars. The legend contains the central wavelength of each filter (in μm) and the molecule which dominates the spectrum in this region. The bandwidth of the narrow band filters ranges from 20 to 50 nm. Two filters of the Wing filter system (Wing (1992, [75])), which was developed to study the molecular features of red giants, are also included. The I, J, H, K L and N broadbandfilters are also shown.

The intensity distributions (i.e. the center to limb darkening) of the models are shown for the narrow band filters at 1.01, 1.51, 1.575, 1.675, 2.175, 3.175, 3.775 μm in Fig. 5.2 and for 3.975, 9.975, 11.025, 12.775 μm in Fig. 5.3. The legend for all of the models is shown in the upper right panel in Fig. 5.2. The dotted lines stand for the models with $C/O = 1.1$, the solid ones for the models with $C/O = 1.4$. In these figures we see some overall characteristics of the models of these stars: The radii vary from ≈ 0.8 AU for the models with $M = 1 M_{\odot}$ and a $\log(g [cm/s^2]) = 0.00$ to ≈ 2.7 AU for the models with $M = 2 M_{\odot}$ and a $\log(g [cm/s^2]) = -0.70$. An interesting fact is that with increasing wavelength the intensity profile is flatter near the center and becomes steeper towards the limb of the star. This wavelength dependent effect occurs in all the models that are used here.

Let us look now in more detail at the intensity profiles: We see that there is not much difference in the intensity profiles between the models with $T_{eff} = 3200$ K, 1 (2) M_{\odot} , $C/O = 1.1$ and $T_{eff} = 3200$ K, 1 (2) M_{\odot} , $C/O = 1.4$. This is not the case when we compare the models with $T_{eff} = 2800$ K. The $T_{eff} = 2800$ K, 2 M_{\odot} model with $C/O = 1.1$ (red dotted line in Fig. 5.2) shows a slightly larger extension than the model with $C/O = 1.4$ (red solid lines). The overall shape of the intensity profiles of these two models is very similar. The larger extension of the model with $C/O = 1.1$ is because this model is calculated with a smaller $\log(g [cm/s^2])$ (-0.70) than the one with $C/O = 1.4$ ($\log(g [cm/s^2]) = -0.65$). This effect also exists in the $T_{eff} = 2800$ K, 1 M_{\odot} models (black lines in Tabs. 5.2 and 5.3). However, it is not so pronounced as in the models with 2 M_{\odot} .

Beginning at a wavelength of 3.175 μm , the models with $T_{eff} = 3200$ K show a small spike in the outer regions (at 0.8 AU for 1 M_{\odot} and 1.15 AU for 2 M_{\odot} in the narrow band filter at 3.175 μm). It is located at a normalized intensity of ≈ 0.3 . At 3.775 μm , this spike is shifted to smaller intensities ($I/I_0 = 0.15$). For longer wavelengths, the location of the spike moves to higher intensities (from $I/I_0 = 0.2$ at 3.975 μm to $I/I_0 = 0.6$ at 12.775 μm). The spike occurs in the intensity distributions of the models with $C/O = 1.1$ and $C/O = 1.4$, but it is more pronounced in the models with $C/O = 1.4$.

In some narrow band filters, the more extended models ($T_{eff} = 2800$ K) have a quite pronounced bulge in the outer regions. At 2.175 μm it is located at a normalized intensity of $I/I_0 \approx 0.3$. At 3.175 μm , this bulge only occurs in the model with $T_{eff} = 2900$ K; $\log(g [cm/s^2]) = -0.70$; $M = 2 M_{\odot}$; $Z = Z_{\odot}$; $C/O = 1.1$. In the narrow band filters from 3.775 μm to 11.025 μm , it appears again in all the models with $T_{eff} < 3200$ K. As the spike in the models with $T_{eff} = 3200$ K, the bulge is shifted to higher normalized intensities at longer wavelengths. At 12.775 μm , the bulge is completely absent in all the models.

Visibility Profiles of Different Intensity Distributions

The visibility functions of the models are shown in Fig. 5.4 (lower panel) for one narrow band filter (at a wavelength of 2.175 μm). We only present one narrow band filter because the visibility functions in the various studied models do not show much difference. In the lower panel of Fig. 5.4, the normalized visibility is plotted on the ordinate. The more extended models have their first zero points of the visibility functions at lower spatial frequencies corresponding to a more resolved source. The spatial frequency is plotted on the abscissa in units of 1/AU. In most cases in the literature it is given in units of 1/arcsec. This can be interpreted as the inverse of an angle on the sky which is a function of the star's diameter and distance. Knowing the distance to the star, the spatial frequency

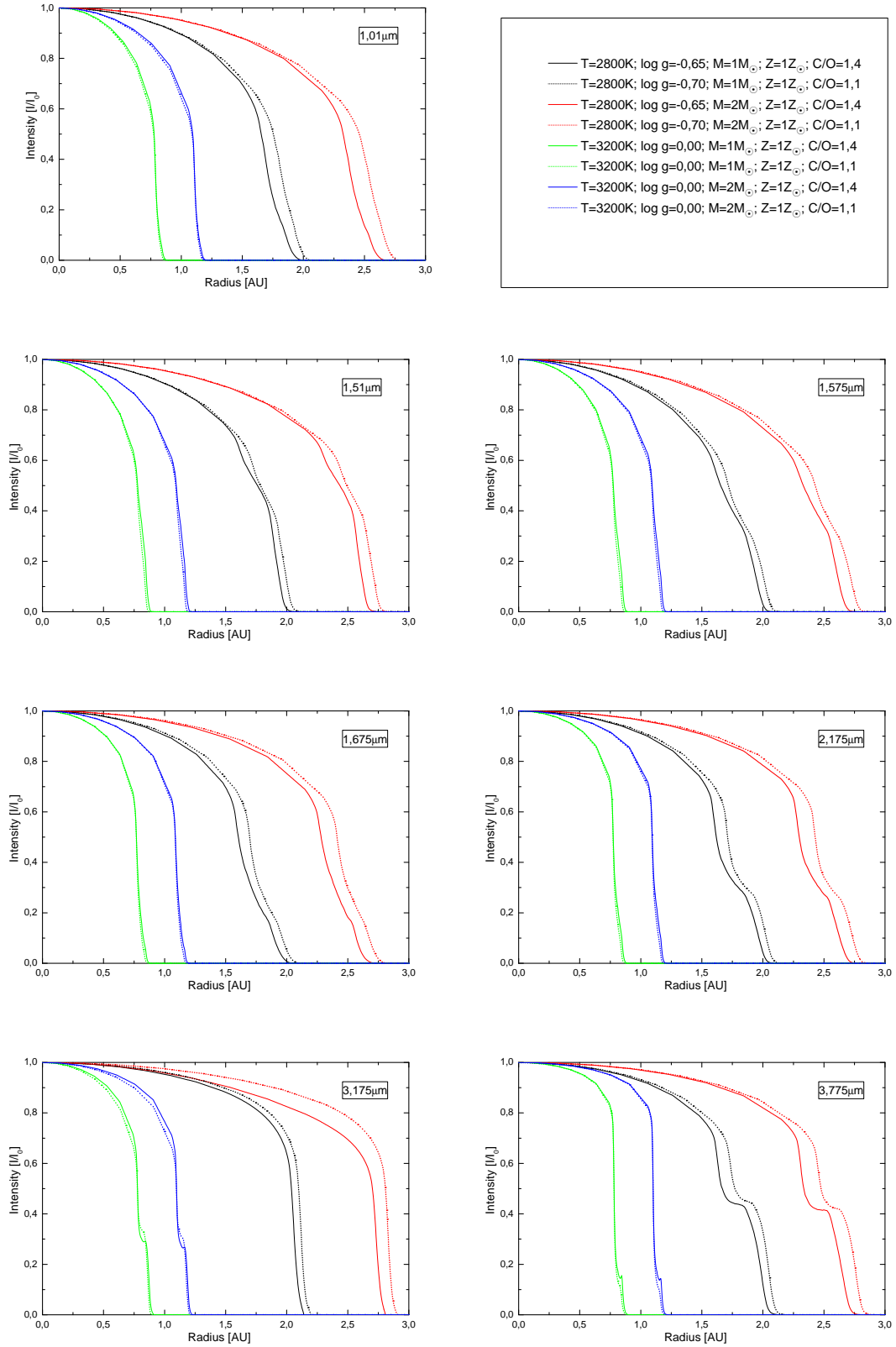


Figure 5.2: Intensity distributions of the different models in some narrow band filters from $1.01\ \mu\text{m}$ to $3.775\ \mu\text{m}$. The solid lines are the models with a C/O ratio of 1.4, the dotted lines are the models with a C/O ratio of 1.1. A detailed discussion can be found in the text.

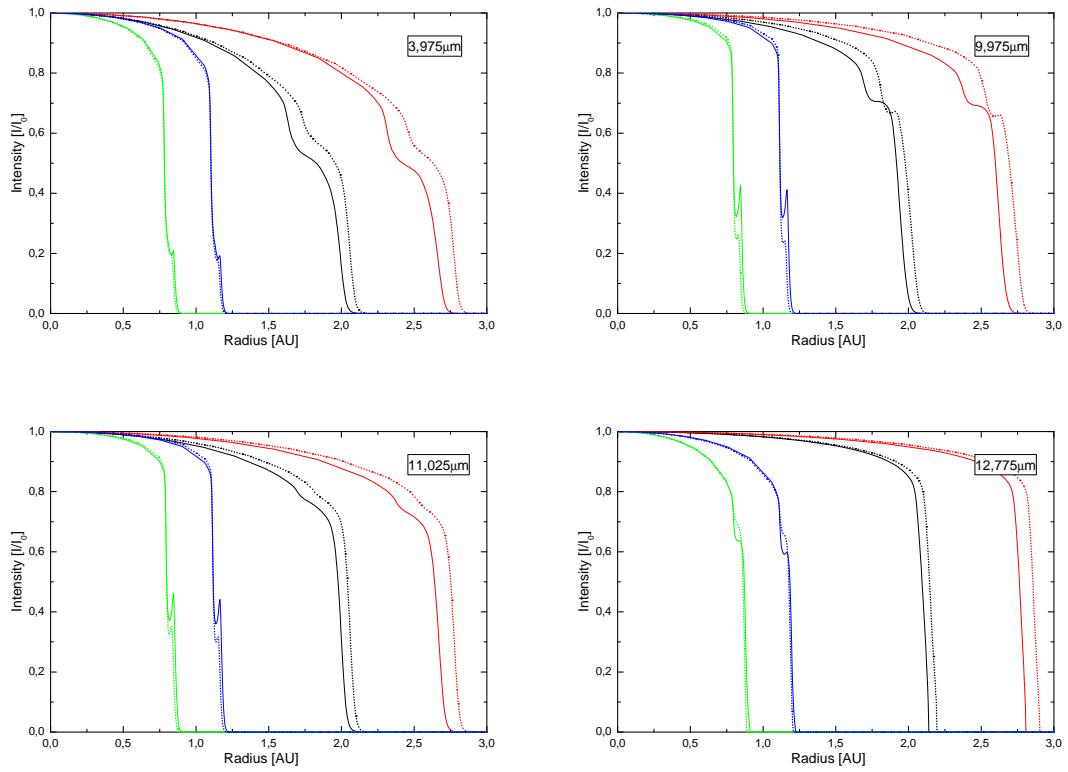


Figure 5.3: Intensity distributions of the different models in some narrow band filters from $3.975 \mu\text{m}$ to $12.775 \mu\text{m}$. The solid lines are the models with a C/O ratio of 1.4, the dotted lines are the models with a C/O ratio of 1.1. A detailed discussion can be found in the text.

expressed in units of an inverse angle can be converted into an inverse radius of the star:

$$f_{sp} = \frac{B}{\lambda} \frac{1}{D[\text{pc}] \cdot 206265}, \quad (5.1)$$

where f_{sp} is the spatial frequency in 1/AU, B the baseline of the interferometer, λ the wavelength, D is the distance in parsec and the factor 206265 makes the transition from angular distances to Astronomical Units. In this thesis, the spatial frequency is always expressed in the unit 1/AU. The reason for this is that the visibility functions of the models can then be better compared with each other without assuming a specific distance. However, a comparison with observations of a given star needs a proper conversion involving the distance, the baseline and the wavelength.

In Fig. 5.5, we see the intensity distributions (upper panel) and visibility functions (lower panel) of one model ($T_{eff} = 3200$ K; $\log(g [cm/s^2]) = 0.00$; $M = 2 M_{\odot}$; $Z = Z_{\odot}$; $C/O = 1.4$) in different narrow band filters. The intensities are shown in the outer parts of the atmosphere (from 0.8 to 1.2 AU). In this Fig., the variation in the intensity profiles at different wavelengths can be seen clearly. They are due to the fact that different molecules have their absorption maximum in different atmospheric depths at different wavelengths. Hence, less radiation is passed through this layer at the wavelength of absorption and the intensity profile shows a 'dent' in this layer. The lower panel in Fig. 5.5 shows the visibility functions of the intensity distributions. The visibility functions in Fig. 5.5, which are the Fourier transforms of the intensity distributions on the sky at the spatial frequencies (chapter 1.3), have their first zero point at lower spatial frequencies with increasing wavelength. This is because the extension of the star is larger at longer wavelengths. This results in a more resolved source and in less contrast between the interference fringes. In spite of the notable differences in the intensity profiles, differences in the visibility profiles seem to be not very pronounced.

Let us contemplate in more detail how different intensity distributions (i.e. different center to limb intensity variations) influence the corresponding visibility functions: Therefore we look at two models which show significant deviations in the intensity distributions and compare the shape of their visibility functions. We choose the models with $T_{eff} = 2800$ K; $\log(g [cm/s^2]) = -0.65$; $M = 1 M_{\odot}$; $Z = Z_{\odot}$; $C/O = 1.4$ and $T_{eff} = 3200$ K; $\log(g [cm/s^2]) = 0.00$; $M = 1 M_{\odot}$; $Z = Z_{\odot}$; $C/O = 1.4$ in the narrow band filter at $3.775 \mu\text{m}$. The shape of their intensity distributions and the visibility functions are presented in Fig. 5.6. The radii of these models differ greatly (≈ 0.75 AU for the model with $T_{eff} = 3200$ K and ≈ 2.15 AU for the model with $T_{eff} = 2800$ K). Our interest lies only on the shape of the visibility function. To compensate for the size differences of the models, the first zero point of the visibility function from the model with $T_{eff} = 2800$ K is forced to coincide with the first zero point of the visibility function from the model with $T_{eff} = 3200$ K by scaling the abscissa properly. The visibility functions of the models are presented in the lower panel of Fig. 5.6.

The upper panel in this figure shows the shape of the intensity distributions (for a better comparability, the zero point of the intensity distribution from the model with $T_{eff} = 2800$ K is again forced to coincide with the first zero point of the intensity distribution from the model with $T_{eff} = 3200$ K). The effect of limb darkening is more pronounced in the model with $T_{eff} = 2800$ K. The deviations in the intensity distributions also have some implications on the visibility profiles: The shape of the first lobe of the visibility functions shows no significant difference when comparing the two models. The difference in the center to limb intensity variation of the models affects only the second lobe of the interference fringes. It results in a lower amplitude of the second lobe for the model with $T_{eff} = 2800$ K. This is an example that it is in principle possible to

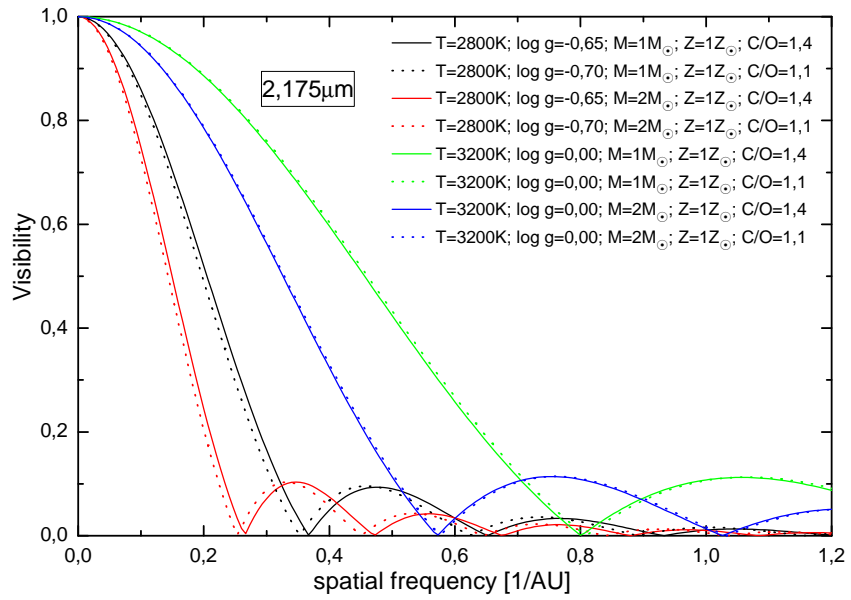
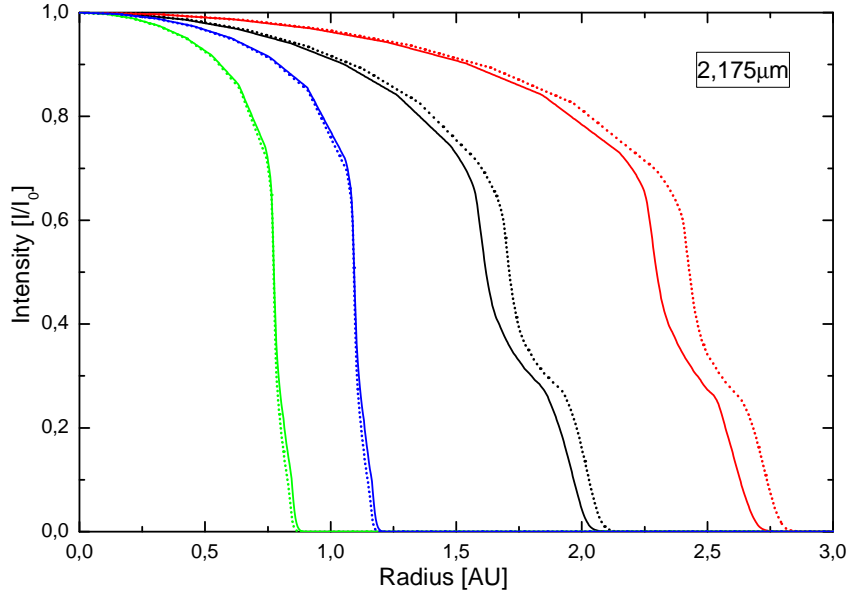


Figure 5.4: Intensity distributions (upper panel) and the normalized visibility functions (lower panel) of different models at 2.175 μm .

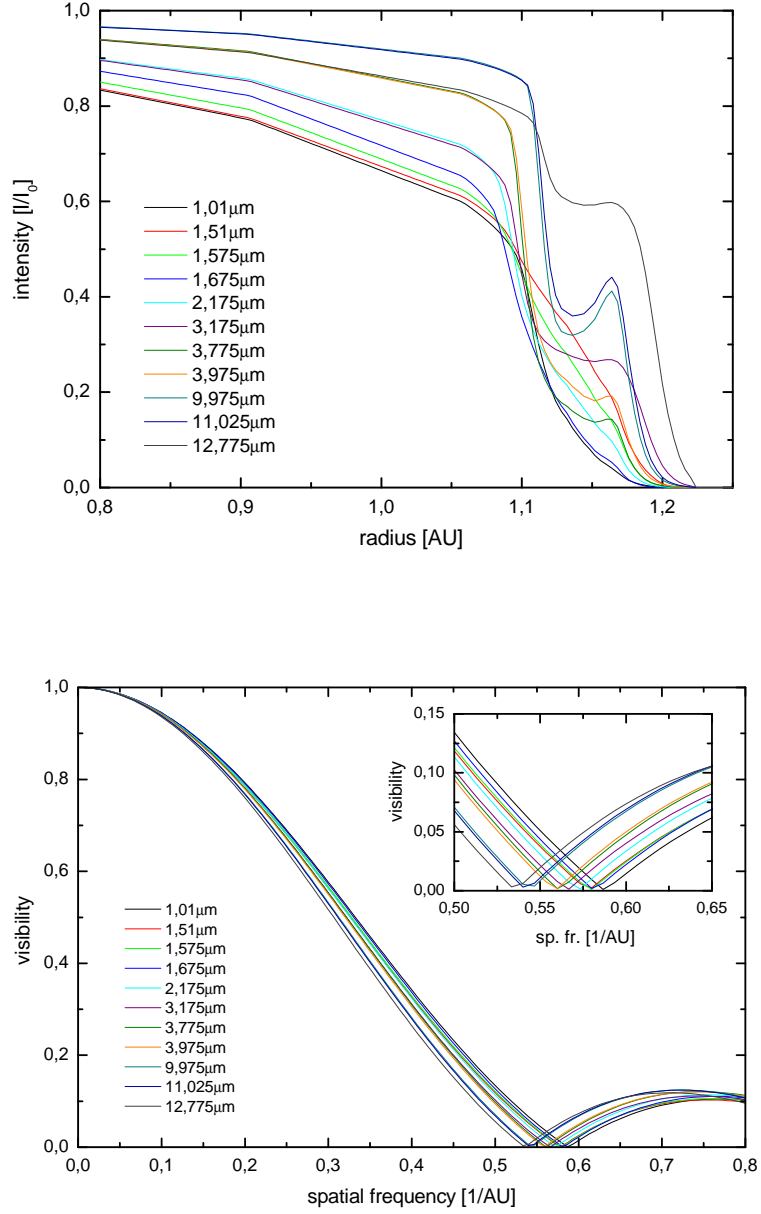


Figure 5.5: Intensity distributions (upper panel) and visibility functions (lower panel) in different narrow band filter. Here shown for the model $T_{eff} = 3200 \text{ K}$; $\log(g [cm/s^2]) = 0.00$; $M = 2 M_{\odot}$; $Z = Z_{\odot}$; $C/O = 1.4$. The visibility function around the first zero point is displayed in detail in the upper right corner in the lower panel.

measure the intensity distribution (or the limb darkening) of a star with a visibility measurement in the second lobe. Measuring these center to limb variations is quite difficult in astronomical interferometry because of the following reasons:

- More than one visibility measurement is required to determine the intensity distribution of a star. Therefore, measurements at different baselines have to be done.
- Measuring in the second lobe demands interferometers with long baselines (given the typical sizes of the stars). As a consequence, the fringe contrast decreases and the corresponding visibility amplitude gets very low. As it can be seen in Fig. 5.6, the differences in the shape of the second lobe between the investigated intensity distributions are significant, but only $\approx 2.5\%$. Therefore, the error bars in the visibility measurements must be low to distinguish between different center to limb intensity variations. This requires interferometers with high accuracy.
- For this reason not many limb darkening measurements (visibility measurements in the second lobe) of stars have been done until now. For example, Wittkowski et al. (2004, [76]) made interferometric measurements of one star in the second lobe with the Very Large Telescope Interferometer (VLTI) and its instrument VINCI. The results showed good agreement with the hydrostatic model calculations and differed significantly from predictions for a uniform disk or a fully darkened disk intensity distribution.

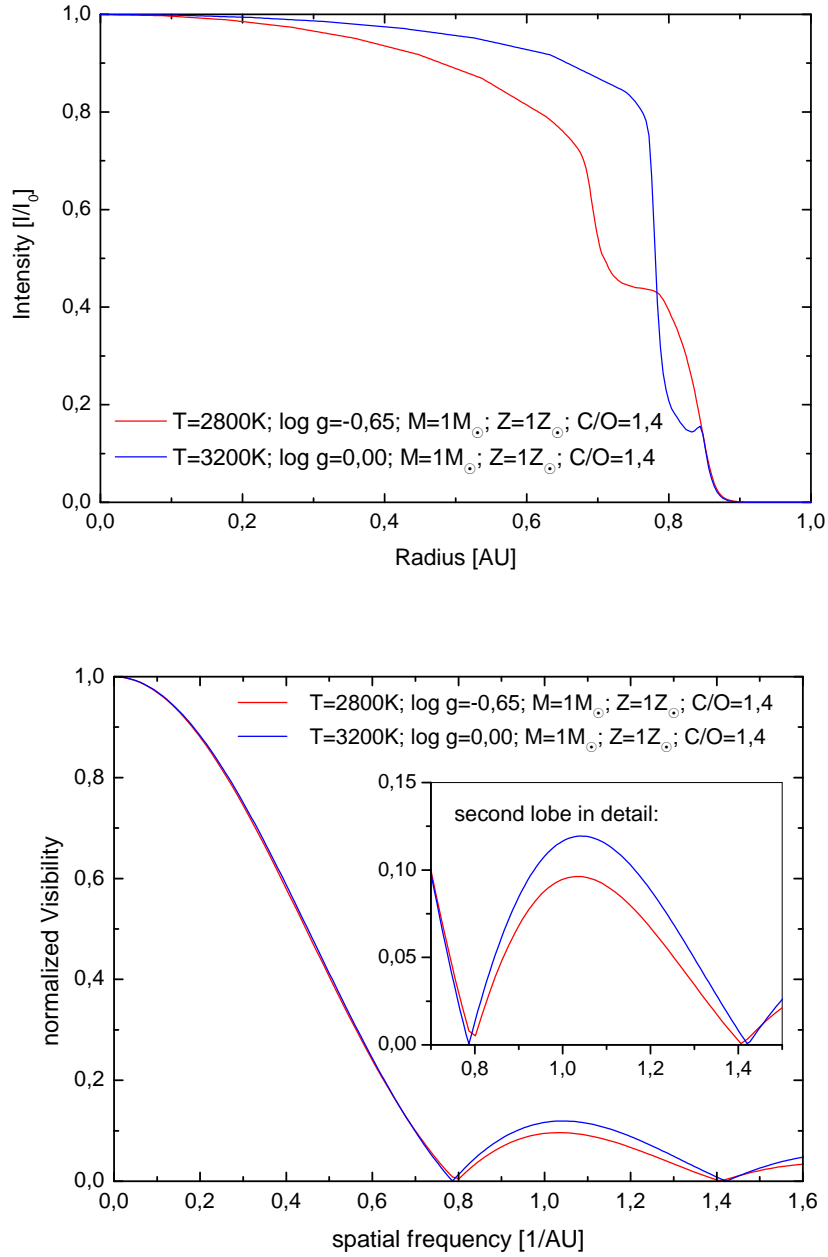


Figure 5.6: Intensity distributions and visibility functions in the $3.775 \mu\text{m}$ narrow band filter. Here shown for the models with $T_{eff} = 2800 \text{ K}$; $\log(g [\text{cm}/\text{s}^2]) = -0.65$; $M = 1 M_{\odot}$; $Z = Z_{\odot}$; $C/O = 1.4$ (red line) and with $T_{eff} = 3200 \text{ K}$; $\log(g [\text{cm}/\text{s}^2]) = 0.00$; $M = 1 M_{\odot}$; $Z = Z_{\odot}$; $C/O = 1.1$ (blue line). To compensate for the size differences of the two models, the first zero point of the visibility function (and the intensity distribution) from the model with $T_{eff} = 2800 \text{ K}$ is forced to coincide with the first zero point of the visibility function (and the intensity distribution) from the model with $T_{eff} = 3200 \text{ K}$. The two models show significant differences in the center to limb intensity variations. These differences can be seen in the 2nd lobe in the visibility profiles.

5.1.2 Influences of Different Filter Widths on the Intensity Distributions

In this section we investigate the influence of the filter width on the calculation of the intensity distribution. Therefore we compare the intensity profiles of two models ($T_{eff} = 2800$ K; $\log(g [cm/s^2]) = -0.65$; $M = 1 M_{\odot}$; $Z = Z_{\odot}$; $C/O = 1.4$ and $T_{eff} = 2800$ K; $\log(g [cm/s^2]) = -0.70$; $M = 1 M_{\odot}$; $Z = Z_{\odot}$; $C/O = 1.1$) at two different wavelengths ($2.175 \mu\text{m}$ and $3.775 \mu\text{m}$). These are the central wavelengths of two narrow band filters (Sec. 5.1.1). The filter width of these two narrow band filters is $0.025 \mu\text{m}$. Then we calculated intensity distributions with a filter width of $0.001 \mu\text{m}$ and with a monochromatic filter at the same central wavelengths. In the calculation we used a rectangular filter transmission profile for the narrow band filters. In Figs. 5.7 and 5.8 the normalized intensity distributions of the different filter widths and the monochromatic filter are presented from 1.4 to 2.2 AU. We see that there is not much difference between the intensity distributions calculated with a filter width of $0.025 \mu\text{m}$ (upper panel in Fig. 5.7) or $0.001 \mu\text{m}$ (upper panel in Fig. 5.8). The similarity between the $0.001 \mu\text{m}$ and the $0.025 \mu\text{m}$ profiles is due to the absence of any wider absorption features in these regions. The intensity distributions of the monochromatic filter are shown in the lower panels of the figures. There, an interesting result occurs: The monochromatic intensities differ significantly from the intensities calculated with a finite filter width. The intensity profiles at $2.175 \mu\text{m}$ are flat up to 1.9 AU (for the model with $\log(g [cm/s^2]) = -0.65$, $C/O = 1.4$) and 1.975 AU (for the model with $\log(g [cm/s^2]) = -0.70$, $C/O = 1.1$) respectively. At larger distances to the center, the intensity profiles become very steep. An explanation for the, at first sight, astonishing deviations between the intensity distributions of the monochromatic and the narrow band filters can be found when we look at an opacity sampling spectra of the models (Fig. 5.9). The upper panel of this Figure shows the OS spectra of the 2 models around the wavelength region of $2.175 \mu\text{m}$, the lower panel shows them around $3.775 \mu\text{m}$. The edges of the narrow band filter at a central wavelength of $2.175 \mu\text{m}$ and a filter width of $0.001 \mu\text{m}$ reach from $2.1745 \mu\text{m}$ to $2.1755 \mu\text{m}$ (they are marked with two red arrows in Fig. 5.9). For a filter width of $0.025 \mu\text{m}$, the edges reach from $2.1625 \mu\text{m}$ to $2.1875 \mu\text{m}$ (blue arrows in Fig. 5.9). The resolution of the opacity sampling spectra is $R = 10000$. This means that even the filter with $\Delta\lambda = 0.001 \mu\text{m}$ contains some sampling points of the spectra. In the region around $2.175 \mu\text{m}$, the opacity sampling spectra contain many absorption features. The intensity distributions in narrow band filters is therefore a mean intensity over the filter bandwidth.

The monochromatic intensities of the models are presented with a filled circle in Fig. 5.9. At $2.175 \mu\text{m}$, they are located close to a minimum of an absorption feature ($F/F_{Cont} \approx 0.25$). This wavelength is intransparent due to the high opacity. This is the reason for the flat monochromatic intensity profile (lower panel in Figs. 5.7 and 5.8) up to large distances. At $3.775 \mu\text{m}$ we see the opposite behaviour: The monochromatic intensities are situated near the continuum ($F/F_{Cont} \approx 0.825$ for the model with $\log(g [g/cm^2]) = -0.70$, $C/O = 1.1$ and $F/F_{Cont} \approx 0.875$ for the model with $\log(g [g/cm^2]) = -0.65$, $C/O = 1.4$ respectively). The opacity at this wavelength is low. The atmosphere is very transparent. Therefore, the effects of limb darkening are very pronounced. This explains the stronger decrease in the monochromatic intensity distribution in the atmosphere.

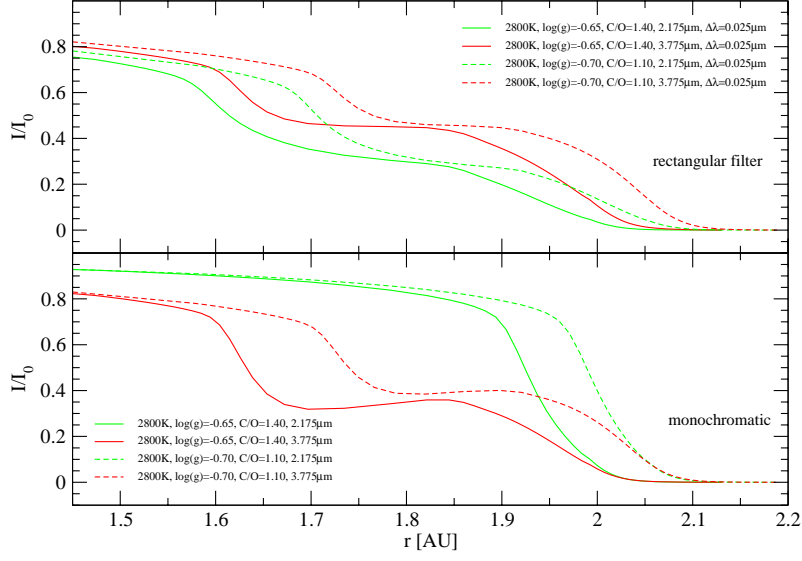


Figure 5.7: Intensity distributions of the models with $T_{eff} = 2800$ K; $\log(g [cm/s^2]) = -0.65$; $M = 1 M_{\odot}$; $Z = Z_{\odot}$; $C/O = 1.4$ (solid line) and $T_{eff} = 2800$ K; $\log(g [cm/s^2]) = -0.70$; $M = 1 M_{\odot}$; $Z = Z_{\odot}$; $C/O = 1.1$ (dashed line) for a filter width of $\Delta\lambda = 0.025 \mu\text{m}$ (upper panel) and for a monochromatic filter (lower panel).

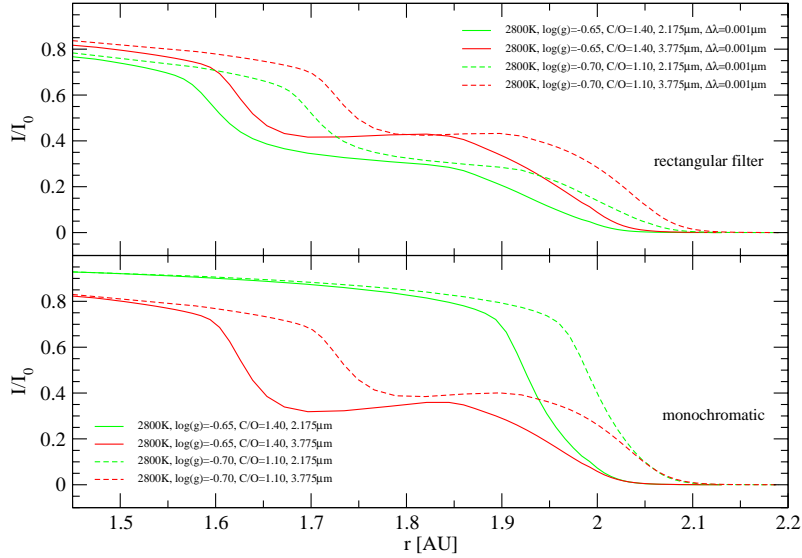


Figure 5.8: Intensity distributions of the models with $T_{eff} = 2800$ K; $\log(g [cm/s^2]) = -0.65$; $M = 1 M_{\odot}$; $Z = Z_{\odot}$; $C/O = 1.4$ (solid line) and $T_{eff} = 2800$ K; $\log(g [cm/s^2]) = -0.70$; $M = 1 M_{\odot}$; $Z = Z_{\odot}$; $C/O = 1.1$ (dashed line) for a filter width of $\Delta\lambda = 0.001 \mu\text{m}$ (upper panel) and for a monochromatic filter (lower panel).

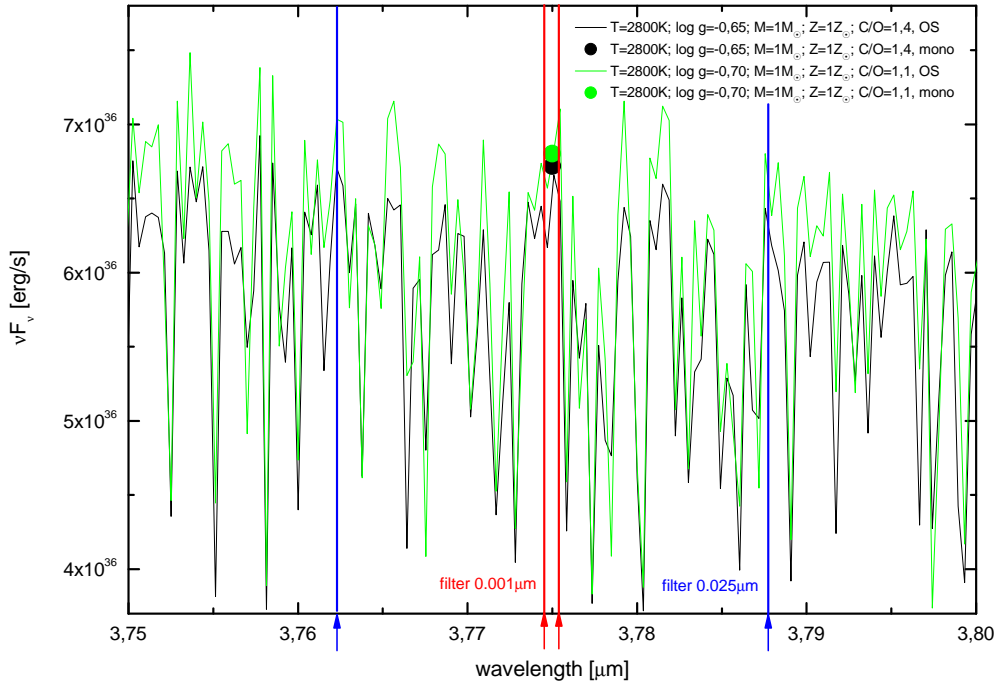
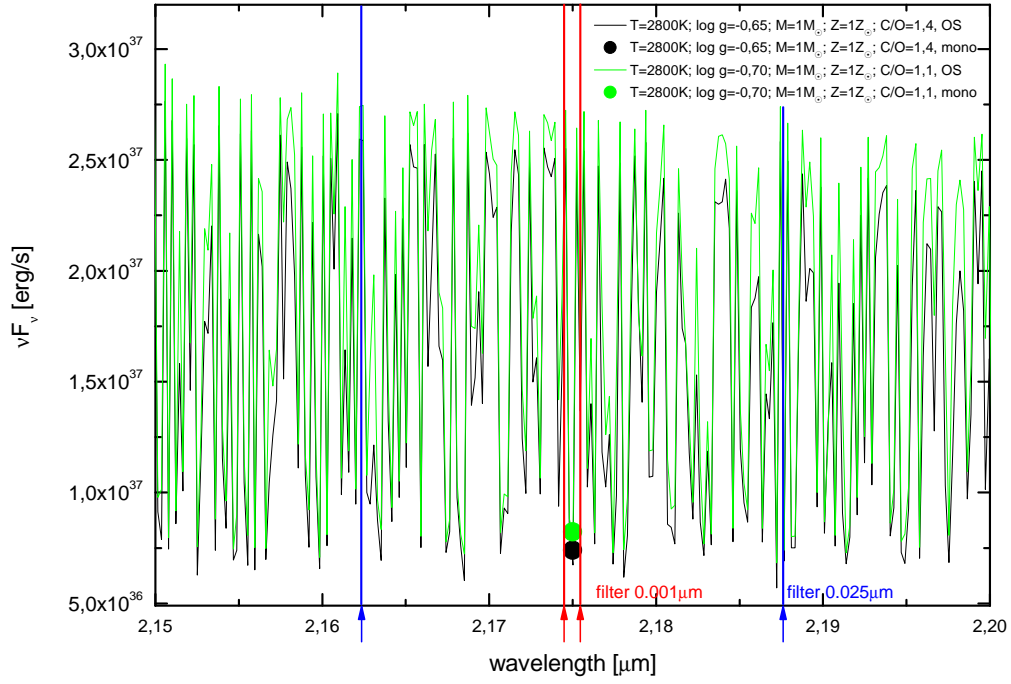


Figure 5.9: Opacity sampling spectra of the models with $T_{eff} = 2800$ K; $\log(g [cm/s^2]) = -0.65$; $M = 1M_{\odot}$; $Z = Z_{\odot}$; $C/O = 1.4$ (green line) and $T_{eff} = 2800$ K; $\log(g [cm/s^2]) = -0.70$; $M = 1M_{\odot}$; $Z = Z_{\odot}$; $C/O = 1.1$ (black line) in the wavelength range of $2.10 \mu\text{m}$ to $2.2 \mu\text{m}$ (upper panel) and $3.75 \mu\text{m}$ to $3.80 \mu\text{m}$. The filled circles denote the monochromatic fluxes at $2.175 \mu\text{m}$ and at $3.775 \mu\text{m}$. At $2.175 \mu\text{m}$ the spectrum shows a deep absorption feature, whereas at $3.775 \mu\text{m}$ the normalized flux is close to the continuum value. The filter edges of the two narrow band filters are marked with red arrows for a filter width of $0.001 \mu\text{m}$ and blue arrows for a filter width of $0.025 \mu\text{m}$ respectively.

5.1.3 Intensity Distributions and Visibility Profiles - Broad Band K-Filter

The visibility measurements of V460 Cyg and Z Psc have been done in the K-band filter at the IOTA interferometer. In order to make a comparison between observation and model calculation possible, the visibility functions of the models must also be calculated in the K-band filter. We used a corresponding standard K-band filter (Bessel & Brett (1988, [9])) with a central wavelength at $2.2 \mu\text{m}$ and a Full Width Half Maximum (FWHM) of $0.4 \mu\text{m}$ in our calculations to simulate the K-band filter at the IOTA instrument. The transmission function of the used filter is shown in Fig. 5.10.

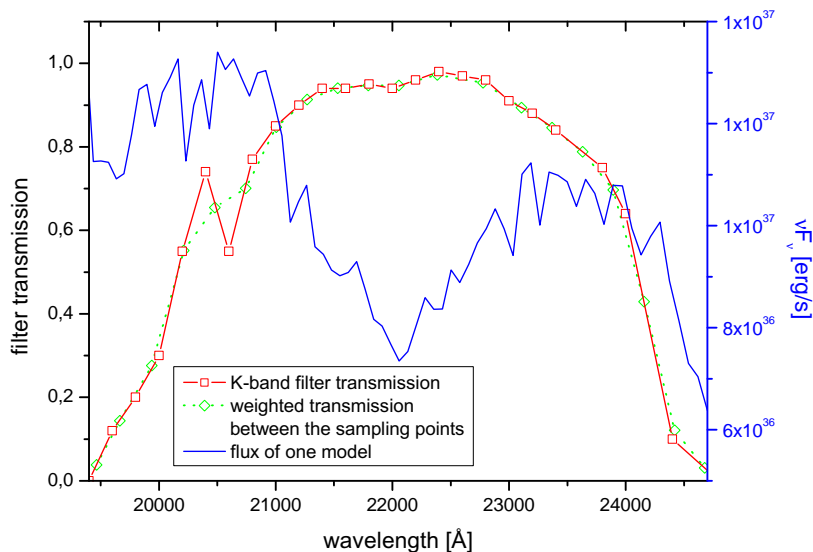


Figure 5.10: K-band filter transmission (red solid line) and the weighted mean transmission for the visibility calculation (green dashed line). The blue line shows the spectral energy distribution of the model with $T_{eff} = 2800 \text{ K}$, $\log(g [\text{cm}/\text{s}^2]) = -0.65$; $M = 1 M_{\odot}$; $Z = Z_{\odot}$; $C/O = 1.4$ in the K-band filter. See the text for a detailed explanation.

There are three reasons why it is more complicated to calculate the visibility function in a broad band filter than in a narrow band filter:

- As an example the K-band filter has a FWHM of $0.4 \mu\text{m}$. The visibility function depends on the wavelength (because the intensity distribution depends on the wavelength) and on the part of the flux spectrum of the model for which the visibility is calculated. The K-band dependency is shown in Fig. 5.11. The Fourier transform of the mean intensity profile is not equal to the mean of the Fourier transforms of the monochromatic intensities. Thus, the correct calculation of the visibility is to compute the mean of the Fourier transforms of the monochromatic intensities. In practice the monochromatic intensities are simulated by a division of the K-band in some narrow band filters. In the normal case, the flux intensity of the models (and in real stars) is not constant over the bandwidth of the filter. Therefore, a flux weighted mean has to be used in the calculation of the visibility in the whole K-band.
- The transmission function of the K-band filter (Fig. 5.10) does not have a rectangular profile which an idealized filter would have. The transmission at the edge of the

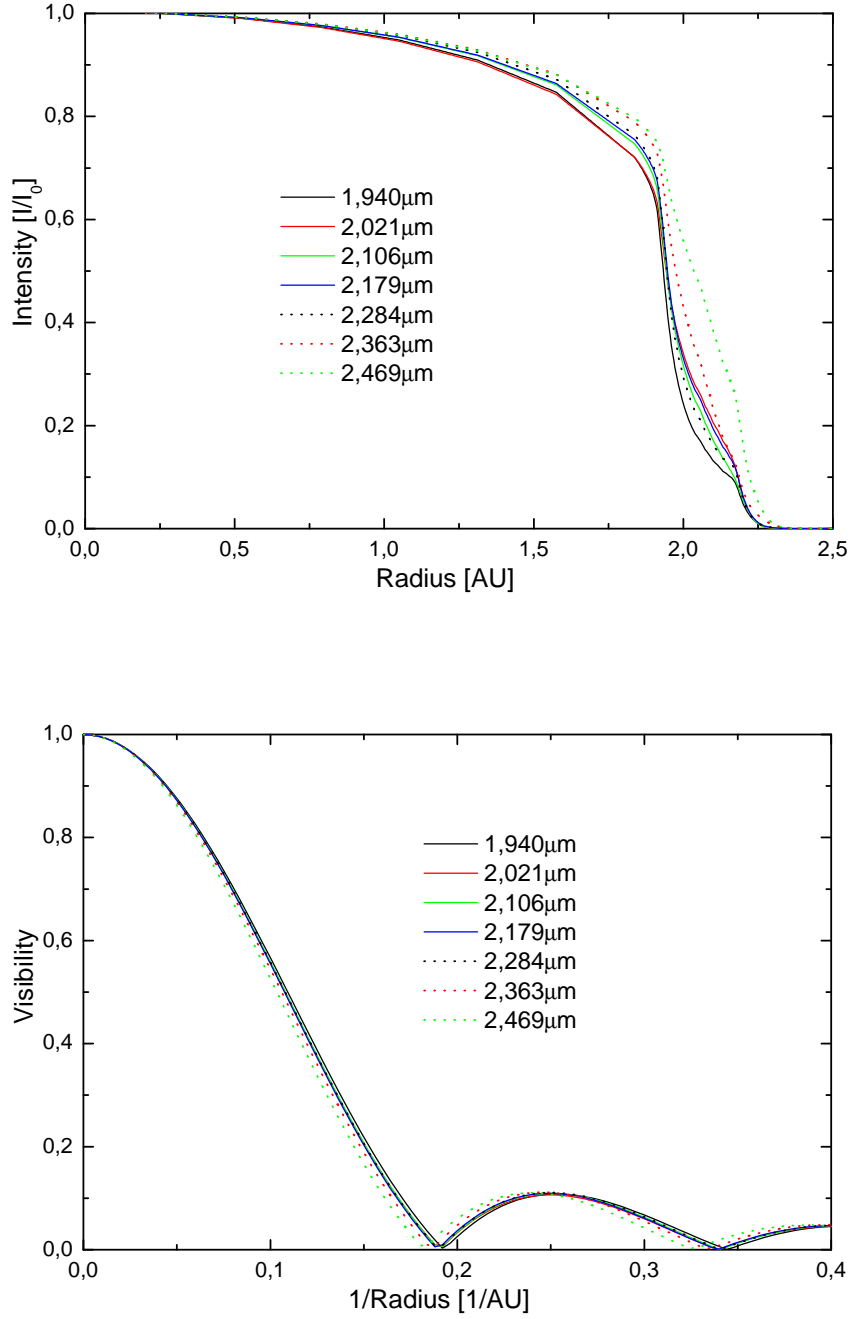


Figure 5.11: Intensity distributions (upper panel) and visibility functions (lower panel) of the splitted K-band in some of the narrow band filters which are used to simulate the K-band, here shown for the model with $T_{eff} = 3075$ K; $\log(g [cm/s^2]) = -0.5$; $M = 2 M_{\odot}$; $Z = Z_{\odot}$; $C/O = 1.4$. The bandwidth of each filter is $0.26 \mu m$.

filter is smaller than in the central region. If we want to compare the calculated K-band visibilities to observed ones, the incoming flux of the star must be weighted with this transmission value.

- The spatial frequency at a given baseline depends on the wavelength. This is of importance when a comparison with observations is made and will be considered later.

These three facts must be taken into account when calculating visibility functions in the K-band filter. In this thesis, the following way was adopted to to this:

- The K-band (19393.7 Å - 24687.5 Å, Fig. 5.10) was splitted in 20 narrow bands with a bandwidth of ≈ 262.5 Å. Then, the visibility function was computed at the central wavelength of each narrow band filter from the mean intensity profile.
- The flux was integrated in each narrow band with a simple trapeze integration from the model spectra. The resolution of the spectra is therefore sufficient. This leads to the net flux in each band.
- The filter transmission in the 20 narrow band filters \overline{T}_j is calculated over a weighted mean between the 19 sampling points of the K-filter curve contained in each of them:

$$\overline{T}_j = \frac{T_{m1}\Delta\lambda_1 + T_{m2}\Delta\lambda_2 + \dots + T_{mi}\Delta\lambda_i}{\Delta\lambda_1 + \Delta\lambda_2 + \dots + \Delta\lambda_i}, \quad (5.2)$$

where T_{mi} is the mean filter transmission in the i-th part of the filter transmission curve and $\Delta\lambda_i$ is the wavelength difference between the sampling points of the K-band filter transmission (the width of the i-th part of the curve, see Fig. 5.12). The green dotted line in Fig. 5.10 shows the shape of this weighted transmission in the whole K-band filter. The diamonds are the mean values in each narrow band, which are used in the further calculations.

- The visibility function in the whole K-band filter $V(S)$ weighted with the filter transmission and the net flux can then be calculated by:

$$V(S) = \frac{\sqrt{\sum_{j=1}^{20} (T_j \cdot \frac{F_j}{F_0} \cdot V_j)^2}}{V(0)}, \quad (5.3)$$

where T_j , F_j and V_j are the mean filter transmission, the net flux and the visibility in the j-th band filter, F_0 is the net flux in the whole K-band filter and $V(0)$ is the central visibility value (to normalize the maximum of the visibility function to one). The squared term $(T_j \cdot \frac{F_j}{F_0} \cdot V_j)^2$ in Equ. 5.3 is used, because the reduction of the observational data also results in a squared visibility: The output of an astronomical interferometer is an interferogram. A Fourier analysis can be used to derive the power spectral density of the interferogram. This power spectral density is a squared quantity. The (observed) squared visibility is derived from the integration of the power spectral density over the wavelength. For this reason we also use squared visibilities in our calculation for the K-band. The next section includes also an error calculation if linear visibilities are used in the calculation of the K-band visibility.

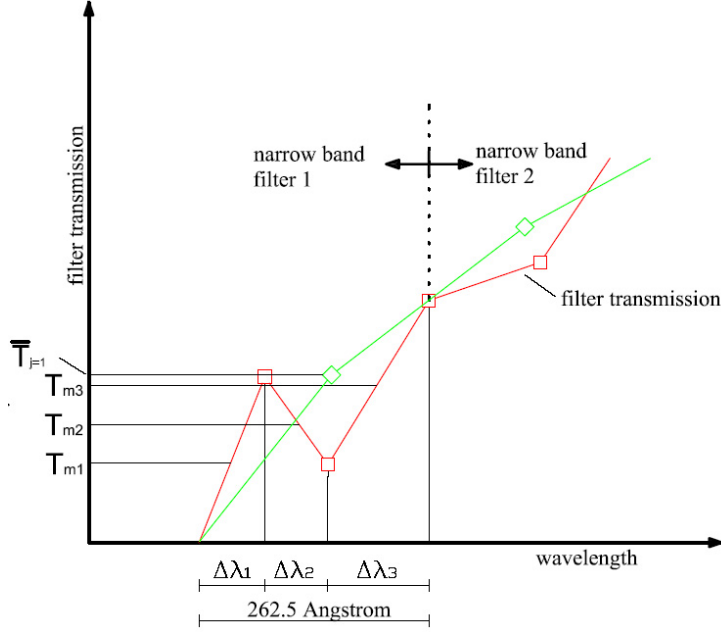


Figure 5.12: Schematic sketch of the weighted filter transmission calculation, here shown for one narrow band filter. The red line is the K-band filter transmission and the green line is the weighted filter transmission. The areas under the lines have the same size in each narrow band filter.

Visibility Functions of the K-Band - Different Calculations

In this section the effect of an incorrect calculation of the visibilities in broadbandfilters is investigated for two possible scenarios (the correct determination is described in the above section):

- We compare the synthetic visibility functions calculated incorrectly at the central wavelength of the K-band with the width of the true K-band and assuming a rectangular filter profile to the correct calculations of the visibility functions as described in the previous section (weighted with the K-band filter transmission and the model flux, Equ. 5.3). The differences (the visibilities calculated incorrectly are subtracted from the ones calculated correctly) between these two different calculations (in the following called K-band errors) are shown in Fig. 5.13 for the models with 2800 K and 3200 K and in Fig. 5.14 for the models with 2900 K and 3000 K along the spatial frequency with a blue dotted line. The K-band errors (right y-axis) are shown in a thousandth part of the absolute values. The visibility functions of the models are shown in Figs. 5.13 and 5.14 with a black solid line.
- Then we calculated the visibility functions in the K-band with the following formula:

$$V(S) = \frac{\sum_{j=1}^{20} (T_j \cdot \frac{F_j}{F_0} \cdot V_j)}{V(0)}, \quad (5.4)$$

with variables as defined above. There, the fact that squared visibilities are measured in observational astronomy is not considered. The differences (again, the visibilities calculated incorrectly are subtracted from the ones calculated correctly) between the calculations with Equ. 5.3 and Equ. 5.4 (in the following called V^2 -errors) is shown in Fig. 5.13 and in Fig. 5.14 with a red dotted line (again in a thousandth part of the absolute values).

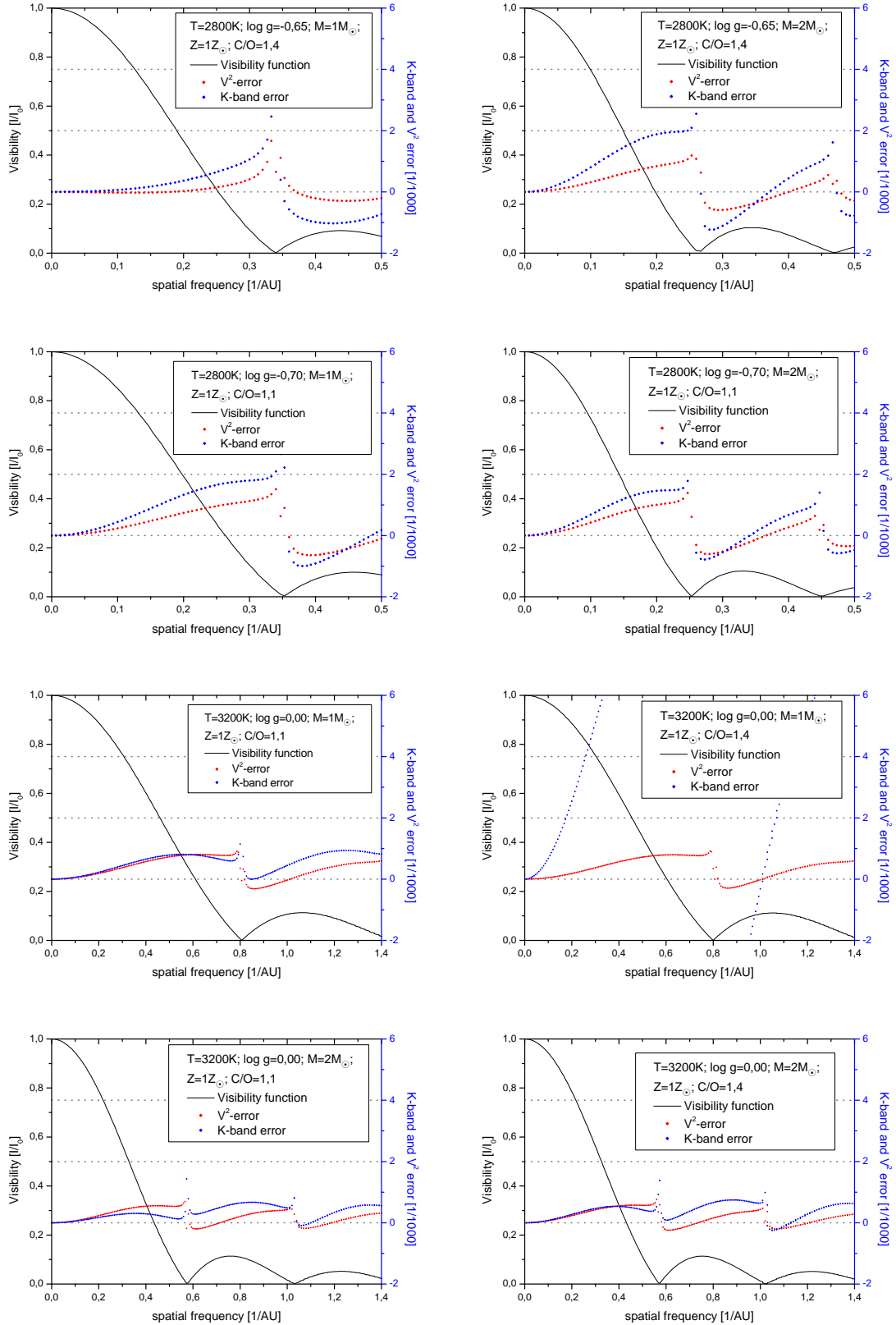


Figure 5.13: Differences between the different visibility calculations for the models with 2800 K and 3200 K. Shown are the deviations with and without using the squared visibility in the calculations (V^2 -errors, red dotted lines), the K-band errors (blue dotted lines) and the visibility functions (black lines) of the models. For the errors the ordinate is on the right side of the plots. For a detailed explanation see the text.

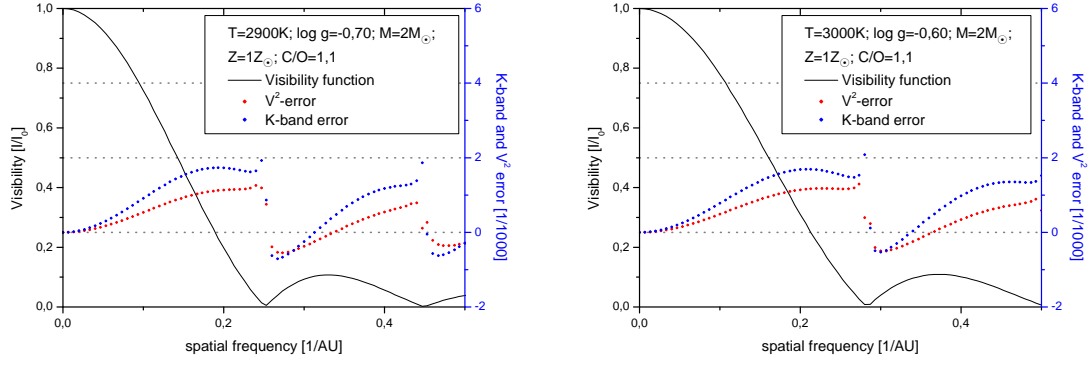


Figure 5.14: Differences between the different visibility calculations for the models with 2900 K and 3000 K. Shown are the deviations with and without using the squared visibility in the calculations (V^2 -errors, red dotted lines), the K-band errors (blue dotted lines) and the visibility functions (black lines) of the models. For the errors the ordinate is on the right side of the plots. For a detailed explanation see the text.

The following qualitative effects can be seen when we compare the K-band errors and the V^2 -errors of the different models:

- For the models with 2800 K, both errors have a maximum at the first zero point of the visibility functions. The maxima range from 1 - 2 ‰. The K-band errors (blue dotted line) are $\approx 1/2 - 1/3$ higher than the V^2 -errors (red dotted line).
- The models with 3200 K have their largest errors close to or at the zero points of the visibility functions or at the zero points of the visibilities. They reach values up to 1 ‰, except for the model with $T = 3200$ K; $\log g = 0.00$; $M = 1 M_{\odot}$; $Z = Z_{\odot}$; $C/O = 1.4$. There, the K-band errors reach values up to 10 ‰ at the first zero point of the visibility function. The reason for this large deviation compared to the other K-band errors could not be clarified.
- The overall shape of the errors of the 2900 K and 3000 K models (Fig. 5.14) is similar to the models with 2800 K, except that the K-band errors reach their maximum deviation shortly before the first zero point of the visibility function.

The measured K-band visibility of V460 Cyg is 0.704 ± 0.051 at a baseline of 37.08 m, the one of Z Psc is 0.810 ± 0.123 at a baseline of 38.21 m. The errors which result from an incorrect calculation of the model visibility functions are smaller than 2 ‰. They are thus much lower compared to the uncertainties of the observations.

Model Visibility Functions and Observed Visibilities

If the visibility functions obtained from the intensity distributions of model calculations are compared to observed visibilities, another wavelength dependent effect must be considered. It is called bandwidth smearing. At the baseline (which is one spatial frequency) of the interferometric observation, each monochromatic wavelength in the filter bandwidth induces one visibility function. The resulting visibility function is a superposition of all monochromatic visibility profiles. To describe this effect, the spatial frequencies are expressed in the units of the baseline (meter) and can be calculated for each monochromatic wavelengths in the used filter with the following equation:

$$B [m] = u [AU^{-1}] \cdot d [kpc] \cdot \lambda [\mu m] \cdot 206.265, \quad (5.5)$$

where B is the spatial frequency in meter, u the spatial frequency in AU^{-1} (as used before), d is the distance to the star in kpc and λ is the monochromatic wavelength. In this thesis, the monochromatic wavelengths are approximated with the central wavelengths of the parts of the splitted K-band (as discussed in the previous section). The bandwidth smearing in the K-band for V460 Cyg is shown for three models in Fig. 5.15. There, the left plots present the effects of band-width smearing on the visibility functions in the splitted K-band for the star V460 Cyg (Hipparcos distance: 631.5 pc). The weighted mean (red line) is again computed with Equ. 5.3 considering the K-band filter transmission (Fig. 5.10) and the model flux in the K-band.

The right graphs in Fig. 5.15 shows the differences in the visibilities when the effect of bandwidth smearing is taken into account (red visibility function) or not (black one). In the calculation of visibility functions which consider the effect of bandwidth smearing, the spatial frequencies are expressed in units of the baseline. For a comparison with the visibilities computed with Equ. 5.3, they are transformed into the unit AU^{-1} rewriting Equ. 5.5 and using the central wavelength ($\lambda = 2.2 \mu m$) of the K-band. The differences between these two calculations along the spatial frequencies are shown with a blue line in the right plots (right ordinates) of Fig. 5.15. They increase up to the first minimum of the visibility functions and reach values up to 2%. This effect has to be considered when comparing model visibility functions to observed visibilities. It is particularly very pronounced when operating with observed visibilities which are located around the first zero points of the visibility function. In contrast to the K-band error and the V^2 error (Figs. 5.13 5.14) the effect of bandwidth smearing is much more pronounced. The errors resulting from it are roughly ten times higher than the ones from the K-band error and the V^2 error.

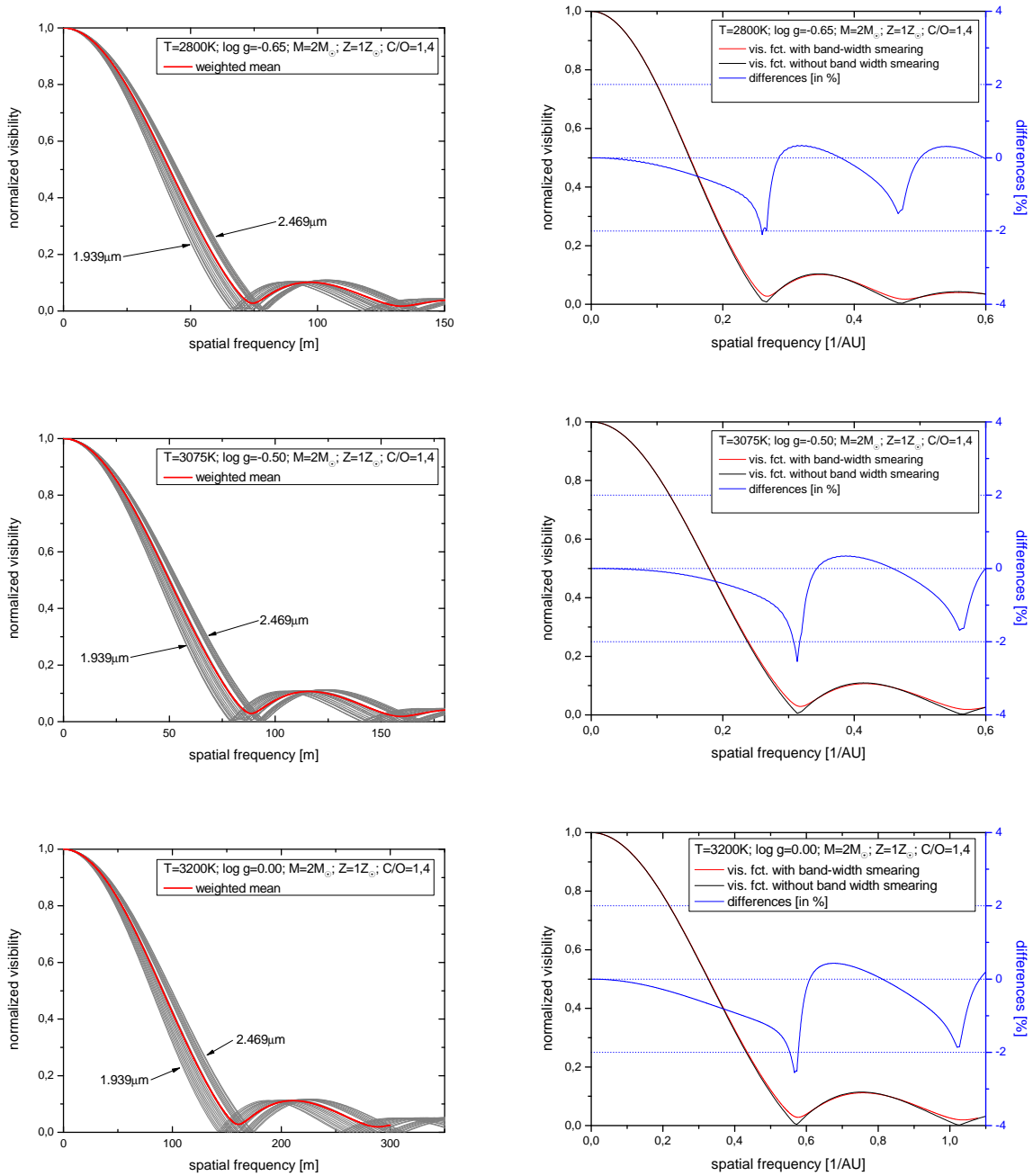


Figure 5.15: Influences of band-width smearing on the model visibility function. Here shown for the K-band observation of the star V460 Cyg (Hipparcos distance: 631.5 pc). In the left plots the visibility functions calculated with Equ. 5.5 in the splitted K-band are presented. In this computation, the spatial frequencies are expressed in units of the baseline (meter). The superposition of the visibility profiles in the splitted K-band (red line) is again calculated with a weighted mean considering the filter transmission and the model flux in the K-band. The right plots show the differences between the visibility calculations whether the effect of band width smearing is taken into account (calc. with Equ. 5.15) or not (calc. with Equ. 5.3). Hence, the spatial frequencies of the visibility functions which include the effect of bandwidth smearing are transformed in the unit AU^{-1} with Equ. 5.15. The differences (visibilities without bandwidth smearing are subtracted from the one considering it) reach values up to 2% around the first minimum of the visibility function.

5.2 Models and the HRD

Here we compare our models (especially the temperature and the bolometric luminosity) to AGB evolutionary tracks from Bessel (1989, [10]). These evolutionary tracks are available for different masses and metallicities. Here shown are the ones with solar metallicity and with the metallicity of the Large Magellanic Cloud (LMC). The latter is $Z = 0.008$ corresponding to $\approx 1/3$ of the solar value. The model parameters from the models which are presented in Fig. 5.16 are listed in Tab. 5.2. The required parameters to plot a HRD are the effective temperature (x-axis) and the bolometric magnitude (M_{bol}) or the luminosity (L). These two values can be converted into each other with the following relation:

$$M_{bol} - M_{bol,\odot} = -2.5 \cdot \log \frac{L}{L_{\odot}}, \quad (5.6)$$

with $M_{bol,\odot} = 4.75$ and $L_{\odot} = 3.9 \cdot 10^{26}$ W.

$M [M_{\odot}]$	$T_{eff} [K]$	C/O	$L [L_{\odot}]$	$R [R_{\odot}]$	$M_{bol} [mag]$
1	2800	1.1	7563	370.6	-4.98
1	2800	1.4	7563	370.6	-4.98
2	2800	1.1	15125	524.1	-5.73
2	2800	1.4	13480	494.8	-5.60
2	2900	1.1	17404	524.1	-5.88
2	3000	1.1	15833	467.1	-5.78

Table 5.2: Some parameters of the models. Each model is calculated with solar metallicity.

With the parameters of Tab. 5.2 we can plot a Hertzsprung Russell diagram (Fig. 5.16) and compare the models with AGB evolutionary tracks from Bessel (1989, [10]). It can be seen that our models are located in the regions covered by these tracks. However, the location of our models in the HRD would require somewhat higher masses or lower luminosities than they were assumed by us (1 and $2 M_{\odot}$).

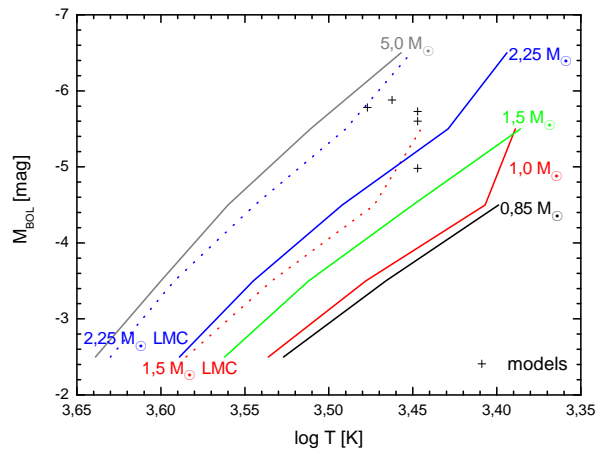


Figure 5.16: Hertzsprung Russell Diagram with AGB evolutionary tracks of Bessel et al. (1989, [10]). Shown are the tracks for solar composition for 0.85, 1, 1.5, 2.25 and $5 M_{\odot}$ (solid lines) and LMC abundances for 1, $2.25 M_{\odot}$ (dotted lines). The black crosses denote our models.

5.3 Model Structure

In this section we discuss the dependence of some physical quantities like the temperature, the opacity, the density, the gas pressure and the abundances of some important molecules on the atmospheric depth in a hydrostatic model. We show plots for two atmospheres. These are the models with $T = 2800$ K; $\log(g [cm/s^2]) = -0.65$; $M = 2 M_{\odot}$; $Z = Z_{\odot}$; $C/O = 1.4$ and $T = 2800$ K; $\log(g [cm/s^2]) = -0.70$; $M = 2 M_{\odot}$; $Z = Z_{\odot}$; $C/O = 1.1$. The radial behaviour of the denoted above quantities is shown in Fig. 5.17:

- The density (red line, 2nd left y-axis) is shown in a linear scale in units of g/cm^3 on the 1st left y-axis.
- The Rosseland mean opacity [cm^{-1}] (blue line) is presented in a logarithmic scale on the 2nd left y-axis.
- The scale for the temperature [K] (gray) is displayed on the first right y-axis.
- The scale for the gas pressure [dyn/cm^2] is shown on the second right y-axis: In the diagrams, the total gas pressure (p_{ges} , Fig. 5.17) and the partial pressures of some molecules (Figs. 5.19 and 5.20), which are predominant in carbon stars, are shown. Fig. 5.19 presents the diatomic molecules CO , CN , CH and C_2 and Fig. 5.20 the polyatomic molecules C_2H_2 , HCN , C_3 (and CO).

These quantities are plotted as a function of the radius. The radial extension of the considered models corresponds to a range from 2.1 to 2.9 AU. The model calculations contain the molecules H_2 , H_2O , CO , CN , CH , C_2 , TiO , HCN , C_3 , SiO , C_2H_2 , OH , VO , CO_2 , SO_2 , HF , HCl , CH_4 , FeH , CrH , ZrO , YO , the atoms H , C , N , O and the ions H^+ , C^+ , N^+ and O^+ . In Fig. 5.18 the spectral energy distributions (resolution $R = 200$) of the here discussed models are displayed. Because of their importance for the opacity in carbon stars, the profiles of the total gas pressure and the partial pressures of the molecules CO , HCN , CH , CN , C_2H_2 , C_2 , and C_3 are shown in Figs. 5.19 and 5.20. The absorption features of these molecules can be identified in Fig. 5.18 in the visible and the near infrared spectral range (due to C_2 and CN), at $1.7 \mu m$ (due to CO , C_2H_2 and HCN), at $2.1 \mu m$ (due to CO and C_2H_2), at $2.5 \mu m$ (due to HCN), at $3 \mu m$ (due to HCN and C_2H_2) and at $4.5 \mu m - 5 \mu m$ (due to CO and C_3).

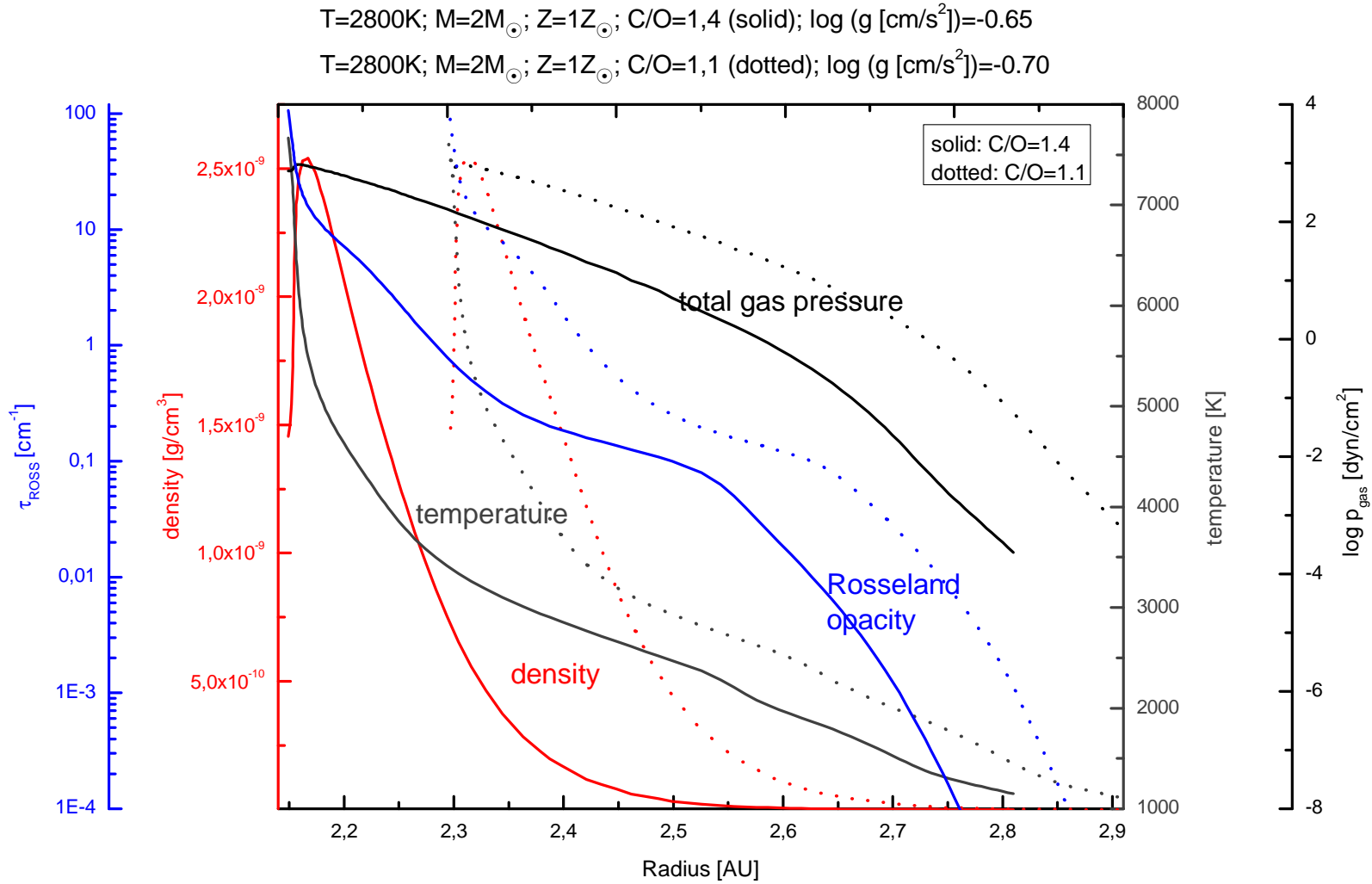


Figure 5.17: Profiles of the density, the Rosseland mean opacity, the temperature and the total gas pressure along the stars' radius. Here shown for the models with $T = 2800\text{K}$; $\log(g [\text{cm/s}^2]) = -0.65$; $M = 2M_{\odot}$; $Z = Z_{\odot}$; $C/O = 1.4$ and $T = 2800\text{K}$; $\log(g [\text{cm/s}^2]) = -0.70$; $M = 2M_{\odot}$; $Z = Z_{\odot}$; $C/O = 1.1$.

Some interesting facts can be seen when we compare the partial pressure structures of the different molecules and the different models:

- The profiles of the partial pressures of the models with $C/O = 1.1$ and $C/O = 1.4$ show a qualitatively similar behaviour. The difference is that the model with $C/O = 1.1$ has a larger extension because of the lower gravitational acceleration.
- The partial pressures of all the presented molecules show a strong decrease at temperatures higher than 5000 K. This corresponds to a radius of 2.2 AU (2.3 AU) for the model with $C/O = 1.1$ ($C/O = 1.4$). Because of the increasing temperature in this region, the molecules cannot form due to the high thermal velocity of the gas.
- The molecule with the highest partial pressure in Fig. 5.19 is CO . The partial pressures of molecules like H_2 or N_2 are higher than the one of CO . They are not shown here because of their marginal influence on the spectra of carbon stars.
- Beside CO , the partial pressures of HCN and C_2H_2 get very high in the outer regions of the models (> 2.55 AU at $C/O = 1.4$ and > 2.60 AU at $C/O = 1.1$).
- The partial pressure of C_2 is roughly constant from 2.2 AU (2.35 AU) to ≈ 2.55 AU (2.65 AU) for $C/O = 1.4$ ($C/O = 1.1$) and it decreases strongly in the regions with radii > 1.9 AU.
- The partial pressure of C_3 increases slightly from 2.2 AU (2.35 AU) to ≈ 2.55 AU (2.65 AU) for $C/O = 1.4$ ($C/O = 1.1$). A strong decrease follows in the outer regions.
- The partial pressure of C_2H_2 increases slightly from 2.2 AU (2.35 AU) to ≈ 2.55 AU (2.65 AU) for $C/O = 1.4$ ($C/O = 1.1$). A slight decrease follows in the outer regions.
- The partial pressures of the molecules CN and CH show similar characteristics. A slight decrease up to ≈ 2.55 AU (≈ 2.65 AU) at $C/O = 1.4$ ($C/O = 1.1$) is followed by a strong decrease for larger radii.
- The bulge which can be seen in the outer regions of most of the center to limb variations in Fig. 5.2 and Fig. 5.3 can be associated with the bulge in the Rosseland opacity in Fig. 5.17 and the partial pressure behaviour of C_2H_2 , HCN and C_3 .

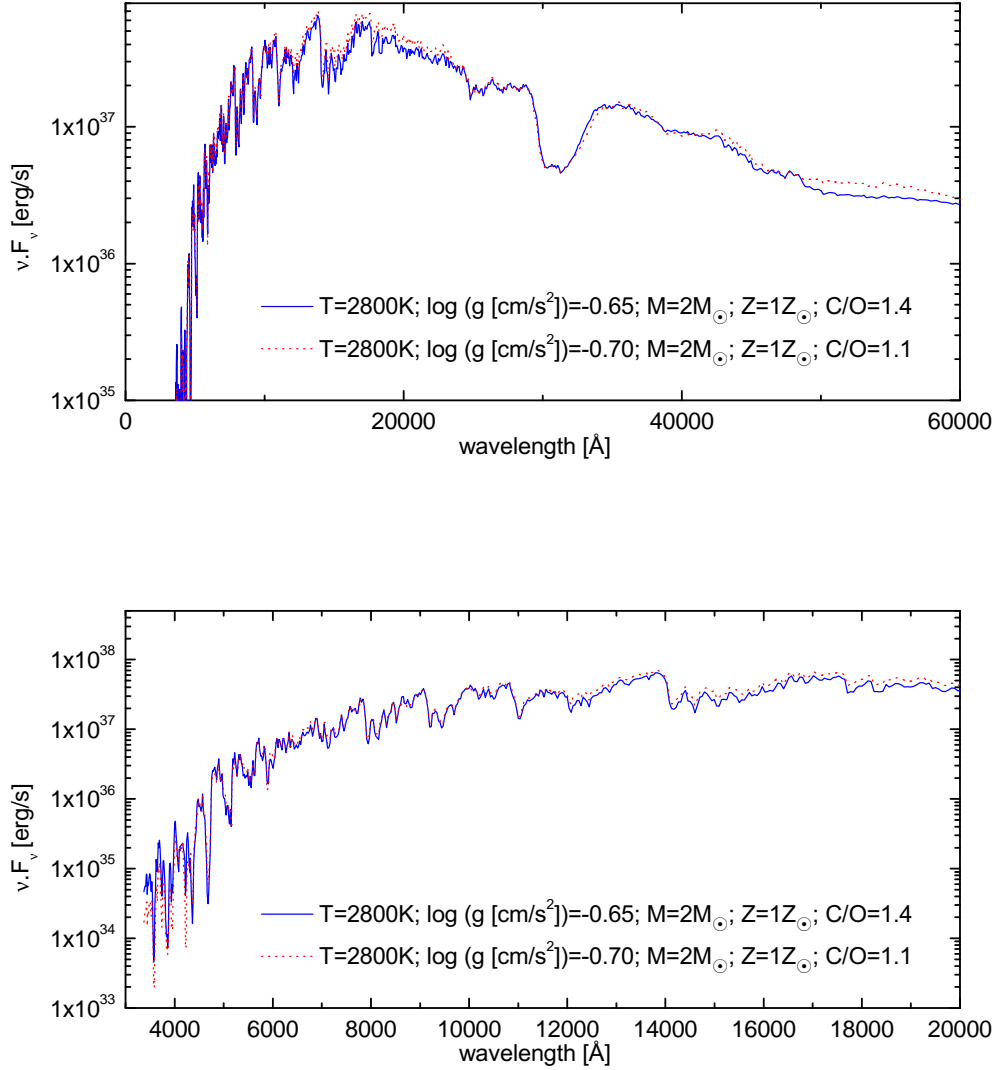


Figure 5.18: Spectral energy distributions of the models with $T = 2800 \text{ K}$; $\log(g [\text{cm/s}^2]) = -0.65$; $M = 2 M_{\odot}$; $Z = Z_{\odot}$; $C/O = 1.4$ (blue solid line) and $T = 2800 \text{ K}$; $\log(g [\text{cm/s}^2]) = -0.70$; $M = 2 M_{\odot}$; $Z = Z_{\odot}$; $C/O = 1.1$ (red dotted line). The upper panel shows the wavelength region up to $60 \mu\text{m}$, the lower panel shows the visible spectral range and the near infrared up to $2 \mu\text{m}$ in more detail.

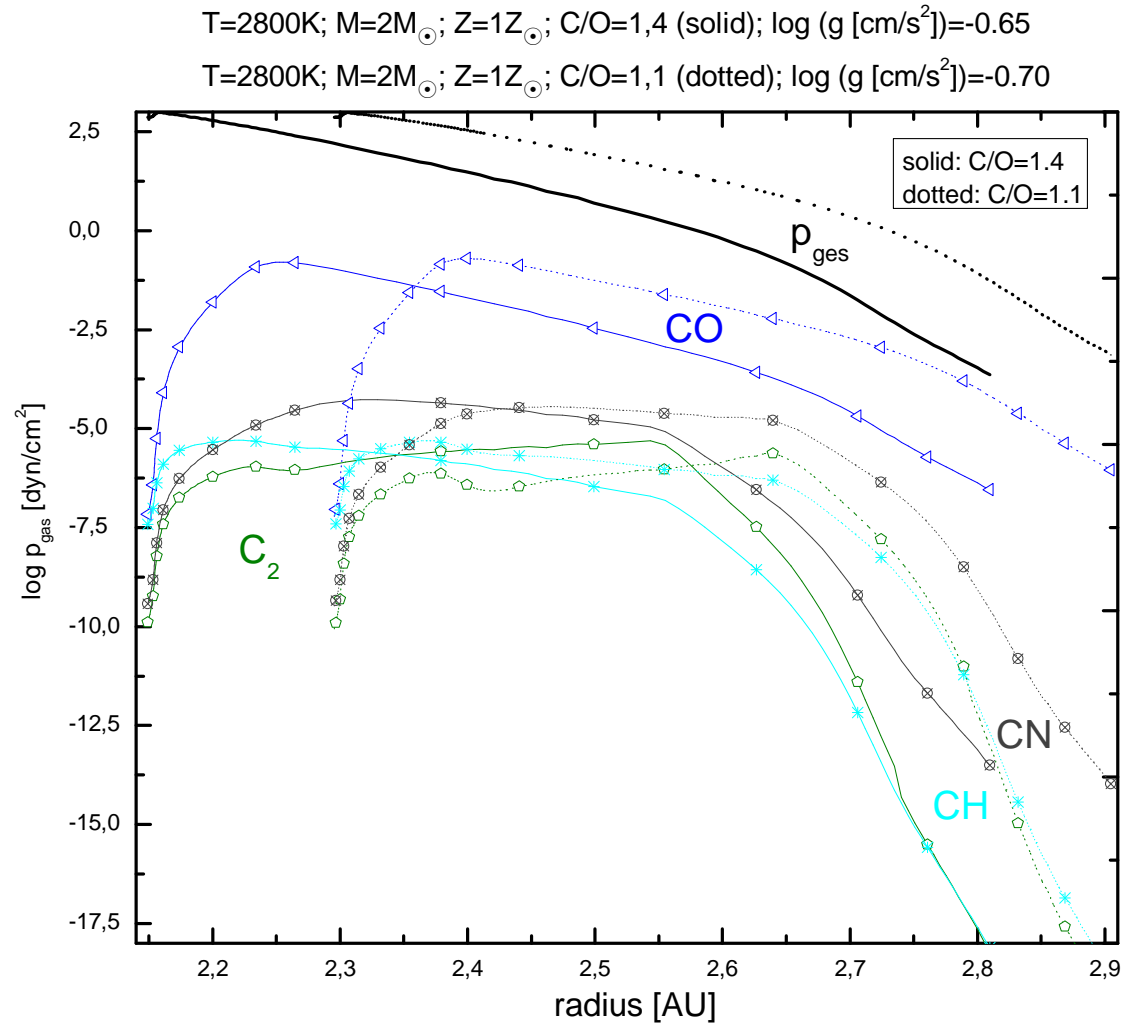


Figure 5.19: Profiles of the total gas pressure and the partial pressures of the diatomic molecules CO , CH , CN and C_2 along the stars' radius. Here shown for the models with $T = 2800 \text{ K}$; $\log(g [\text{cm/s}^2]) = -0.65$; $M = 2 M_{\odot}$; $Z = Z_{\odot}$; $C/O = 1.4$ and $T = 2800 \text{ K}$; $\log(g [\text{cm/s}^2]) = -0.70$; $M = 2 M_{\odot}$; $Z = Z_{\odot}$; $C/O = 1.1$.

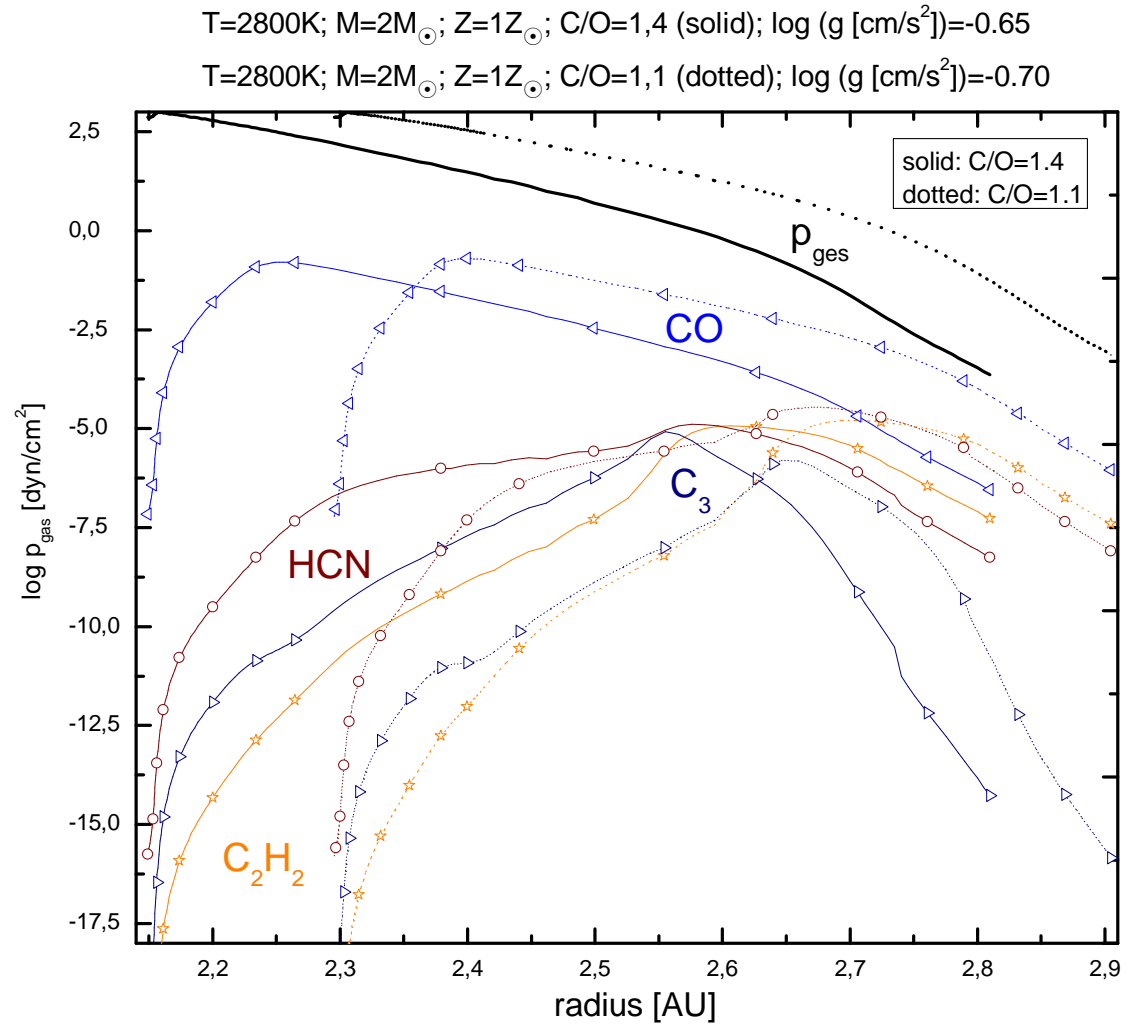


Figure 5.20: Profiles of the total gas pressure and the partial pressures of the polyatomic molecules CO , C_2H_2 , HCN and C_3 along the stars' radius. Here shown for the models with $T = 2800\text{K}$; $\log(g [\text{cm/s}^2]) = -0.65$; $M = 2M_{\odot}$; $Z = Z_{\odot}$; $C/O = 1.4$ and $T = 2800\text{K}$; $\log(g [\text{cm/s}^2]) = -0.70$; $M = 2M_{\odot}$; $Z = Z_{\odot}$; $C/O = 1.1$.

Chapter 6

Best-Fit Model

How can we find now the model best fitting the observed spectra and the visibility? This is done by a comparison between the observed spectra and the ones calculated from hydrostatic COMARCS, MARCS - atmospheres. Sec. 6.1 shows that it is possible to interpolate linearly between our model spectra in a first approximation. This was done in order to test the feasibility of an interpolation in the existing grid of models to obtain the best-fit parameters. In Sec. 6.2 we compare the model spectra to the ISO data of V460 Cyg. In Sec. 6.3 and 6.4 we study the synthetic spectra together with the visible spectra of V460 Cyg/Z Psc and in Sec. 6.5 the parameters of the chosen best-fit model are defined. The spectra, which are shown in this chapter have a resolution of $R = 200$ and are binned down from high resolution opacity sampling spectra ($R = 10000$). There, a microturbulence velocity of $\xi = 2.5$ km/s was assumed (Aringer et al. (2008, in preparation, [1])).

6.1 Interpolation of Spectra

When we look at the atmospheres which are used in this thesis (Tab. 5.1), we see that the gaps between the parameters are much too large to define a best-fit model. E.g., the step width in temperature between the models is 100 K and the various models are only calculated for two different C/O values (1.1 and 1.4). Because of this limited number of available parameters we examined if it is possible to interpolate linearly between the model spectra. For the effective temperature we validated the possibility to do this in the following way: We took atmospheres which only differ in the temperature (keeping other model parameters constant). This is the case for the calculations with $T_{eff} = 3000$ K, $T_{eff} = 3100$ K and $T_{eff} = 3200$ K; $\log(g [cm/s^2]) = -0.50$; $M = 2M_{\odot}$; $Z = Z_{\odot}$; $C/O = 1.1$ or $C/O = 1.4$. Then we interpolated linearly between the models with 3000 K and 3200 K to obtain the one with 3100 K. This was done for the atmospheres with $C/O = 1.1$ and $C/O = 1.4$. The interpolated 3100 K model is then compared to the one taken from the grid. This is shown in Fig. 6.1. As it can be seen in this figure, the deviations between the original 3100 K spectrum (red spectrum) and the interpolated one (black dotted spectrum) are quite small. This confirms the assumption that it is possible to interpolate linearly between model spectra in this small temperature range as a first approximation.

With the above mentioned models we then produced a model grid with a linear interpolation (extrapolation) in the temperature range of 3000 to 3200 K in steps of 25 K and from $C/O = 1.1$ to $C/O = 1.6$ in steps of 0.1. The spectra with $C/O = 1.5$ and 1.6 are extrapolated from the models with $C/O = 1.1$ and 1.4. With the grid of atmo-

spheres available for this thesis the linear interpolation in C/O could not be validated in the same way as the temperature interpolation, because we only have two different C/O values. Nevertheless, studies covering a larger sample of C/O ratios demonstrate that it will work quite well. The change of intensity of the main molecular absorption features as a function of C/O behaves in quite regular way (Aringer et al. (2008, in preparation, [1])).

6.2 V460 Cyg - Fit of ISO Spectrum

In this section the ISO-SWS spectrum of V460 Cyg (Fig. 4.2) is compared to the results from model calculations. It has a resolution of $R \approx 200$ (Aoki et al. (1998, [5])) and can therefore be compared to the synthetic ones ($R = 200$) without any binning. A first restriction of the model parameters could be made by a visual inspection. It was immediately clear that the ISO spectrum of V460 Cyg cannot be reproduced by the synthetic ones based on $T_{eff} = 2800$ K since the molecular bands are far too strong in such models. Similarities between the observed and the model spectra appeared at a temperature of 3100 K and at a C/O ratio of 1.4 for the atmospheres with $\log(g [cm/s^2]) = -0.50$; $M = 2 M_{\odot}$ and $Z = Z_{\odot}$. Hence, we compared the ISO spectrum to the small model grid covering $T_{eff} = 3000 - 3200$ K and $C/O = 1.1 - 1.6$ which was produced before with a linear interpolation for the models with $C/O = 1.1 - 1.4$ and with an extrapolation for $C/O = 1.5 - 1.6$.

The ISO spectrum (Fig. 4.2) covers a wavelength range from $2.38 \mu m$ to $45.2 \mu m$. There are two dominant absorption features in the short wavelength region in the spectrum of V460 Cyg. The first band can be found at $3 \mu m$ and is mainly due to the molecules C_2H_2 and HCN . The second one is situated at $5 \mu m$ and is caused by CO ($> 4.25 \mu m$) and C_3 ($4.75 \mu m - 5.75 \mu m$). How do these absorption features respond to a change in the temperature and in the C/O ratio (Fig. 6.2)?:

- The C_2H_2 and HCN band at $3 \mu m$ is very sensitive with regard to changes in temperature. It grows in strength towards cooler models. This feature is hardly existent at a temperature of 3200 K. Already at 3000 K it is very pronounced. The CO and C_3 band at $5 \mu m$ varies only slightly with temperature. A small increase in the band strength for lower temperatures can be identified.
- The following remarks about the dependency of the absorption features on the C/O ratio are only valid for a C/O ratio higher than one: For temperatures higher than 3000 K the $3 \mu m$ band becomes stronger at a lower C/O ratio. This is because the HCN molecule is the dominating feature in warmer models because it consists of one carbon atom (the more free carbon is available, the more molecules with a higher amount of carbon atoms are produced compared to species including only one C-atom). At temperatures lower than 3000 K, this feature is mainly due to C_2H_2 .

The band strength on the short wavelength side of the $5 \mu m$ feature, which is due to CO , is marginally influenced by a change in the C/O ratio. The longer wavelength part of the $5 \mu m$ band, which is due to C_3 , increases with an increasing C/O ratio. The intensity ratio of this C_3 band to the HCN band at $3 \mu m$ can be used as a sensitive tool for a measurement of the C/O ratio. It strongly increases with an increasing C/O ratio. (Jørgensen et al. (2000, [36])). The reason for this is that the molecules have roughly the same temperature dependencies, because both are composed of three atoms and both have approximately the same dissociation

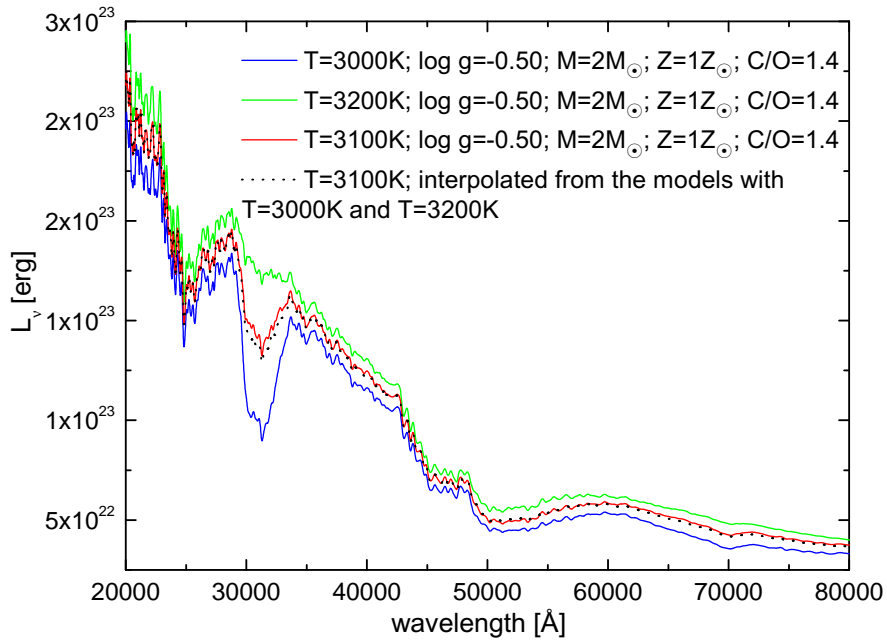
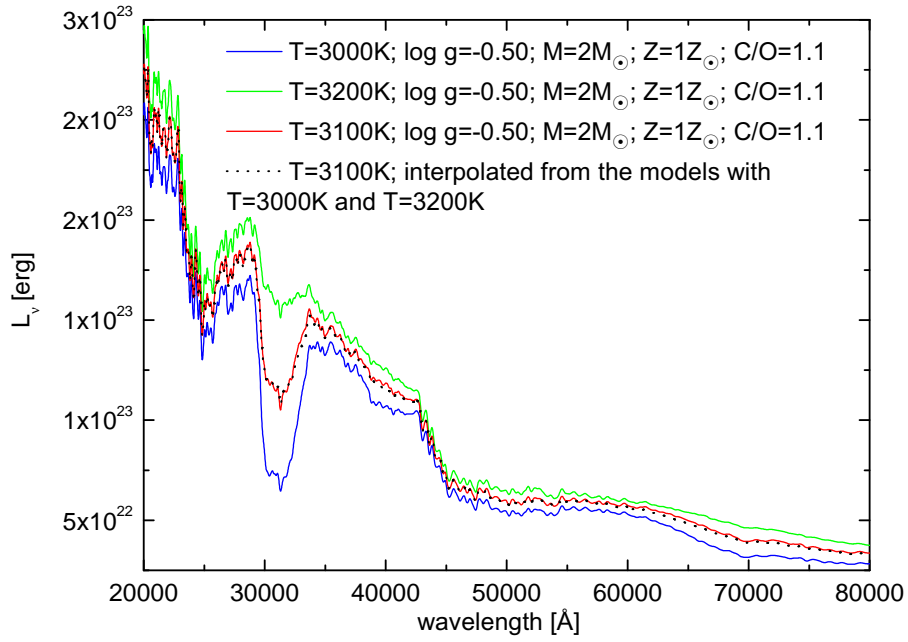


Figure 6.1: Validation of the linear interpolation in temperature between the synthetic model spectra ($R = 200$). Shown are the interpolated 3100 K spectrum (black dotted line), the ones with 3000 K (blue), with 3200 K (green) and the original 3100 K spectrum (red) for $C/O = 1.1$ (upper graph) and 1.4 (lower graph) in the wavelength range from 2 to 8 μm .

energies. Otherwise, the C_3 molecule consists of 3 C-atoms and the HCN molecule only of one. Therefore, the amount of C_3 is a function of the number density of the free carbon atoms to the third power (the greater the C/O ratio the more free carbon is available).

Which part of the ISO-SWS range is now best to compare the observations to the model spectra to determine the best-fit model? We chose the wavelength interval from $2.4\ \mu\text{m}$ to $5.6\ \mu\text{m}$ due to the following reasons:

1. Because of the sensitivity of the bands at $3\ \mu\text{m}$ and $5\ \mu\text{m}$ to the temperature and the C/O ratio.
2. The ISO spectrum shows the biggest uncertainties at wavelengths longer than $10\ \mu\text{m}$. This can be seen by the increasing standard deviation in the observed ISO spectrum at wavelengths $> 10\ \mu\text{m}$ (Fig. 4.2).
3. The observed ISO spectrum has a higher flux than the synthetic ones at wavelengths $> 10\ \mu\text{m}$ (Fig. 6.4). This is a general problem of all hydrostatic model calculations. Jørgensen et al. (2000, [36]) found it to be unlikely that this discrepancy is an artefact of the data reduction of the ISO-SWS spectra. A possible explanation is given in the following paragraph.
4. The band at $14\ \mu\text{m}$, which is mainly caused by C_2H_2 and HCN , is not very pronounced in the observed ISO spectrum. This feature is very strong in model calculations (Fig. 6.4).

Point 3 and 4 also appeared in the study of Jørgensen et al. (2000, [36]). There, the ISO-SWS spectra of 3 carbon stars (TX Psc, V460 Cyg and TT Cyg) were compared to model calculations based on hydrostatic model atmospheres. The main difference in comparison to our models is that they used a plane-parallel model geometry. The authors of this study give the following tentative explanation to the deviations between the model spectra and the observed spectra at wavelengths longer than $10\ \mu\text{m}$: The flux excess beyond $8\ \mu\text{m}$ originates from a continuous emission source on top of the star's photosphere. The authors came to their conclusions after performing simulations with DUSTY (Ivezic & Elitzur (1995, [35])). DUSTY is a dust-envelope spectrum computation program and it describes the radiative transport in a (circular symmetric) circumstellar dusty envelope. The input data is the photospheric spectrum of the central star. From these simulations it followed that the whole stellar surface could not be covered with this continuous emission source (because the flux excess at wavelength longer than $\approx 8\ \mu\text{m}$ is much too high). A simple flux adjustment leads to the result that approximately 10% of the stellar photosphere is covered by clumps of dust-rich cool gas. The emission of these clumps is responsible for the excess flux in the observed spectrum and the filling up of the $14.0\ \mu\text{m}$ band. Otherwise, the deviations to the strong photospheric feature, which occurs in the (photospheric) synthetic model spectra at $14\ \mu\text{m}$ cannot be explained. The small bands at $13.7\ \mu\text{m}$ and at $14.0\ \mu\text{m} - 14.3\ \mu\text{m}$, which appear in the observed spectrum, are produced due the absorption of a cool ($< 600\ \text{K}$), C_2H_2 rich gas which is located on top of the clumps of the dust-rich cool gas.

However, the authors suggest that dynamical phenomena in the outer atmospheres may also play some role.

In former studies (e.g. Tsuji et al. (1997, [66]) or Yamamura et al. (1999, [77])), the deviations between the computed and the observed $14\ \mu\text{m}$ band were explained with the

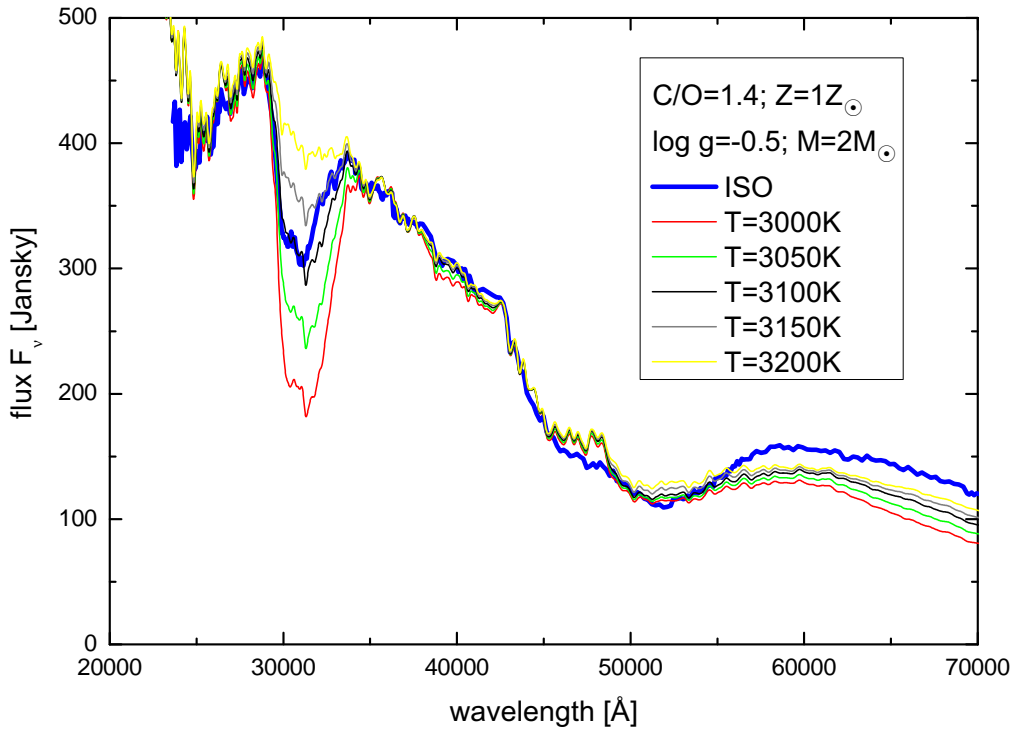
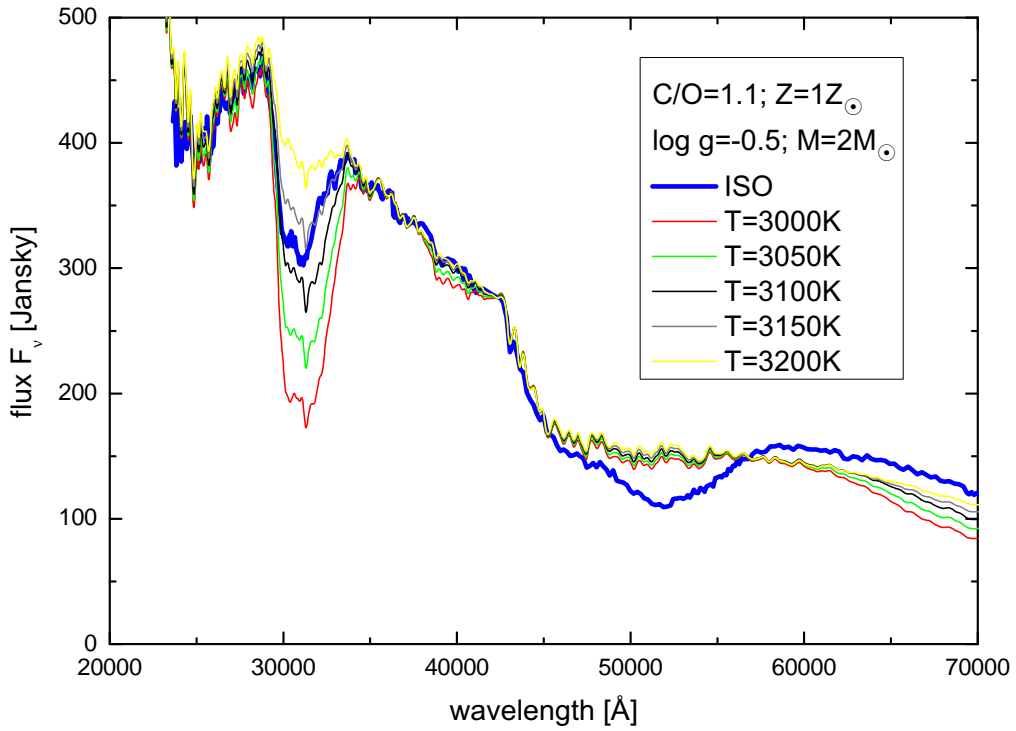


Figure 6.2: The $3\ \mu\text{m}$ and the $5\ \mu\text{m}$ band and their sensitivity to the temperature and to the C/O ratio. Shown are the observed ISO spectrum (thick blue line) and the model spectra from 3000 K to 3200 K in steps of 50 K of the models with $Z = Z_{\odot}$ and $M = 2 M_{\odot}$ and $\log g = -0.50$ for $C/O = 1.1$ (upper graph) and $C/O = 1.4$ (lower graph).

existence of a so-called warm molecular envelope. There, layers of dense molecular gas are assumed to surround the star's photosphere. The strength of the bands can be matched to the observed ones by adjusting the temperature and the density of the molecular gas in the envelope. Jørgensen et al. (2000, [36]) excluded a warm molecular envelope around the three carbon stars because of the following reason: The $14\ \mu\text{m}$ band is generated due to C_2H_2 absorption. A weakening in the $14\ \mu\text{m}$ band (which is observed) originating from the absorption of a dense molecular envelope should also cause a weakening in the C_2H_2 part of the $3\ \mu\text{m}$ band, because both bands have roughly the same behaviour as a function of temperature (the intrinsic transition probabilities of the two bands and the excitation energies of the vibrational levels are very similar). This weakening in the $3\ \mu\text{m}$ band is not observed. The models of Jørgensen et al. (2000, [36]) provide an accurate description of this feature. Therefore it is not likely that the deviations in the $14\ \mu\text{m}$ region are produced from a warm molecular envelope.

We used the wavelength range from $3.6\ \mu\text{m}$ to $3.8\ \mu\text{m}$ to normalize the model spectra to the observed ISO spectrum. This region lies between the two dominant absorption features and is close to the continuum.

To find the best-fit model we then calculated the root mean square error between the interpolated model spectra and the observed ISO data in the wavelength range from $2.4\ \mu\text{m}$ to $5.6\ \mu\text{m}$. Since the sampling points of the available synthetic spectra differ from the ones of the ISO spectrum we made a linear interpolation of each spectrum (each model spectrum and the observed ISO spectrum) with 60000 sampling points in the wavelength range from $2.4\ \mu\text{m}$ to $5.6\ \mu\text{m}$. This results in constant wavelength gaps between the sampling points. The error between the observed and the synthetic spectra is then calculated at each sampling point. The root mean square error (RMSE) in the whole wavelength range from $2.4\ \mu\text{m}$ to $5.6\ \mu\text{m}$ is

$$RMSE = \sqrt{\frac{\sum_{i=1}^n (x_{Obs.,i} - x_{Mod.,i})^2}{n}}, \quad (6.1)$$

where $x_{Obs.,i} - x_{Mod.,i}$ is the flux deviation between the observed and the synthetic spectra at the sampling point i and n is the number of the sampling points ($n = 60000$). The root mean square error of each interpolated model is shown in Fig. 6.3. The abscissa in this figure gives the different interpolated (extrapolated) C/O ratios from 1.1 to 1.6 and the ordinate gives the RMSE for the models with temperatures from $T_{eff} = 3000\ \text{K}$ to $T_{eff} = 3200\ \text{K}$ in steps of $\Delta T = 25\ \text{K}$. The error bars are calculated with a simple error estimation using the standard deviation of the ISO spectrum: We defined an upper/lower limit of the ISO spectrum by adding/subtracting the standard deviation to its flux at each sampling point. Then, the RMSE is calculated as before. The error bars in Fig. 6.3 show the deviation between the RMSE calculated with the 'normal' ISO spectrum and the RMSE calculated with the ISO spectrum with the added/subtracted standard deviation. The error bars are quite small in comparison to the differences of the RMSEs between the different models. When we neglect the uncertainties which result from the interpolation of each spectrum to calculate the RMSE, this permits a rather unambiguous determination of the parameters of the best-fit model. They are at a C/O of 1.3, 1.4 or 1.5 and at a temperature between $T_{eff} = 3050\ \text{K}$ and $3100\ \text{K}$. The model with $T_{eff} = 3050\ \text{K}$ and $C/O = 1.6$ has roughly the same RMSE as the ones at $C/O = 1.4$. Because of the relatively high errors of the neighbouring models ($T_{eff} = 3025\ \text{K}$ and $T_{eff} = 3075\ \text{K}$) at $C/O = 1.6$ and due to the fact that the atmospheres at $C/O = 1.6$ are extrapolated from the models with $C/O = 1.1$ and $C/O = 1.4$ (the uncertainties in the extrapolated models are probably higher than in the interpolated ones) we excluded this model from

the possible best-fit solutions. The best-fit model is defined as the model with the smallest RMSE. This is the one with $T_{eff} = 3075$ K; $\log(g [cm/s^2]) = -0.50$; $M = 2 M_{\odot}$; $Z = Z_{\odot}$; $C/O = 1.4$. Then we calculated a COMARCS model with exactly these parameters to check how good the agreement between the interpolated model and the computed one is. The computed model is shown with a blue cross in Fig. 6.3. The deviation between the two is quite small compared to the error bars. This again confirms the possibility to interpolate linearly between model spectra in a small parameter range.

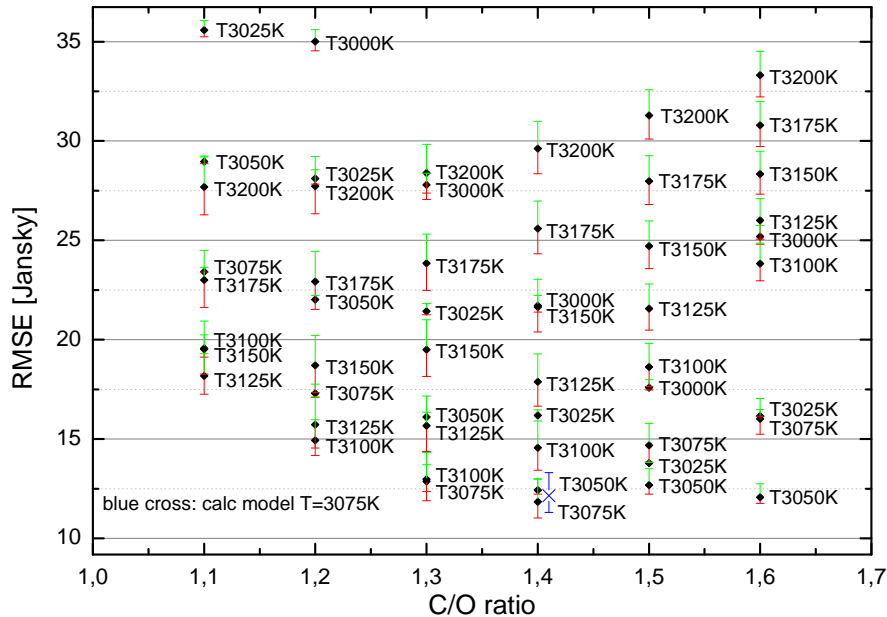


Figure 6.3: Root mean square error calculated from differences between the interpolated models (for $Z = Z_{\odot}$ and $M = 2 M_{\odot}$ and $\log(g [cm/s^2]) = -0.50$) and the ISO-SWS spectrum in the wavelength range from $2.4 \mu\text{m}$ to $5.6 \mu\text{m}$. The error bars are calculated using the standard deviation of the ISO spectrum. A synthetic spectrum based on a COMARCS model with the parameters of the interpolated model with the smallest error ($T_{eff} = 3075$ K; $\log(g [cm/s^2]) = -0.50$; $M = 2 M_{\odot}$; $Z = Z_{\odot}$; $C/O = 1.4$) was then calculated (blue cross). The difference between the interpolated and the calculated model is rather small. The orange cross shows the RMSE for the model with the parameters $T_{eff} = 3050$ K; $\log(g [cm/s^2]) = -0.50$; $M = 2 M_{\odot}$; $Z = Z_{\odot}$ and a $C/O = 1.4$.

In Fig. 6.4 we plot the best-fit model spectrum and the ISO spectrum. The upper graph shows the wavelength region which was used for the calculation of the best-fit model ($2.4 \mu\text{m}$ to $5.6 \mu\text{m}$). The lower graph covers the wavelength region from $2 \mu\text{m}$ to $20 \mu\text{m}$. The best-fit model spectrum reproduces the overall shape of the pseudo-continuum and the two dominant absorption features of the ISO data very well. However, the shape of the C_2H_2 and HCN feature at $3 \mu\text{m}$ in the ISO spectrum shows little differences to the model. The bulge from $4.6 \mu\text{m}$ to $4.9 \mu\text{m}$ which occurs in the model spectrum does not appear in the observed one. Longwards of the C_3 feature, in the range from $\approx 5.6 \mu\text{m}$ to $7.5 \mu\text{m}$ the observed spectrum shows a higher flux than the model. This excess occurs in all of the calculated models. A reason for this deviation and the missing of the bulge in the $5 \mu\text{m}$ feature of the observed ISO spectrum can be that the molecular opacities are not well known. We assume that the deviations from $2.38 \mu\text{m}$ to $2.45 \mu\text{m}$ (in this region the absorption features are produced from HCN , CO , CN and C_2) have the same reason.

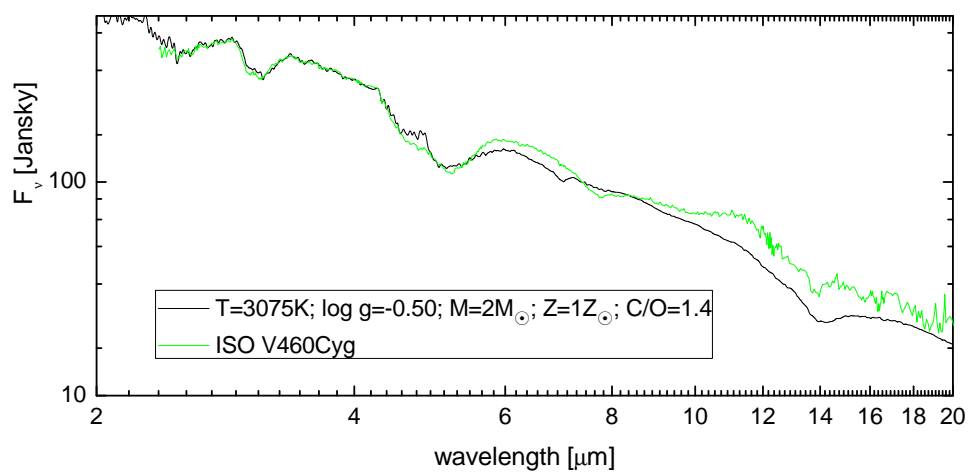
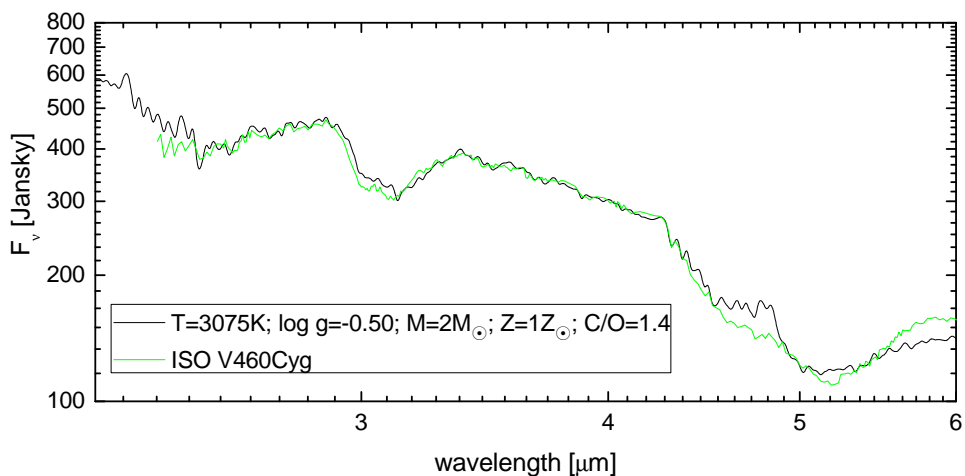


Figure 6.4: Comparison between the best-fit model spectrum ($T_{eff} = 3075 \text{ K}$; $\log(g [cm/s^2]) = -0.50$; $M = 2 M_{\odot}$; $Z = Z_{\odot}$; $C/O = 1.4$, black line) and the ISO spectrum (green line). The upper graph shows the wavelength range from $2 \mu\text{m}$ to $6 \mu\text{m}$, which was used to determine the best-fit model. The lower graph shows the two spectra from $2 \mu\text{m}$ to $20 \mu\text{m}$. A possible explanation for the deviations in the wavelength region $> 10 \mu\text{m}$ is given in the text.

Until now, the comparison between the models and the ISO spectra has been performed with the assumption that V460 Cyg has a solar metallicity. To test this assumption, we compared the ISO spectrum of V460 Cyg to models with a lower metallicity than the solar one ($Z = 0.33 Z_{\odot}$, Fig. 6.5). With this metallicity we used models with $T_{eff} = 2800$ K, $T_{eff} = 3000$ K, $T_{eff} = 3100$ K and $T_{eff} = 3200$ K; $\log(g [cm/s^2]) = 0.00$; $M = 2 M_{\odot}$ and a $C/O = 1.4$. The model spectrum with $T_{eff} = 2800$ K again differs strongly from the ISO spectrum. We again interpolated the $T_{eff} = 3050$ K and the $T_{eff} = 3150$ K spectra from the other models and compared them to the ISO spectra. As a result, the following issues are conspicuous:

- The short wavelength region of the C_2H_2 and HCN band at $3 \mu m$ is reproduced well from the model by $T_{eff} = 3150$ K. On the other hand, the long wavelength end of this feature is stronger and shifted to longer wavelengths. The other models cannot reproduce this feature.
- The C_3 and CO feature is too weak for all the models. Its intensity grows with decreasing temperature. Hence, the model with $T_{eff} = 3150$ K cannot describe this band. A difference to the models with solar metallicity is the absence of the extra depression at wavelengths higher than $4.7 \mu m$ (upper panel in Fig. 6.5)
- At the same model temperature, the C_3 feature is weaker and the C_2H_2 and HCN is stronger at a metallicity of $Z = 0.33 Z_{\odot}$. This dependency of the features is in agreement with the model calculations which were published by Gautschy (2001, [25]).
- The ISO spectrum also shows an excess flux for the models with $Z = 0.33 Z_{\odot}$ in the region $> 5.5 \mu m$
- The band at $4 \mu m$, which is due to C_2H_2 and HCN , increases significantly at the temperatures $T_{eff} = 3050$ K and $T_{eff} = 3000$ K at a metallicity of $Z = 0.33 Z_{\odot}$.
- We conclude that there is no model with $Z = 0.33 Z_{\odot}$, $C/O = 1.4$, $M = 2 M_{\odot}$ and $\log(g [cm/s^2]) = 0.00$ which describes the overall shape and the absorption features of the observed ISO spectrum.

We do not have models with a metallicity of $Z = 0.33 Z_{\odot}$ which have other parameters than $C/O = 1.4$, $M = 2 M_{\odot}$ and $\log(g [cm/s^2]) = 0.00$. Therefore, we discuss the changing of the absorption features by a variation of these parameters using the results of a former study Gautschy (2001, [25]):

- An increase in the C/O ratio leads to stronger features of CN , C_2 and C_3 and to weaker features of CO , HCN , C_2H_2 and CH . It is therefore possible that there is a model with a high C/O ratio (> 1.4) and with $Z = 0.33 Z_{\odot}$ which provides an accurate reproduction of the ISO spectrum.
- A changing of the surface gravity only has little effect on the model spectra. The C_2 , CN , C_2H_2 , HCN and C_3 features slightly decrease and the CO features increase in strength.
- A decreasing $^{12}C/^{13}C$ ratio results in stronger C_2 , CN , C_3 features. The C_2H_2 and HCN features are unaffected by this change.
- Recapitulatory, changes in the effective temperature, the C/O ratio and the $^{12}C/^{13}C$ ratio have a great influence on synthetic spectra. In contrast, variations in mass and gravitational acceleration only have small effects on model spectra.

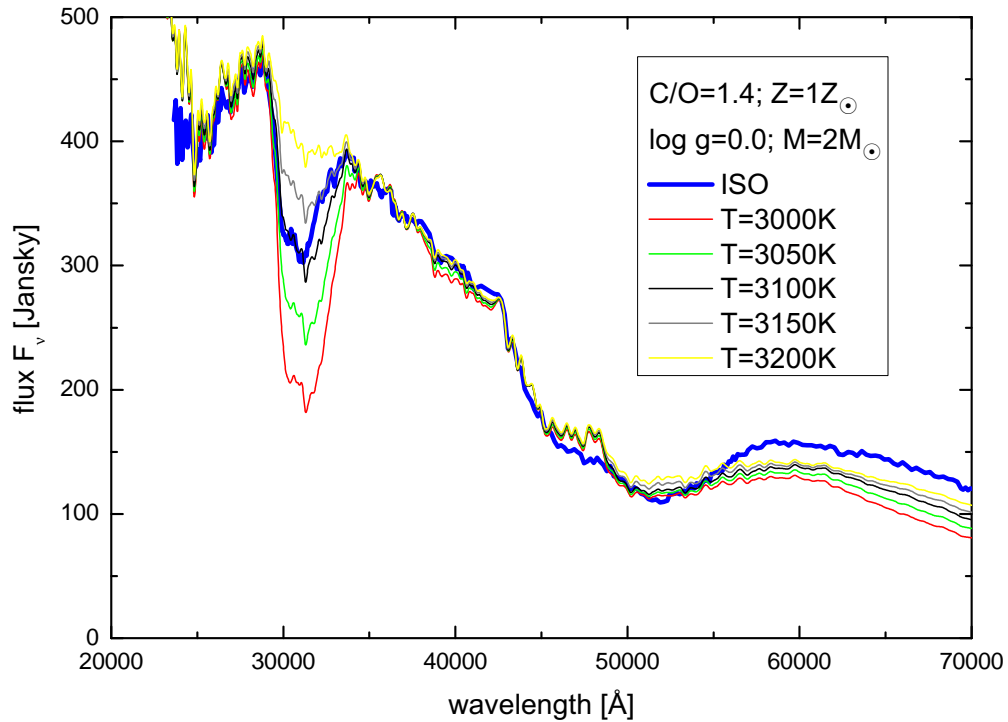
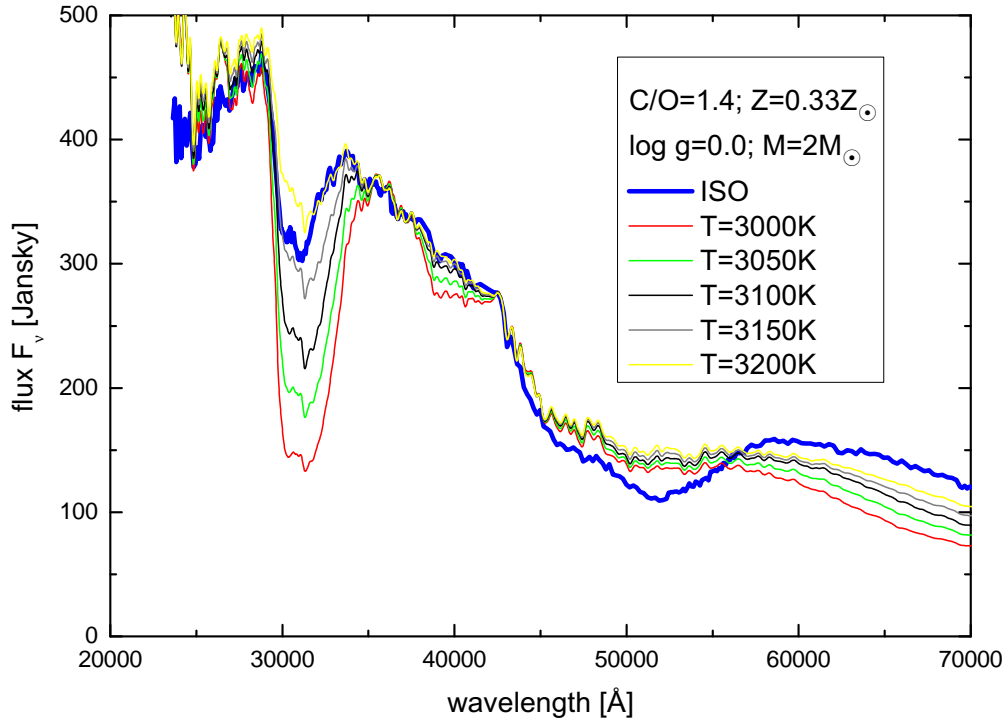


Figure 6.5: Comparison between models ($T_{eff} = 3000\text{ K} - 3200\text{ K}$ in steps of $\Delta T = 50\text{ K}$; $\log(g [cm/s^2]) = 0.00$; $M = 2M_{\odot}$; $C/O = 1.4$) with different metallicities and the ISO spectrum. The upper graph shows the models with a metallicity of $Z = 0.33Z_{\odot}$. The lower graph shows the ones with solar metallicity ($Z = 1Z_{\odot}$). The thick blue line represents the ISO spectrum. There is no model with 1/3 of the solar metallicity which describes the dominant absorption features in this region (the C_2H_2 and HCN feature at $3\mu\text{m}$ and the C_3 feature at $5\mu\text{m}$).

We briefly discuss the assumption of solar metallicity for V460 Cyg with respect to the variation of the chemical abundance in the Milky Way in time and space: The evolution of the metallicity abundance (ϵ) with age is in the order of $\Delta \log \epsilon \approx 0.5$ dex in 10^{10} years in the Milky Way (Unsöld & Baschek ((2002), [71])). The metallicity gradient in the galactic disk decreases with increasing distance from the galactic centre and has a dimension of $d \log \epsilon / dR \approx -0.05$ dex/kpc at the present epoch (Unsöld & Baschek (2002, [71])). The distance of V460 Cyg from the sun is approximately 0.5 kpc. Hence, the metallicity gradient has only a marginal influence at this distance. An age estimation of V460 Cyg is not possible due to the fact that the mass determination of AGB stars is very uncertain. Therefore, we cannot estimate the deviation of the metallicity abundance to the solar metallicity because of the unknown age compared to the sun. The star cannot be compared to isochrones in a Hertzsprung-Russel-diagram due to its unknown mass.

In a recent study, Jørgensen et al. (2000, [36]) derived the parameters of V460 Cyg from a comparison of the ISO spectrum to hydrostatic model atmospheres. Depending on which value of $K_P(C_3)$ was used, the authors found the following model parameters as a good fit to the observed ISO spectrum:

T_{eff} [K]	$\log g$ [cm/s^2]	C/O
2900	-1.5	1.1
3000	-0.5	1.2
3100	-0.5	1.023
3100	0.0	1.2

Table 6.1: Model parameters of V460 Cyg in the study of Jørgensen et al. (2000, [36]).

In that work, plane parallel models were used because of a better comparability to former studies. The best-fit model of V460 Cyg in our study has the parameters $T_{eff} = 3075$ K, $\log(g [cm/s^2]) = -0.50$, $M = 2 M_{\odot}$, $Z = Z_{\odot}$ and a $C/O = 1.4$. The temperature and the gravitational acceleration are in good agreement with the 4th model in Tab. 6.1, which has the parameters $T_{eff} = 3100$ K, $\log(g [cm/s^2]) = 0.00$ and a $C/O = 1.2$. The C/O value of this model is rather different compared to our best-fit model. A possible explanation of this deviation is the difference between plane parallel and spherical models. We attribute the deviations in the C/O ratio to the differences between spherical and plane parallel models.

For lower temperatures Jørgensen et al. found good fits with lower gravitational acceleration. A lower gravitational acceleration results in a more extended star and therefore in lower partial pressures of the molecules. The lower partial pressures of the molecules compensate the increasing strength in the features due to the smaller temperatures. However, a $\log(g [cm/s^2])$ of -1.5 (the model with $T_{eff} = 2900$ K) underestimates the luminosity resulting from the Hipparcos parallax and a $\log g$ of 0.0 (the model with $T = 3100$ K) is a bit too high compared to the Hipparcos value (Jørgensen et al. (1992, [38])). The authors conclude that the most likely temperature range for V460 Cyg is from $T_{eff} = 2950$ K to $T_{eff} = 3050$ K. This is in rather good agreement with our result where the temperature of V460 Cyg is $T_{eff} = 3075$ K.

6.3 Model Spectra and Visible Spectra of V460 Cyg

In this section, we compare the model spectra to the observed ones in the visible wavelength range (Fig. 4.1). The Barnbaum spectrum (Barnbaum (1996, [6])) has a resolution

of 1.6 \AA in the wavelength region from 4000 \AA to 5000 \AA . The synthetic spectra have a resolution of 2.2 \AA at 4450 \AA at the short wavelength end and 3.5 \AA at 7000 \AA at the long wavelength end of the Barnbaum spectrum. For a better comparability to the models the Barnbaum spectrum is binned by a factor of 2 and has therefore then a resolution of 3.2 \AA . The Tereshchenko spectrum (Tereshchenko (1999, [65])) has a resolution of 50 \AA (from 3225 \AA to 7575 \AA). We binned the model spectra at exactly these sampling points. The flux at each sampling point is calculated with an arithmetic mean, e.g. the flux at 3225 \AA is the mean of the fluxes from 3200 \AA to 3250 \AA .

These binned model spectra are normalized to the observed ones. This is done in the wavelength region from 5669.5 \AA to 5853.8 \AA because the spectrum there seems to be close to the continuum. The comparison between the observed data and the normalized synthetic spectra is shown in Fig. 6.6 for the Tereshchenko spectrum and in Fig. 6.8 for the Barnbaum spectrum.

Then, the root mean square error obtained from the differences between the observed and the synthetic spectra is calculated after Equ. 6.1 as described in the previous section. The deviations in the resolution of the Barnbaum spectrum compared to the model observations could produce some errors in the calculation of the RMSE. The RMSEs for the models are shown in Fig. 6.7 for the Tereshchenko spectrum and in Fig. 6.9 for the Barnbaum spectrum. The error bars in these figures result from an assumed signal to noise ratio of 50. The relative root mean square error from the Tereshchenko spectrum is $2 - 5 \%$. The value with 2% roughly corresponds to a S/N ratio of 50. The error bars in Fig. 6.7 are therefore a lower limit for the uncertainties of the RMSEs. Unfortunately, we have no information about the uncertainty in the Barnbaum spectrum. However, we also assumed a S/N ratio of 50 to get an idea how big the error bars are in comparison to the RMSEs.

Can we now define a best-fit model from the comparison between the observed and the synthetic spectra as we did before with the ISO observations? We see that the model with the lowest RMSE resulting from the Tereshchenko spectrum is located at a C/O ratio of $1.3 - 1.4$ (Fig. 6.7), the one from the Barnbaum spectrum is at a C/O ratio of $1.2 - 1.3$ (Fig. 6.9). The best-fit model resulting from the ISO spectrum has a C/O ratio of 1.4. This is in agreement with the Tereshchenko spectrum. However, the error bars in Fig. 6.7 are only a lower limit for the uncertainties in the RMSEs. The models with the smallest errors at the other C/O values are within the error bars of the best-fit models at a C/O ratio of $1.3 - 1.4$. Hence, it is problematic to define solely the best-fit model as the one with the smallest RMSE.

A visual comparison between the spectrum of V460 Cyg and the models with $C/O = 1.1$ and $C/O = 1.4$ shows that the first ones reproduce the observed features better. This can be seen very well in the Barnbaum spectrum (Fig. 6.8). Maybe because of the low resolution this effect is not so pronounced in the Tereshchenko spectrum (Fig. 6.6). This does not agree with the ISO spectrum where the best fit model has a C/O ratio of 1.4 (or 1.3 within the error bars). Possible explanations of these differences are:

- The absorption features in the visible spectral range are mainly generated by the C_2 and CN molecules. A decreasing $\log(g)$ or metallicity result in weaker features of C_2 and CN (Gautschy (2001, [25])). Maybe the surface gravity and/or the metallicity of our models are too high. With a lower value of $\log(g)$ or metallicity we need a higher C/O ratio to produce the observed strength of the features. We saw in Sec. 6.2 that it is not likely that the metallicity of V460 Cyg is much smaller than the solar value. A lower $\log(g)$ results in a more extended star. To make a priori assumptions about the gravitational acceleration of V460 Cyg the mass and the

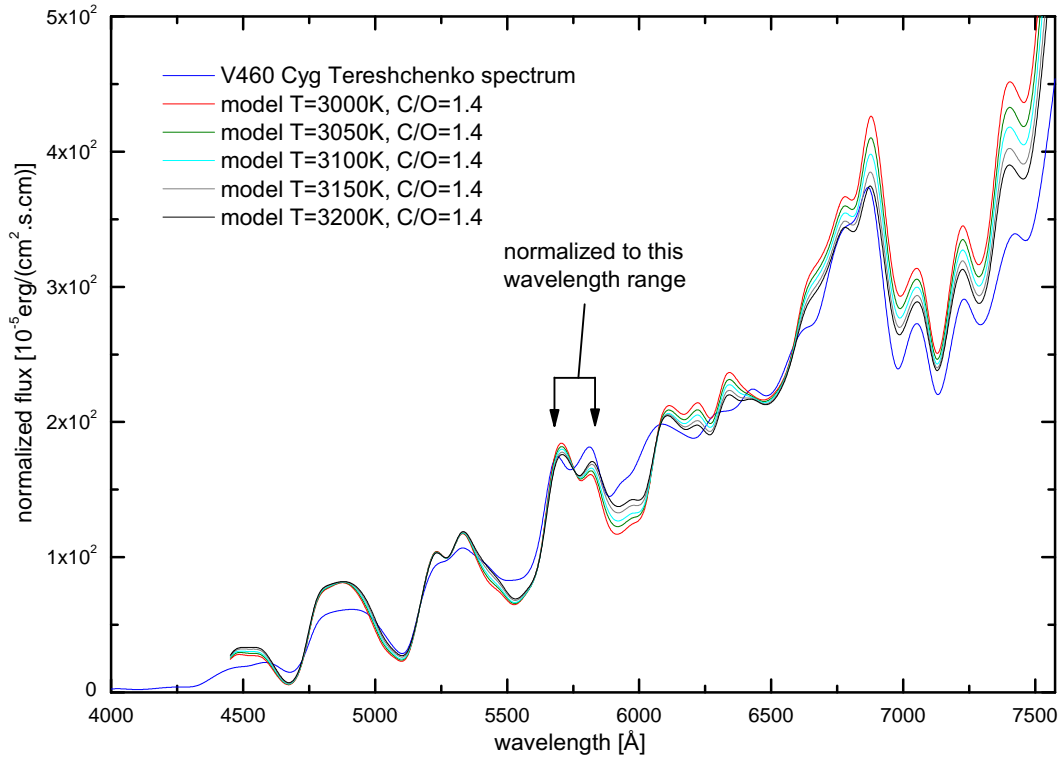
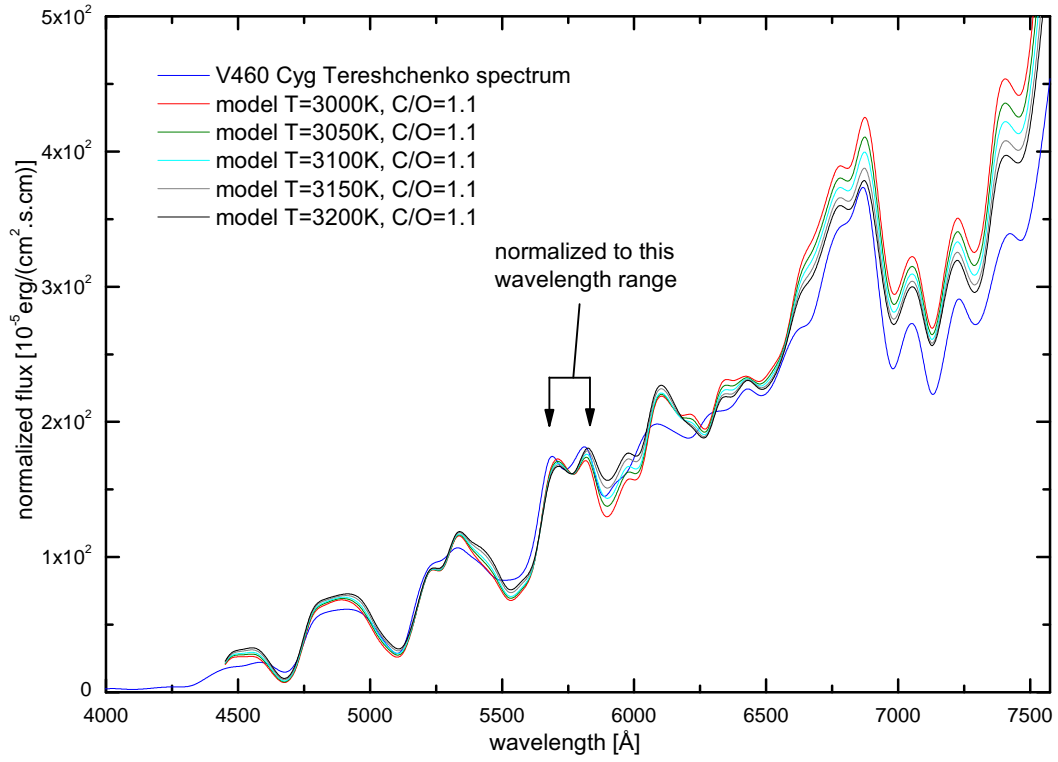


Figure 6.6: Comparison between the Tereshchenko spectrum of V460 Cyg and the interpolated model spectra ($T_{eff} = 3000 \text{ K} - 3200 \text{ K}$ in steps of 50 K , $M = 2 M_{\odot}$, $\log(g [\text{cm}/\text{s}^2]) = -0.5$, $Z = Z_{\odot}$, $C/O = 1.1$, upper graph and $C/O = 1.4$, lower graph).

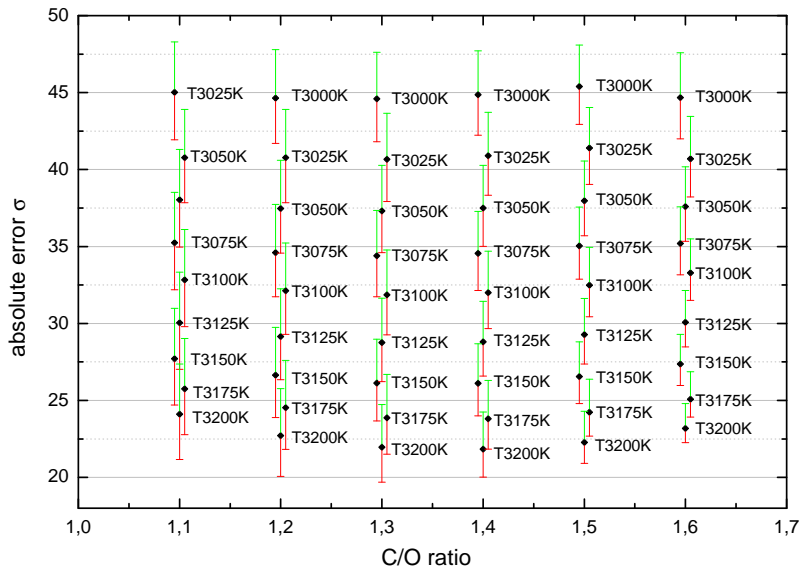


Figure 6.7: Root mean square errors obtained from the differences between the interpolated models (for $T_{eff} = 3000\text{ K} - 3200\text{ K}$ in steps of 50 K, $Z = Z_{\odot}$ and $M = 2M_{\odot}$ and $\log(g [cm/s^2]) = -0.5$) and the Tereshchenko spectrum in the wavelength range of $0.445\ \mu\text{m}$ to $0.7575\ \mu\text{m}$. The error bars are calculated with an assumed S/N ratio of 50.

radius of the star have to be known. The radius of V460 Cyg was determined by Van Belle & Thompson (2000, [72]) by a fit of a uniform disc to the observed visibility and adopting a Hipparcos distance to $333 R_{\odot}$. The main problem in obtaining values of the gravitational acceleration is the determination of the mass. This is in general not easy for single stars and especially very problematic for AGB stars.

- It is a systematic effect that the C/O values determined with a comparison between synthetic and observed spectra are higher in the near infrared than in the visible spectral range. This maybe due to problems concerning the atmospheric structure of hydrostatic models and need to be investigated further.

The trend that the models with a $C/O = 1.1$ fit the visual observations better cannot be seen in the RMSEs of the Tereshchenko spectrum (Fig. 6.7). There, at a given temperature the RMSEs at different C/O ratios have similar values. In the RMSEs of the Barnbaum observations (Fig. 6.9) a slight tendency can be found that the models with a C/O ratio of $1.1 - 1.4$ and with effective temperatures around 3200 K fit the observations better than the models with a C/O of 1.5 and 1.6 . As in the Tereshchenko spectrum the RMSEs at a constant temperature do not show significant differences from $C/O = 1.1$ to $C/O = 1.4$.

When we look at the RMSEs at different temperatures we see another interesting phenomenon: The errors increase with decreasing temperature. The warmer models have the lower RMSEs. This systematic effect occurs at both, the Barnbaum and the Tereshchenko spectra at each C/O ratio (except for the Barnbaum spectrum and the models with $C/O = 1.5$, $T_{eff} = 3025\text{ K}$ and $T_{eff} = 3050\text{ K}$).

In general, a higher model temperature results in weaker absorption features because of the lower partial pressures of the molecules. This behaviour can be seen in Fig. 6.8 and in Fig. 6.6. The features in the models with higher temperatures are more pronounced.

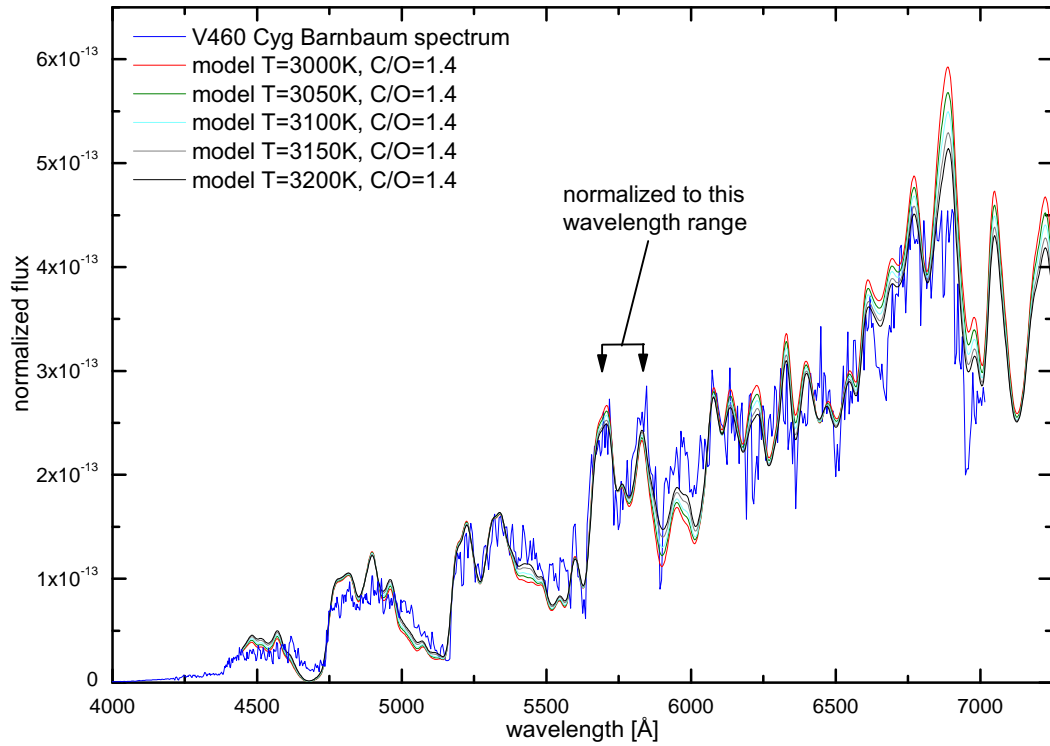
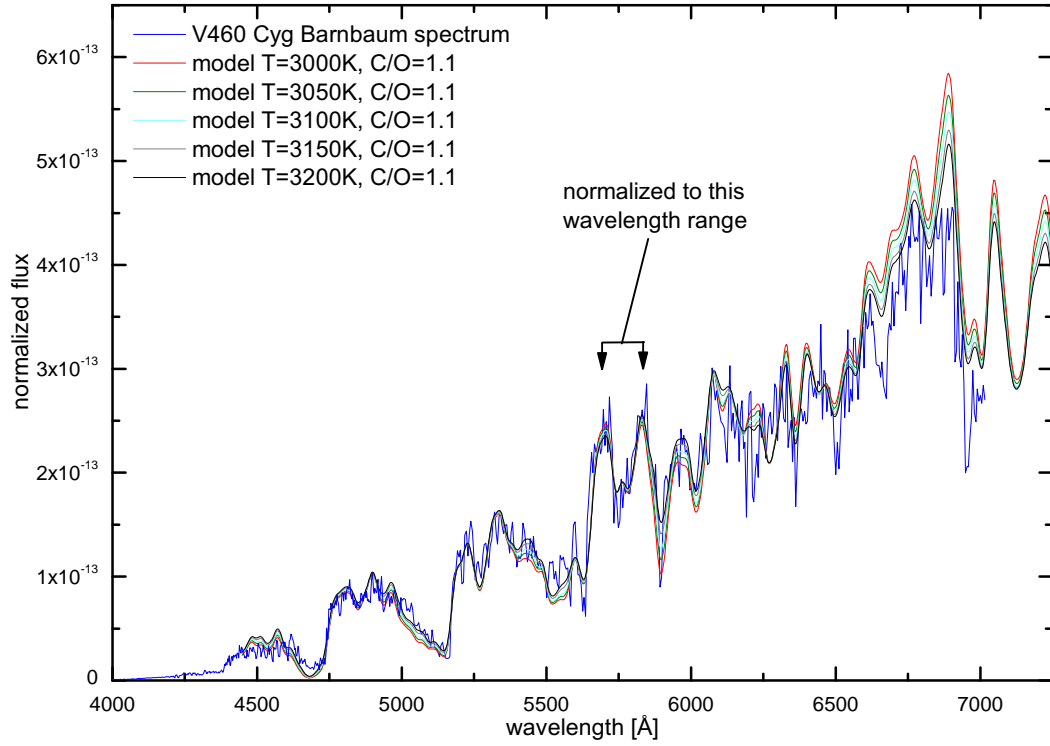


Figure 6.8: Comparison between the Barnbaum observations of V460 Cyg and the interpolated model spectra ($T_{eff} = 3000\text{ K} - 3200\text{ K}$ in steps of 50 K , $M = 2 M_{\odot}$, $\log(g [cm/s^2]) = -0.5$, $Z = Z_{\odot}$, $C/O = 1.1$ (upper graph) and $C/O = 1.4$ (lower graph).

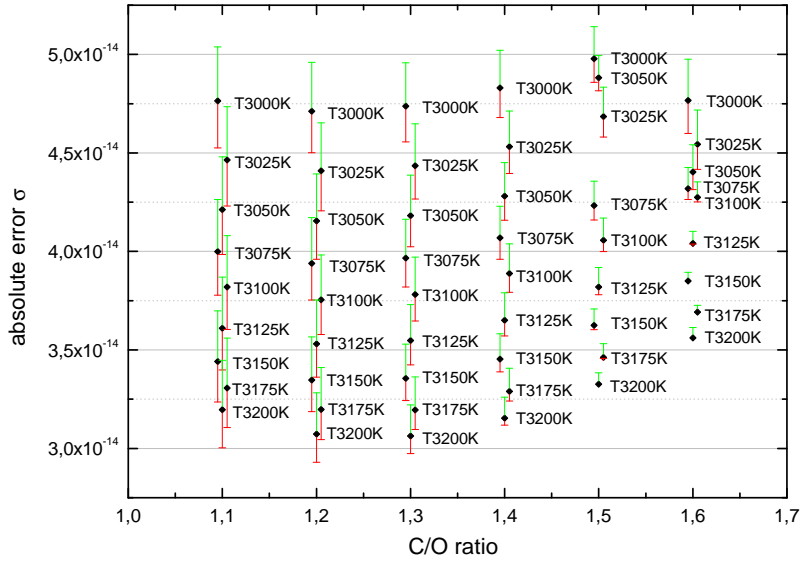


Figure 6.9: Root mean square errors obtained from the differences between the interpolated models (for $T_{eff} = 3000\text{ K} - 3200\text{ K}$ in steps of 50 K , $Z = Z_{\odot}$ and $M = 2M_{\odot}$ and $\log(g) = -0.5$) and the Barnbaum spectrum of V460 Cyg in the wavelength range from $0.4995\ \mu\text{m}$ to $0.7019\ \mu\text{m}$. The error bars are calculated with an assumed S/N ratio of 50.

When we compare the models and the observed spectra, we see that the models reproduce the overall shape of the C_2 and the CN features quite good, but there are deviations at some pseudo-continuum points (especially in the models with low temperatures).

The regions from $4750\ \text{\AA}$ to $5000\ \text{\AA}$ and the peak at $6700\ \text{\AA}$ should be near to the continuum. There, the Tereshchenko spectrum shows a lower flux compared to the models. This difference is very pronounced from $4750\ \text{\AA}$ to $5000\ \text{\AA}$ for the models with a C/O ratio of 1.4 at each temperature. At $6700\ \text{\AA}$, a similar flux excess occurs at both C/O ratios for the models with lower temperatures.

The Barnbaum spectrum shows a flux lower than all the models at the continuum point at $6880\ \text{\AA}$ (at this point, the Tereshchenko spectrum accorded with the model with $T_{eff} = 3025\text{ K}$). The deviations between the models with different temperatures are quite large at this point. The model with $T_{eff} = 3000\text{ K}$ has a significantly higher flux than the observed spectrum compared to the other models considered here. Similar deviations can also be found in other parts of the spectrum (compare the regions at $6770\ \text{\AA}$, $6615\ \text{\AA}$, $6320\ \text{\AA}$ and $6220\ \text{\AA}$). The absorption bands of C_2 and CN , which are dominant in the discussed spectral range, normally increase in strength with decreasing temperatures. This can be seen well at the C_2 bands from $4960\ \text{\AA}$ to $5120\ \text{\AA}$, from $6020\ \text{\AA}$ to $6070\ \text{\AA}$ and at the CN band at $5400\ \text{\AA}$ to $5600\ \text{\AA}$. These features are especially at cooler temperatures and higher C/O ratios stronger in the models than in the Barnbaum spectrum. These two effects (which are not independent of each other), the higher flux in the continuum at $6700\ \text{\AA}$ and the stronger features of the models with lower temperatures are responsible for the systematic effect (the RMSE grows with decreasing temperature at a constant C/O) in the RMSEs which occurs in Figs. 6.7 and 6.9. Another possibility for the differences in the strength of the absorption features can be that the here considered models have too low temperatures. As discussed before, a higher model temperature would result in weaker features. An effective temperature higher than 3200 K is in disagreement with

the parameters obtained from the ISO spectrum. The effective temperatures of V460 Cyg found in the literature (Tab. 4.3) vary from 2840 K to 3230 K. Therefore, it is not likely that this star has a temperature much higher than 3200 K. A systematic study of optical/near infrared fits would be necessary to clarify the differences in the best-fit model parameters.

Lambert (1986, [45]) estimated the C/O ratio of V460 Cyg to 1.062 by a combination of a high resolution near infrared spectrum ($1.5\ \mu\text{m}$ - $2.5\ \mu\text{m}$) and model atmospheres. This value roughly agrees with the fact that the models with $C/O = 1.1$ reproduce the observed Barnbaum spectrum much better than the ones with $C/O = 1.4$. However, it is far away from the C/O ratio derived from the ISO spectrum. The models which are used in the work of Lambert describe the wavelength region of the observed spectra ($1.5\ \mu\text{m}$ - $2.5\ \mu\text{m}$) quite good. For some carbon stars the authors compared their synthetic spectra to the observed ones also at larger wavelengths (up to $10\ \mu\text{m}$). The C_2H_2/HCN and C_3 feature showed strong deviations from the corresponding models. The synthetic features had a much too high band strength. Due to these problems and the results of recent studies that the ratio of the band strength of the C_2H_2/HCN and the C_3 feature is an excellent measurement of the C/O ratio (Jørgensen et al. (2000, [36])), we do not use the C/O value of Lambert (1986, [45]) to define the best-fit model.

6.4 Model Spectra and Visible Spectrum of Z Psc

The only spectrum Z Psc which could be found in the literature is published in the spectral atlas of Barnbaum (1996, [6]). We applied the same procedure as discussed in the previous section to compare this spectrum to the synthetic ones. The RMSEs are shown in Fig. 6.10 and the comparison of the models with $C/O = 1.1$ and $C/O = 1.4$ to the observed spectrum is presented in Fig. 6.11. A very pronounced effect in Fig. 6.10 is that the RMSEs grows with an increasing C/O ratio. The model with the lowest RMSE is the one at with a $C/O = 1.1$. This increase is roughly constant from $C/O = 1.1$ to $C/O = 1.5$ but does not continue at the models with a $C/O = 1.6$. The systematic effect in the temperature that the errors are higher at lower temperatures which has been discussed before connecting to V460 Cyg also appears for Z Psc for the models from $C/O = 1.1$ to $C/O = 1.5$. Another interesting phenomenon occurs at the model with $C/O = 1.6$. The systematic effect in the temperature does not exist anymore. The reason for this could be that this C/O ratio is so far away from reality that the errors resulting from the wrong C/O ratio are much larger than the systematic effect in the temperature. A similar effect can be seen in the RMSEs for V460 Cyg (Fig. 6.9), though it is not so strong in this star. The RMSEs obtained from the differences between the V460 Cyg spectra and the models with $T = 3200\ \text{K}$ are roughly constant within the error bars at a $C/O = 1.1$ to 1.4 and increase for the models with a $C/O = 1.5$ and 1.6. This is another indication that the C/O of V460 Cyg is ≤ 1.4 .

The RMSEs of the Barnbaum Z Psc spectrum implicate that the C/O of Z Psc is somewhere in the range from 1.0 to 1.1. This agrees with the study of Lambert (1986, [45]), where the C/O ratio of Z Psc was determined to be 1.014. As we saw in the last section, the C/O ratios of Lambert differ greatly from the ones estimated with the ISO spectrum. For this reason it is again difficult to use the C/O value of Lambert to restrict the parameters of the best-fit model of Z Psc.

As expected from the RMSEs, also a look at Fig. 6.11 shows that the spectra of the models with $C/O = 1.1$ reproduce the observations much better than the ones with $C/O = 1.4$ (Fig. 6.11). Unfortunately, no ISO spectrum exists for this star. It would be

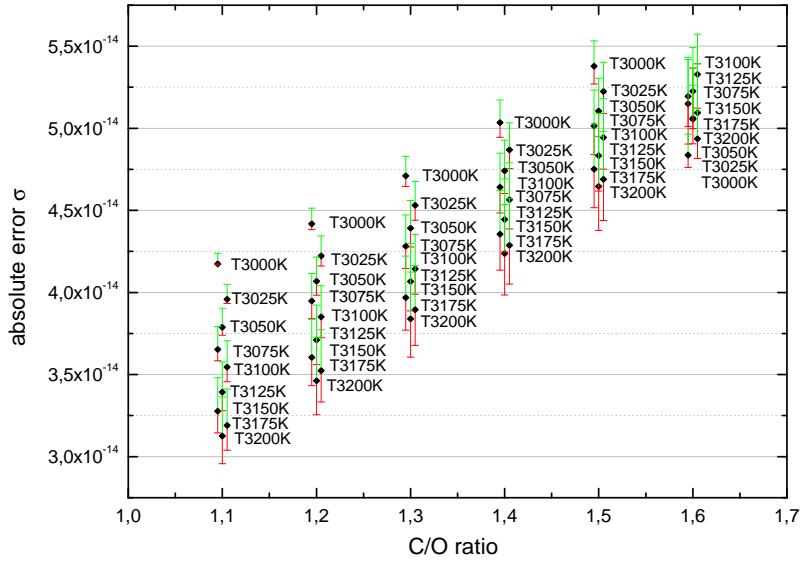


Figure 6.10: Root mean square errors between the interpolated models (for $T_{eff} = 3000 \text{ K} - 3200 \text{ K}$ in steps of 50 K , $Z = Z_{\odot}$ and $M = 2M_{\odot}$ and $\log(g [cm/s^2]) = -0.5$) and the Barnbaum spectrum of Z Psc in the wavelength range of $0.4995 \mu\text{m}$ to $0.7019 \mu\text{m}$. The error bars are calculated with an assumed S/N ratio of 50.

an interesting result if the comparison of the models to a spectrum in the infrared would also result in a higher C/O value than estimated in the visible spectral range (as it does for V460 Cyg).

A temperature estimation for Z Psc with the Barnbaum and the model spectra is not possible because of the systematic effect, that the models with the higher temperatures show the lower RMSE. This effect also occurred for V460 Cyg and was discussed in the last section. The effective temperatures of Z Psc found in the literature (Tab. 4.7) vary from 2870 K to 3240 K . Therefore, it is not likely that this star has a temperature much higher than 3200 K .

6.5 V460 Cyg and Z Psc - Best-Fit Model

The C_2H_2 and HCN feature at $3 \mu\text{m}$ is very sensitive to the parameter range in the temperature range of V460 Cyg. The ratio of the C_3 feature at $5 \mu\text{m}$ to the C_2H_2 and HCN feature at $3 \mu\text{m}$ is a very good measurement of the C/O ratio. For this reason and because of the problems of finding an optimized model from the visible spectra (Sec. 6.3) we defined the best-fit model for V460 Cyg only from the ISO data. It has the following parameters: $T_{eff} = 3075 \text{ K}$, $\log(g [cm/s^2]) = -0.50$, $M = 2M_{\odot}$, $Z = Z_{\odot}$ and a $C/O = 1.4$.

For Z Psc we only have a spectrum in the visible range. From this it follows that the C/O ratio of Z Psc is close to one ($1.0 - 1.1$). A determination of the temperature of Z Psc was not possible due to the reasons discussed in (Sec. 6.3).

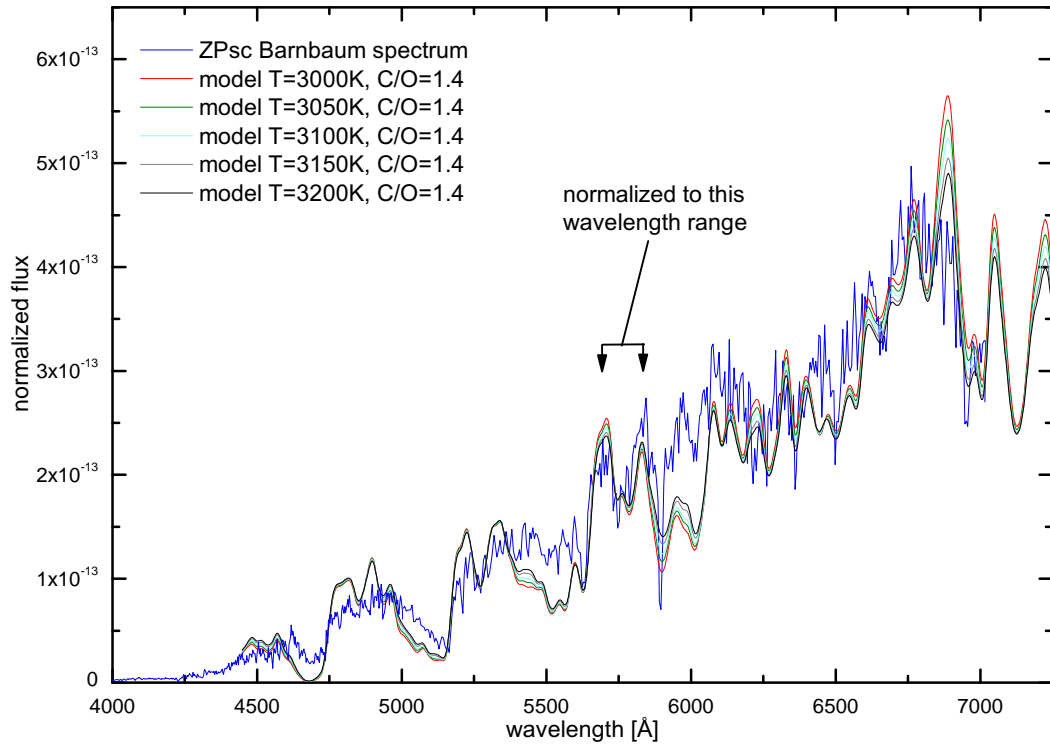
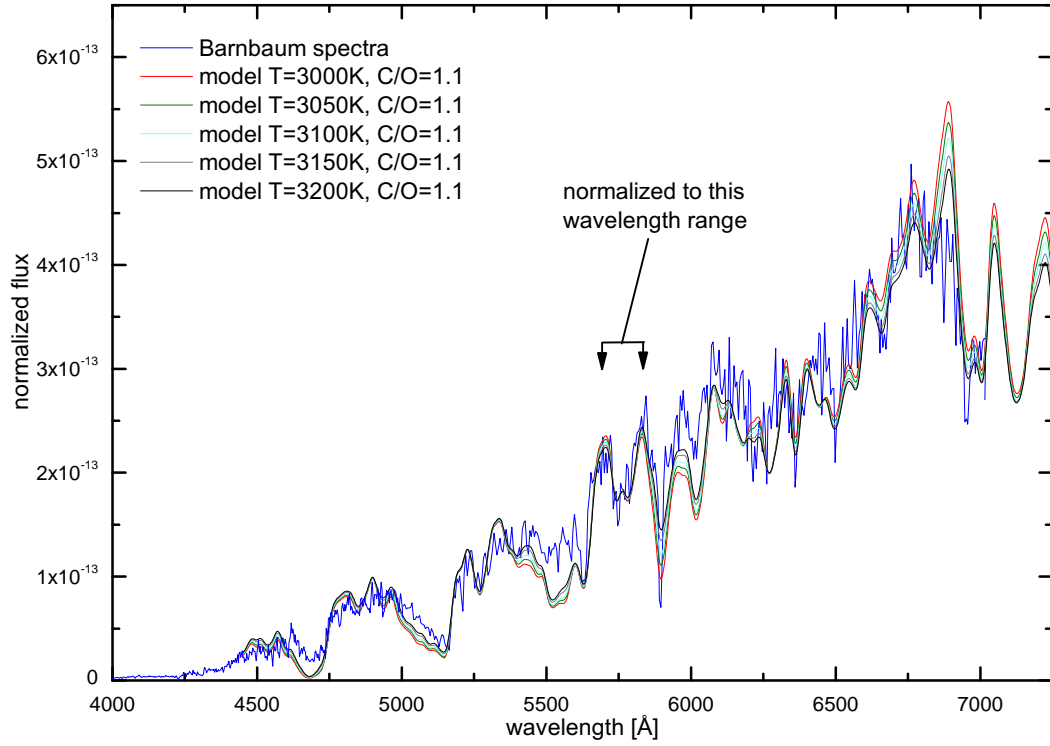


Figure 6.11: Comparison between the Barnbaum spectrum of Z Psc and the interpolated model spectra ($T = 3000\text{K} - 3200\text{K}$ in steps of 50K , $M = 2 M_{\odot}$, $\log(g [\text{cm}/\text{s}^2]) = -0.5$, $Z = Z_{\odot}$, $C/O = 1.1$, upper graph and $C/O = 1.4$, lower graph).

Chapter 7

Comparing Observations and Models

In this section we compare the visibility functions of our hydrostatic models to observed visibilities of V460 Cyg and Z Psc (Figs. 7.1 and 7.2). In the publication of the interferometric measurements of these stars (Dyck et al. (1996, [18])), the spatial frequencies are expressed in units of arcsec^{-1} . In this thesis they are expressed in units of AU^{-1} . They are converted into the unit AU^{-1} using Equ. 5.1 and the Hipparcos distances for V460 Cyg (613.5 pc) and Z Psc (323.6 pc). The exact value of the Hipparcos parallax (Perryman (1997, [55])) for V460 Cyg is 1.63 with a standard deviation of 0.73, the one for Z Psc is 3.08 ± 0.83 . It corresponds to a minimum distance of 423.7 pc and a maximum distance of 1111.1 pc for V460 Cyg (255.1 pc and 442.5 pc for Z Psc respectively). This uncertainty in the distance measurement enters the calculation of the spatial frequency in a linear way. In Figs. 7.1 and 7.2 it is shown as error bars parallel to the x-axis. The error bars in the y-direction result from the uncertainty in the observations and the data reduction. The measured K-band visibility for V460 Cyg is 0.704 ± 0.051 at a baseline of 37.08 m, the one for Z Psc is 0.810 ± 0.123 at a baseline of 38.21 m.

In Ch. 2 we defined as the goal of this thesis if it is possible to describe carbon stars with low pulsation amplitude with hydrostatic model atmospheres and how good the results from the model calculation agrees with observed spectra and with interferometric measurements. For V460 Cyg we came to the following results:

7.1 V460 Cyg

We found a model spectrum which reproduces the observed ISO spectrum of V460 Cyg very well. The ISO spectrum covers the wavelength range from $2.38 \mu\text{m}$ to $45.2 \mu\text{m}$. Because of the sensitivity of the C_2H_2/HCN and the C_3 feature to the temperature and the C/O ratio (cf. Sec. 6.2) we used the region from $2.4 \mu\text{m}$ to $5.6 \mu\text{m}$ to define the best-fit model. It has the parameters $T_{eff} = 3075 \text{ K}$, $\log g = -0.50$, $M = 2 M_\odot$, $Z = Z_\odot$ and a $C/O = 1.4$. The region from $2.4 \mu\text{m}$ to $5.6 \mu\text{m}$ is well reproduced from the best-fit model (Fig. 6.4). At wavelengths longer than $5.5 \mu\text{m}$ some deviations appeared between the ISO observations and the spectrum from the best-fit model. Explanations for these deviations are given in Sec. 6.2. We also compared visible spectra to our model calculations. The absorption features of the observed visible spectra are reproduced well from the model calculations. Nevertheless, some problems occurred by defining the parameters of a best-fit model from the visible spectra. They were discussed in Sec. 6.3 in detail. Based on this discussion we defined the parameters of the best-fit model for V460 Cyg only from the ISO spectrum.

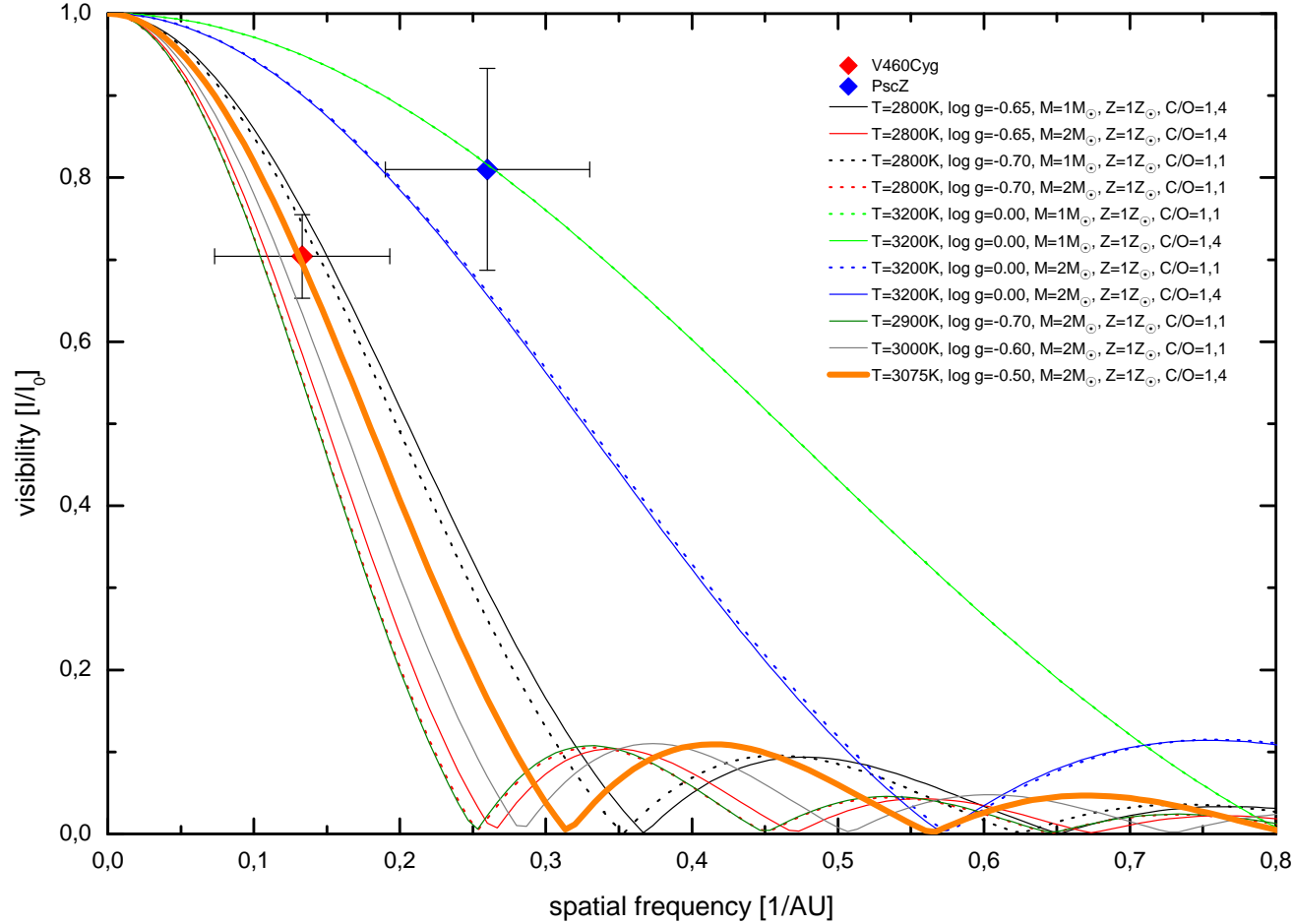


Figure 7.1: Comparison between the model and the observed visibilities for V460 Cyg (red diamond) and Z Psc (blue diamond). The error bars of the observed visibilities in x-direction give the uncertainty in the distance determination from the Hipparcos parallax, the ones in y-direction give the uncertainties in the observations and the data reduction. The visibility function of the best-fit model for V460 Cyg ($T_{eff} = 3075$ K, $\log(g [cm/s^2]) = 0.00$, $M = 2 M_{\odot}$, $Z = Z_{\odot}$ and a $C/O = 1.4$) is shown with an orange line. The agreement between the observed visibility of V460 Cyg and the model visibility function calculated from the intensity distribution of a hydrostatic model is quite good.

The visibility function calculated from the intensity distribution of this model is presented in Fig. 7.1 with an orange line. The observed visibility of V460 Cyg (red diamond in Fig. 7.1) is in very good agreement when we compare it to the visibility function of the best fit model. In Fig. 7.2, the visibility functions of the best-fit model including the effect of bandwidth smearing (Ch. 5.1.1), which has to be considered in the model visibilities when broadband filters are used in observational interferometry, are presented. There, the orange visibility function shows the result of band width smearing in the K-band filter for the carbon star V460 Cyg. The black one gives the visibility without considering this effect. Both are weighted with the K-band filter transmission and the absolute flux of the best-fit model. We see, that the errors in the Hipparcos distance are considerably larger than the effect of bandwidth smearing in the K-band filter for V460 Cyg.

The effective temperatures of V460 Cyg vary from 2840 K to 3230 K in the literature (Tab. 4.3). Excluding the 2 values with the lowest temperatures of V460 Cyg, namely 2840 K, estimated with total fluxes and interferometry (Mendoza & Johnson (1965, [49])) and 2845 K, estimated with the Infrared Flux Method (Tsuji (1981, [67])) because of their rather old publication date, the effective temperatures of V460 Cyg vary from 2950 K to 3230 K. If available, the standard deviations of these estimations range from 147 K to 157 K. Therefore, our derived temperature for V460 Cyg (3075 K) corresponds well with previous studies.

The C/O ratios of V460 Cyg in the literature vary from 1.062 (Lambert (1986, [45])) to 1.2 (Jørgensen (2000, [36])). The deviations to our C/O ratio for V460 Cyg, which was determined to 1.4, have been discussed in Sec. 6.2.

A fact which has to be taken into account is that V460 Cyg is a variable star (variability type SRb). Its pulsation is monophasic with an amplitude of 1.43 mag in the V-filter and it has a period of 180 days (Kiss et al. (1999, [42])). The pulsation of a star is connected with a variation in the radius and the effective temperature. Therefore, also the photospheric spectrum of a star changes its appearance. The parameters of the best-fit model for V460 Cyg are derived for the observation date of the ISO spectrum. To answer the question if V460 Cyg can be described with hydrostatic models doubtlessly, we would need more spectra at different observation times. At least observations in the maxima and minima of the pulsation phase would be required to determine the range of the stellar parameters of this star. Otherwise, the pulsation magnitude of V460 Cyg (1.43 mag) is measured in the V-filter, which has a central wavelength of $0.55 \mu\text{m}$. For cool stars such as carbon stars, this filter is arranged on the Wien-side of the spectrum (Fig. 7.3). Due to its sensitivity to the temperature, a small variation in the temperature has a large effect on the flux value in this wavelength region. This is the reason why the pulsation amplitude of cool stars is much larger in the visible spectral range than in the near infrared. The wavelength region of the ISO spectrum which was used to define the best-fit model of V460 Cyg ($2.4 \mu\text{m} - 5.6 \mu\text{m}$, Fig. 7.3) lies on the Rayleigh-Jeans side close to the flux maximum of the best-fit model. There, a small variation in the temperature due to a pulsation of a star has much lower influence on the total fluxes than on the steep Wien-side of the spectrum. Although no measured pulsation amplitude has been found in the literature in the near infrared, we assume that it is rather low in this region and that the description of V460 Cyg with hydrostatic atmospheres is close to reality.

Considering the good agreement between the model and the observed visibilities and spectra for V460 Cyg, we conclude that hydrostatic models allow a consistent description of two independent observables, namely the spectrum and the intensity profile.

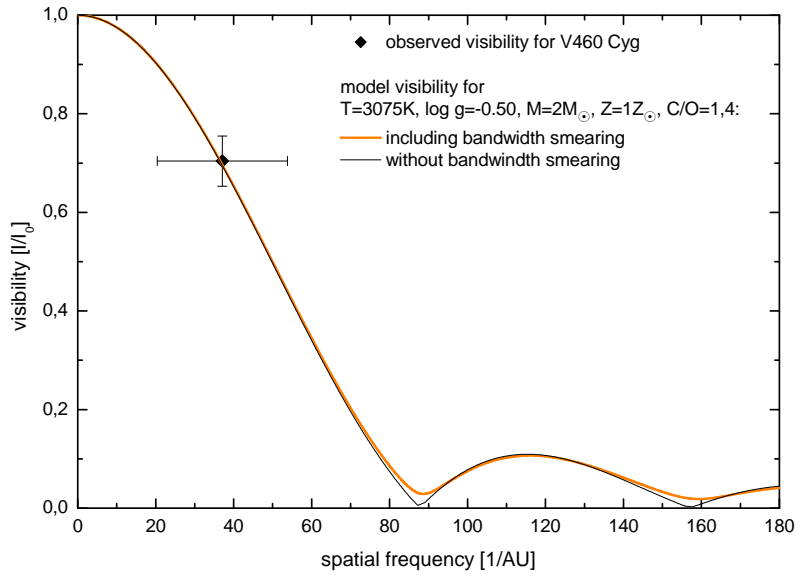


Figure 7.2: Comparison between the visibility function of the best-fit model for V460 Cyg and the observed visibility for V460 Cyg (black diamond). The orange line shows the visibility function including bandwidth smearing, which appears due to the finite filter width of the K-band filter. The black one gives the visibility without this effect.

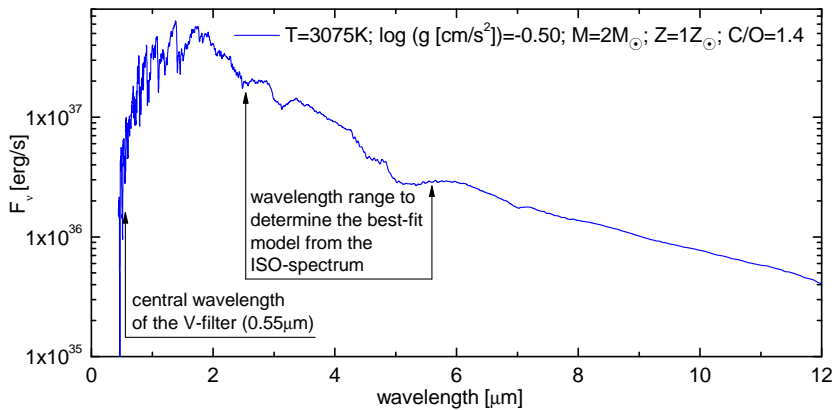


Figure 7.3: Spectrum of the best-fit model of V460 Cyg.

7.2 Z Psc

The 2nd investigated star in this thesis is Z Psc. For this star it was not possible to define a best fit model because of the missing ISO-spectrum. The definition of the best-fit model parameters from a comparison of a visible spectrum for Z Psc to synthetic spectra caused (as it did for V460 Cyg) some problems (Ch. 6.4). Tab. 4.7 gives the temperatures of Z Psc, which can be found in the literature. They range from $T_{eff} = 2870$ K to $T_{eff} = 3240$ K. The temperatures derived from interferometry vary from 3240 ± 239 K to 2913 ± 228 K. The observed visibility of Z Psc (blue diamond in Fig. 7.1) corresponds with the visibility functions of the models with $T_{eff} = 3200$ K, $\log g = 0.00$, $M = 2M_{\odot}$, $Z = Z_{\odot}$ and a $C/O = 1.4$ or $C/O = 1.1$. Nevertheless it is difficult to define stellar parameters of Z Psc only from a comparison of the observed visibility to visibility functions derived from the intensity distributions of hydrostatic model calculations because the absence of the parameters of a best-fit model derived from spectroscopic data and the large error bars in the observed visibility for Z Psc make a unique determination of the parameters of this star problematic.

Bibliography

- [1] *Aringer B., Girardi L., Nowotny W., Marigo P., Lederer M. (2008)*: Synthetic photometry for carbon-rich giants I. Hydrostatic dust-free models, in preparation.
- [2] *Aringer B. (2005)*: Infrared Spectra of Red Giants: Molecular and Atomic Lines, High Resolution Infrared Spectroscopy in Astronomy, Proceedings of an ESO Workshop held at Garching, Germany, 18-21 November 2003. Edited by H.U. Käuffl, R. Siebenmorgen, and A. Moorwood. Garching, Germany, pp. 303-308.
- [3] *Aringer B., Jørgensen U. G., Langhof S. R., Hron J. (2000)*: The SiO Molecule in the Atmospheres and Circumstellar Envelopes of AGB stars, PhD Thesis, Univ. of Vienna.
- [4] *Aringer B., Höfner S., Wiedemann G., Hron J., Jørgensen U. G., Käuffl H. U., Windsteig W. (1999)*: SiO rotation-vibration bands in cool giants II. The behaviour of SiO bands in AGB stars, *A & A*...342..799A.
- [5] *Aoki W., Tsuji T., Ohnaka K. (1998)*: Infrared spectra of carbon stars observed by the ISO SWS. I. Molecular absorption in N-type and SC-type stars, *A & A*...340..222A.
- [6] *Barnbaum C., Stone Remington P. S., Keenan, Philip C. (1996)*: A Moderate-Resolution Spectral Atlas of Carbon Stars: R, J, N, CH, and Barium Stars, *ApJS*..105..419B.
- [7] *Bergeat J., Chevallier L. (2005)*: The mass loss of C-rich giants, *A & A*...429..235B.
- [8] *Bergeat J., Knapik A., Rutily B. (2001)*: The effective temperatures of carbon-rich stars, *A & A*...369..178B.
- [9] *Bessell M. S., Brett J. M. (1988)*: JHKLM photometry - Standard systems, passbands, and intrinsic colors, *PASP*..100.1134B.
- [10] *Bessell M. S., Brett J. M., Wood P. R., Scholz M. (1989)*: Colors of extended static model photospheres of M giants, *A & AS*...77....1B.
- [11] *Blackwell D. E., Shallis M. J. (1977)*: Stellar angular diameters from infrared photometry - Application to Arcturus and other stars, *MNRAS*.180..177B.
- [12] *Blanco A., Borghesi A., Fonti S., Orofino V. (2000)*: On the distance and mass-loss rate of carbon stars showing the silicon carbide emission feature, *A & A*...357..515B.
- [13] *Carleton N. P., Traub W. A., Lacasse M. G., Nisenson P., Pearlman M. R., Reasenberg R. D., Xu X., Coldwell C. M., Panasyuk A., Benson J. A., and 5 coauthors (1994)*: Current status of the IOTA interferometer, *SPIE*.2200..152C.

- [14] *Claussen M. J., Kleinmann S. G., Joyce R. R., Jura M. (1987):* A flux-limited sample of Galactic carbon stars, *ApJS*...65..385C.
- [15] *Cristallo S., Straniero O., Lederer M. T., Aringer B. (2007):* Molecular Opacities for Low-Mass Metal-poor AGB Stars Undergoing the Third Dredge-up, *ApJ*...667..489C.
- [16] *Cutri R. M., Skrutskie M. F., van Dyk S., Beichman C. A., Carpenter J. M., Chester T. Cambresy L., Evans T., Fowler J., Gizis J., and 15 coauthors (2003):* 2MASS All Sky Catalog of point sources, The IRSA 2MASS All-Sky Point Source Catalog, NASA/IPAC Infrared Science Archive. <http://irsa.ipac.caltech.edu/applications/Gator/>.
- [17] *De Graauw T., Haser L. N., Beintema D. A., Roelfsema P. R., van Agthoven H., Barl L., Bauer O. H., Bekenkamp H. E. G., Boonstra A.-J., Bozhoorn D. R. and 52 coauthors (1996):* Observing with the ISO Short-Wavelength Spectrometer, *A&A*...315L..49D.
- [18] *Dyck H. M., van Belle G. T., Benson J. A. (1996):* Angular Diameters and Effective Temperatures of Carbon Stars, *AJ*....112..294D.
- [19] *Dyck H. M., Benson J. A., van Belle G. T., Ridgway S. T. (1996):* Radii and Effective Temperatures for K and M Giants and Supergiants, *AJ*....111.1705D.
- [20] *Dyck H. M., Benson J. A., Carleton N. P., Coldwell C., Lacasse M. G., Nisenson P., Panasyuk A., Papaliolios C., Pearlman M. R., Reasenberg R. D., and 5 coauthors (1995):* First 2.2 micrometer results from the IOTA interferometer, *AJ*....109..378D.
- [21] *Egan M. P., Leung C. M. (1991):* On the nature of the excess 100 micron flux associated with carbon stars, *ApJ*...383..314E.
- [22] *Falkesgaard J. (2001):* Master thesis, Univ. Copenhagen
- [23] *Fleischer A. J., Gauger A., Sedlmayr E. (1991):* Circumstellar dust shells around long-period variables. I - Dynamical models of C-stars including dust formation, growth and evaporation, *A & A*...266..321F.
- [24] *Freytag B., Steffen M., Dorch B. (2002):* Spots on the surface of Betelgeuse – Results from new 3D stellar convection models, *AN*....323..213F.
- [25] *Gautschy R. (2001):* Spectral variability of carbon stars: A comparison between theory and observations, Dissertation an der Universität Wien.
- [26] *Groenewegen M. A. T., Sevenster M., Spoon H. W. W., Perez I. (2002a):* Millimetre observations of carbon stars. I, *A & A*...390..501G.
- [27] *Groenewegen M. A. T., Sevenster M., Spoon H. W. W., Perez I. (2002b):* Millimetre observations of carbon stars. II, *A & A*...390..511G.
- [28] *Groenewegen M. A. T., Whitelock P. A. (1996):* A revised period-luminosity relation for carbon Miras, *MNRAS*.281.1347G.
- [29] *Gustafsson B., Bell R. A., Eriksson K., Nordlund A. (1975):* A grid of model atmospheres for metal-deficient giant stars. I, *A & A*...42..407.
- [30] *Habing H. J., Olofsson H. (2003):* Asymptotic giant branch stars, New York, Berlin, Springer.

- [31] *Hanson R. B. (1979)*: A practical method to improve luminosity calibrations from trigonometric parallaxes, MNRAS.186..875H.
- [32] *Henry L., Vardya M. S., Bodenheimer P. (1965)*: Studies in Stellar Evolution. III. The Calculation of Model Envelopes, ApJ...142..841H.
- [33] *Hoefner S., Dorfi E. A. (1997)*: Dust formation in winds of long-period variables. IV. Atmospheric dynamics and mass loss, A & A...319..648H.
- [34] *Iben I., Jr. (1981)*: The carbon star mystery - Why do the low mass ones become such, and where have all the high mass ones gone, ApJ...246..278I.
- [35] *Ivezic Z., Elitzur M. (1995)*: Infrared emission and dynamics of outflows in late-type stars, ApJ...445..415I.
- [36] *Jørgensen U. G., Hron J., Loidl R. (2000)*: ISO-SWS spectra of the carbon stars TX Psc, V460 Cyg, and TT Cyg, A & A...356..253J.
- [37] *Jørgensen U. G. (1992)*: Sampling Methods, Revista Mexicana de Astronomía y Astrofísica, 23, 195.
- [38] *Jørgensen U. G., Johnson H. R., Nordlund A. (1992a)*: Effects of sphericity in carbon star atmospheres, A & A...261..263J.
- [39] *Jura M. (1987)*: Mass-losing red giants in open clusters, ApJ...313..743J.
- [40] *Kerschbaum F. (1993)*: Infrared properties of stars on the Asymptotic Giant Branch, Ph.D. thesis, University of Vienna, Austria.
- [41] *Kessler M. F., Steinz J. A., Anderegg M. E., Clavel J., Drechsel G., Estaria P., Faelker J., Riedinger J. R., Robson A., Taylor B. G., Ximénez de Ferrán S. (1996)*: The Infrared Space Observatory (ISO) mission, A & A...315L..27K.
- [42] *Kiss L. L., Szatmáry K., Cadmus R. R., Jr., Mattei J. A. (1999)*: Multiperiodicity in semiregular variables. I. General properties, A & A...346..542K.
- [43] *Knapp G. R., Pourbaix D., Platais I., Jorissen A. (2003)*: Reprocessing the Hipparcos data of evolved stars. III. Revised Hipparcos period-luminosity relationship for galactic long-period variable stars, A & A...403..993K.
- [44] *Labeyrie A., Lipson S. G., Nisenson P., Dejajffe R. (2006)*: An Introduction to Optical Stellar Interferometry, Cambridge University Press.
- [45] *Lambert D. L., Gustafsson B., Eriksson K., Hinkle K. H. (1986)*: The chemical composition of carbon stars. I - Carbon, nitrogen, and oxygen in 30 cool carbon stars in the Galactic disk, ApJS...62..373L.
- [46] *Lawson P. R. (1999)*: Principles of Long Baseline Stellar Interferometry, Course Notes from the 1999 Michelson Summer School August 15 - 19, JPL Publication 00-009 07/00, <http://sim.jpl.nasa.gov/michelson/iss.html>.
- [47] *Lazaro C., Hammersley P. L., Clegg R. E. S., Lynas-Gray A. E., Mountain C. M., Zadrozny A., Selby M. J. (1994)*: Infrared Spectrophotometry of Bright Carbon Stars, MNRAS.269..365L.

- [48] *Marigo P., Bressan A., Chiosi C. (1998):* TP-AGB stars with envelope burning, *A & A...*331..564M.
- [49] *Mendoza E. E., Johnson H. L. (1965):* Multicolor Photometry of Carbon Stars, *ApJ...*141..161M.
- [50] *Michelson A. A. (1920):* On the Application of Interference Methods to Astronomical Measurements, *ApJ....*51..257M.
- [51] *Ohnaka K., Tsuji T. (1998):* Quantitative analysis of carbon isotopic ratios in carbon stars. II. The effect of model atmosphere on the iso-intensity method, *A & A...*335.1018O.
- [52] *Ohnaka K., Tsuji T. (1996):* Quantitative analysis of carbon isotopic ratios in carbon stars. I. 62 N-type and 15 SC-type carbon stars, *A & A...*310..933O.
- [53] *Perrin G., Ridgway S. T., Coudé du Foresto V., Mennesson B., Traub W. A., Lacasse M. G. (2004):* Interferometric observations of the supergiant stars α Orionis and α Herculis with FLUOR at IOTA, *A & A...*418..675P.
- [54] *Percy J. R., Wilson J. B., Henry G. W. (2001):* Long-Term VRI Photometry of Small-Amplitude Red Variables. I. Light Curves and Periods, *The Publications of the Astronomical Society of the Pacific*, 113, 983.
- [55] *Perryman M. A. C., ESA, (1997):* The HIPPARCOS and TYCHO catalogues. Astrometric and photometric star catalogues derived from the ESA HIPPARCOS Space Astrometry Mission, *ESA SP Series*, 1200.
- [56] *Plez B., Brett J. M., Nordlund A. (1992):* Spherical opacity sampling model atmospheres for M-giants. I - Techniques, data and discussion, *A & A...*256..551P.
- [57] *Richichi A. (2005):* CHARM2: An updated Catalog of High Angular Resolution Measurements, *A & A...*431..773R.
- [58] *Richichi A., Calamai G. (2003):* Infrared high angular resolution measurements of stellar sources. VI. Accurate angular diameters of X Cnc, U Ori and Eta Gem, *A & A...*399..275R.
- [59] *Richichi A., Percheron I. (2002):* CHARM: A Catalog of High Angular Resolution Measurements, *A & A...*386..492R.
- [60] *Rowan-Robinson M., Harris S. (1984):* Radiative Transfer in Dust Clouds - Part Four - Circumstellar Dust Shells around Carbon Stars, *MNRAS*.202..797R.
- [61] *Salaris M., Cassisi S. (2005):* Evolution of Stars and Stellar Populations, *Wiley Verlag*.
- [62] *Schöier F. L., Olofsson, H. (2001):* Models of circumstellar molecular radio line emission. Mass loss rates for a sample of bright carbon stars, *A & A...*368..969S.
- [63] *Scholz M., Takeda Y. (1987):* Model study of wavelength-dependent limb-darkening and radii of M-type giants and supergiants, *A & A...*186..200S.
- [64] *Sloan G. C., Kraemer, Kathleen E., Price, Stephan D., Shipman, Russell F. (2003):* A Uniform Database of 2.4-45.4 Micron Spectra from the Infrared Space Observatory Short Wavelength Spectrometer, *ApJS..*147..379S.

- [65] *Tereshchenko V. M. (1999)*: Spectrophotometry of three S stars and thirteen carbon N stars, *Astronomy Reports*, 43, 526.
- [66] *Tsuji T., Ohnaka K., Aoki W., Yamamura I. (1997)*: Warm molecular envelope of M giants and Miras: a new molecule forming region unmasked by the ISO SWS, *A & A...320L...1T*.
- [67] *Tsuji T. (1981a)*: Intrinsic Properties of Carbon Stars I. Effective Temperature Scale of N-type Carbon stars, *Journal of Astrophysics and Astronomy*, 2, 95.
- [68] *Tsuji T. (1981b)*: Intrinsic Properties of Carbon Stars II. Spectra, Colours, and HR diagram of Cool Carbon Stars, *Journal of Astrophysics and Astronomy*, 2, 253.
- [69] *Tsuji T. (1978)*: Atmospheres of red supergiant stars. III. Light scattering in the circumstellar dust shell and its effect upon stellar interferometry, *PASJ...30..435T*.
- [70] *Tsuji T. (1973)*: Molecular abundances in stellar atmospheres. II, *A & A....23..411T*.
- [71] *Unsöld A., Baschek B. (2002)*: *Der neue Kosmos*, 7.Auflage, Springer Verlag.
- [72] *Van Belle G. T., Thompson R. R. (2000)*: Linear Radii and Effective Temperatures of Carbon Stars, 195th Meeting of the American Astronomical Society, Atlanta (publication available in the CHARM catalogue: PartIII: Publications with long-baseline interferometry results).
- [73] *Verhoelst T. (2005)*: Evolved stars: a combined view from interferometry and spectroscopy, PhD Thesis, Leuven.
- [74] *Windsteig W., Dorfi E. A., Hoefner S., Hron J., Kerschbaum F., (1997)*: Mid- and far-infrared properties of dynamical models of carbon-rich long-period variables, *A & A...324..617W*.
- [75] *Wing R. (1992)*: Three-Color Narrow-Band Photoelectric Photometry of Red Variables, *JAVSO..21...42W*.
- [76] *Wittkowski M., Aufdenberg J. P., Kervella P. (2004)*: Tests of stellar model atmospheres by optical interferometry. VLTI/VINCI limb-darkening measurements of the M4 giant ψ Phe, *A & A...413..711W*.
- [77] *Yamamura I., de Jong T., Onaka T., Cami J., Waters L. B. F. M. (1999)*: Detection of warm SO_2 gas in oxygen-rich AGB stars, *A & A...341L...9Y*.
- [78] *Yamashita Y. (1972)*: The C-classification of the spectra of carbon stars, *Ann. Tokyo Astron. Obs*, 13, 169.
- [79] *Yuasa M., Unno W., Magono S. (1999)*: Distance Determination of Mass-Losing Stars, *Publ. of the Astronomical Society of Japan*, 51, 197.

Chapter 8

Appendix

8.1 Interesting Stars for Further Studies

In this chapter we present some further data of the stars listed in Tab. 3.1. We look for stars which can be investigated as we did in our study. Tab. 8.1 lists the variability type, the variability amplitude, the spectral type, the distance and its minimum and maximum error, the parallax and its error, the effective temperature and the period. Tab. 8.2 gives some information about the availability of interferometric measurements and spectroscopic observations. The observed spectra from the ISO-SWS01 are shown in Fig. 8.1 (from 2.44 to 15 μm). They are published in Sloan et al. (2003, [64]) and were taken from the website http://www.iras.ucalgary.ca/~volk/getswspect_plot.html. Fig. 8.2 presents the visible spectra which can be found in Barnbaum et al. (1996, [6]).

Interesting stars for future studies are stars with interferometric observations, observed spectra (particularly ISO-SWS01 spectra) and a small error in the measured parallax. This is the case for the following stars:

- VX And: Available data: Visibility and spatial frequency; ISO-SWS01, ISO-SWS06 and Barnbaum spectra; variability amplitude $\Delta V = 1.50$ mag, parallax= 3.56 ± 1.28 , $T_{eff} = 2455$ K.
- TT Cyg: Available data: An interferometric observation already exists, but only the angular diameter is published; ISO-SWS01 (2x) and ISO-SWS06 spectra; variability amplitude $\Delta B = 1.70$ mag, parallax= 1.96 ± 0.80 , $T_{eff} = 2825$ K.
- Y CVn: Available data: Visibility and spatial frequency; ISO-SWS01, ISO-SWS06, Barnbaum and Tereshchenko spectra; variability amplitude $\Delta P = 2.60$ mag, parallax= 4.59 ± 0.73 , $T_{eff} = 2760$ K.

Investigated Stars

GCVS	type	ampl.	[mag]	spectrum	dist. [pc]	min. [pc]	max [pc]	par. [mas]	T_{eff} [K]	period [days]
AB Ant	Lb	0.10	[V]	C6,3(N0)	301.20	249,38	380,23	3.32 [0.69]	3030	
AC Pup	Lb	1.20	[V]	C5,4(N)	353.36	251,89	591,72	2.83 [1.14]	2675	
AQ And	SR	1.90	[P]	C5,4(NB)	12500.00			0.08 [1.09]	2660	346
AQ Sgr	SRb	2.30	[P]	C7,4(N3)	4761.90			0.21 [0.92]	2790	199,6
AV Tr	Lb	0.70	[P]	C5,5(NB)	462.96	303,03	980,39	2.16 [1.14]		
AX Tr	Lb	1.38	[V]	C5,5(NB)	458.72	359,71	632,91	2.18 [0.60]		
BE CMa	Lb	1.30	[P]	C5,5J(N)	909.09			1.10 [1.11]	2960	
BF Sge	Lb	1.80	[B]	C4,4(N3)				-0.01 [1.34]	2935	
BL Ori	Lb	1.80	[P]	C6,3(NB,TC)	398.41	290,70	632,91	2.51 [0.93]	3035	
CR Gem	Lb	1.20	[B]	C8,3E(N)	323.62	212,31	680,27	3.09 [1.62]	2960	
DR Ser	Lb	2.99	[B]	C6,4(N)	1694.92			0.59 [1.48]	2650	
EL Aur	Lb	0.80	[P]	C5,4(N3)	207.90	149,48	341,30	4.81 [1.88]	2730	
HK Lyr	Lb	1.80	[V]	C6,4(N4)	1369.86			0.73 [0.76]	2620	
HX Gem	Lb	1.50	[P]	C4,4(N)	78.00	63,09	102,15	12.82 [3.03]	2910	
GK Ori	SR	1.50	[V]	C4-5,4-5(N)	480.77	271,74	2083,33	2.08 [1.60]	2430	236
NP Pup	Lb	0.27	[V]	C7,2(N0)	418.41	332,23	564,97	2.39 [0.62]	3090	
NQ Cas	Lb	0.92	[B]	C4,5J(R5)	1785.71			0.56 [1.34]	3685	
RT Ori	SRb	2.10	[P]	C6,4(NB)	286.53	202,84	487,80	3.49 [1.44]	2870	321
RT Cap	SRb	2.80	[P]	C6,4(N3)	561.80	306,75	3333,33	1.78 [1.48]	2480	393
RU Pup	SRb	1.90	[P]	C5,4(N3)	218.34	179,53	278,55	4.58 [0.99]	2680	425
RV Cyg	SRb	1.60	[P]	C6,4E(N5)	2439.02			0.41 [0.84]	2675	263
RV Mon	SRb	2.19	[B]	C4,4-C6,2(NB/R9)	450.45	310,56	819,67	2.22 [1.00]	2910	131
RY Dra	SRb	1.97	[V]	C4,5J(N4P)	487.80	370,37	714,29	2.05 [0.65]	2810	200
RY Mon	SRa	1.70	[V]	C5,5-C7,4:(N5/R)	454.55	310,56	847,46	2.20 [1.02]	2440	455
S Sct	SRb	1.27	[B]	C6,4(N3)	395.26	291,55	613,50	2.53 [0.90]	2755	148
ST Cam	SRb	2.80	[P]	C5,4(N5)	2777.78			0.36 [0.84]	2805	300
SX Sco	SR	0.90	[P]	C5,4(N3)	363.64	239,81	751,88	2.75 [1.42]	2785	
SY Eri	SRb	1.00	[P]	C6,3(N0)				-0.46 [1.32]		96
T Cnc	SRb	2.90	[V]	C3,8-C5,5(R6-N6)	6666.67			0.15 [1.18]	2405	482
T Ind	SRb	1.70	[P]	C7,2(NA)	571.43	392,16	1052,63	1.75 [0.80]	2990	320
T Lyr	Lb	1.76	[V]	C6,5(R6)	632.91	429,18	1204,82	1.58 [0.75]	2310	
T Mus	SRb	2.60	[P]	C(NP)	1724.14			0.58 [0.72]	2830	93
TT CVn	SRb	0.71	[B]	C3,5CH(R6P)				-0.68 [1.34]	3865	105
TT Cyg	SRb	1.70	[B]	C5,4E(N3E)	510.20	362,32	862,07	1.96 [0.80]	2825	118
TT Tau	SRb	2.00	[P]	C4,2-C7,4(N3)	1282.05			0.78 [1.20]	3090	166,5
TV Lac	Lb	0.80	[P]	C4,5(N3)	534.76	361,01	1030,93	1.87 [0.90]	3290	
TW Hor	SRb	0.43	[V]	C5,5J(R8)	403,23	328,95	520,83	2.48 [0.56]	2950	158
TW Oph	SRb	2.20	[P]	C5,5(NB)	280.11	203,67	448,43	3.57 [1.34]	2440	185
TX Psc	Lb	0.41	[V]	C7,2(N0)(TC)	233.10	191,57	297,62	4.29 [0.93]	3125	
U Ant	Lb	1.60	[P]	C5,3(NB)	256.41	218,82	309,60	3.90 [0.67]	2810	
U Aps	Lb	0.60	[P]	C(NB)	1694.92			0.59 [0.91]	2605	
U Cam	SRb	1.80	[P]	C3,9-C6,4E(N5)	1265.82			0.79 [1.35]	2695	400
U Hya	SRb	2.40	[B]	C6,5,3(N2)(TC)	161.81	144,30	184,16	6.18 [0.75]	2965	450
UU Aur	SRb	2.17	[B]	C5,3-C7,4(N3)	555.56	383,14	1010,10	1.80 [0.81]	2760	234
UV Aql	SRa	1.30	[P]	C5,4-5(N4)				-0.12 [0.95]	2700	385
UX Cen	SRb	0.50	[P]	C(NB)	398.41	288,18	645,16	2.51 [0.96]	2925	122
UX Dra	SRa	1.16	[V]	C7,3(N0)	571.43	440,53	813,01	1.75 [0.52]	3090	168
V1942 Sgr	Lb	0.26	[V]	C6,4(N2/R8)	396.83	299,40	588,24	2.52 [0.82]	2960	
V Aql	SRb	1.80	[V]	C5,4-C6,4(N6)	370.37	275,48	564,97	2.70 [0.93]	2700	353
V Pav	SRb	1.90	[P]	C6,4(NB)	301.20	240,96	401,61	3.32 [0.83]	2545	225,4
VX And	SRa	1.50	[V]	C4,5(N7)	280.90	206,61	438,60	3.56 [1.28]	2455	369
VY UMa	Lb	1.13	[V]	C6,3(N0)	347.22	283,29	448,43	2.88 [0.65]	2930	
W CMa	Lb	1.55	[V]	C6,3(N)	2272.73			0.44 [0.82]	2960	
W Sex	SR	2.20	[B]	C6,3E(NBE)	389.11	260,42	769,23	2.57 [1.27]	3305	134
WW Cas	Lb	2.60	[V]	C5,5(N1)	371.75	199,60	2702,70	2.69 [2.32]	2750	
WZ Cas	SRb	2.00	[P]	C9,2JLI(N1P)	787.40	507,61	1754,39	1.27 [0.70]	3095	186
X Cnc	SRb	1.90	[V]	C5,4(N3)	1111.11			0.90 [1.01]	2645	195
X Vel	SR	1.23	[B]	C4-5,4-5(NB)	526.32	371,75	900,90	1.90 [0.79]	2700	140
Y CVn	SRb	2.60	[P]	C5,4J(N3)	217.86	187,97	259,07	4.59 [0.73]	2760	157
Y Pav	SRb	1.70	[P]	C7,3(N0)	362.32	288,18	487,80	2.76 [0.71]	2945	233
Y Tau	SRb	2.70	[V]	C6,5,4E(N3)	268.82	166,39	699,30	3.72 [2.29]	2735	241

Table 8.1: List of the investigated stars. These carbon stars are selected from the AGB database (Kerschbaum (1993, [40])) up to a variability amplitude of 3 mag. The GCVS name is the star's name in the general catalogue of variable stars, type is the variability type, ampl. is the variability amplitude in the B ([B]), V ([V])-filter or the photometric amplitude ([P]), spectrum is the carbon star spectral classification, dist. is the distance in parsec, min. and max. give the minimum and maximum distance calculated from the error of the Hipparcos parallax, par. is the parallax in milliarcseconds with its error in the squared brackets, T_{eff} is the effective temperature (taken from Bergeat et al. (2001, [8])) and the last column gives the period in days.

Investigated Stars

GCVS	comments	ISO	Barnbaum	Tereshchenko
AB Ant				
AC Pup			yes	
AQ And	Vis + sp. Fr.		yes	
AQ Sgr			yes	
AV Tr				
AX Tr				
BE CMa				
BF Sge				
BL Ori	only Θ available		yes	yes
CR Gem	only Θ available			
DR Ser				
EL Aur			yes	
GK Ori			yes	
HK Lyr	only Θ available			
HX Gem				
NP Pup				
NQ Cas			yes	
RT Cap				
RT Ori			yes	
RU Pup				
RV Cyg	Vis + sp. Fr.			
RV Mon				
RY Dra		SWS01		
RY Mon				
S Sct		SWS01, SWS06, sp.	yes	yes
ST Cam				
SX Sco				
SY Eri				
T Cnc			yes	
T Ind		SWS01 (3x)		
T Lyr		SWS06 (2.44 – 45.2 μm)	yes	
T Mus				
TT CVn		SWS01		
TT Cyg	only Θ available	SWS01 (2x), SWS06		
TT Tau			yes	
TV Lac			yes	
TW Hor				
TW Oph			yes	
TX Psc	not spherical	SWS01 (2x), SWS06 43.01 – 195.88 μm		yes
U Ant				
U Aps				
U Cam		SWS01		
U Hya			yes	yes
UU Aur			yes	yes
UV Aql				
UX Cen				
UX Dra				
V1942 Sgr			yes	
V Aql		SWS01, SWS06		yes
V Pav				
VX And	Vis + sp. Fr.	SWS01, SWS06	yes	
VY UMa				yes
W CMa			yes	
W Sex				
WW Cas				
WZ Cas		SWS06 (2.44 – 45.2 μm)		
X Cnc	Vis + sp. Fr.		yes	yes
X Vel				
Y CVn	Vis + sp. Fr.	SWS01, SWS06	yes	yes
Y Pav				
Y Tau			yes	yes

Table 8.2: List of the investigated stars. This Table gives some information about the availability of observational data. The column 'comments' shows interferometric data (for references and explanations see Ch. 3). The columns ISO, Barnbaum and Tereshchenko give the information about the existence of spectra. The ISO column shows if a spectrum observed with the Short Wavelength Spectrometer (SWS, de Graauw et al. (1996, [17])) is available (SWS01 stands for the operation mode 01, SWS06 stands for the operation mode 06). If visible spectra have been observed by Barnbaum et al. (1996, [6]) or Tereshchenko (1999, [65]) it is denoted with a 'yes' in the corresponding row.

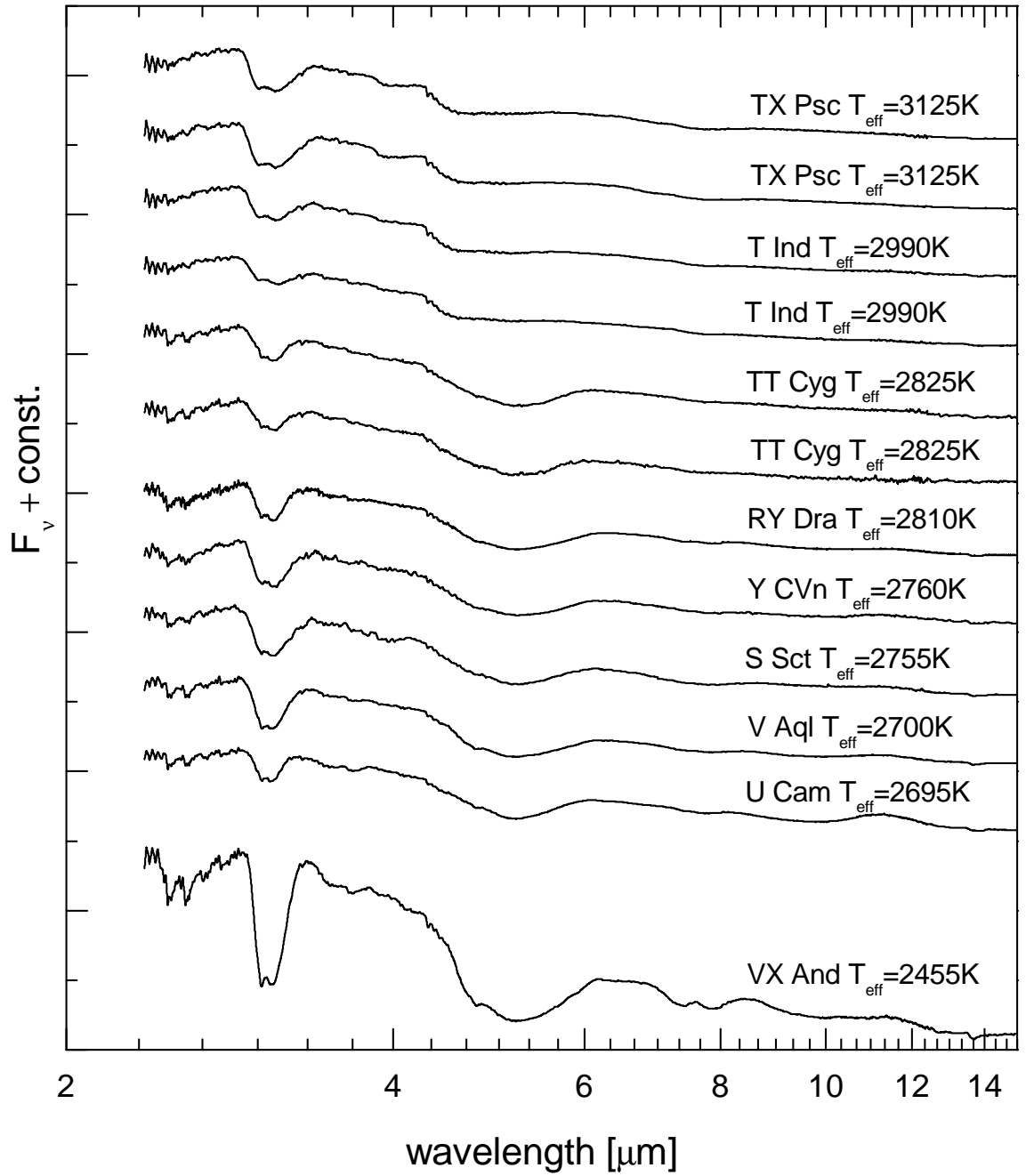


Figure 8.1: ISO-SWS01 spectra of the stars listed in Tab. 8.2, here presented from 2.44 to 15 μm . Also shown are the effective temperatures from Bergeat et al. (2001, [8]).

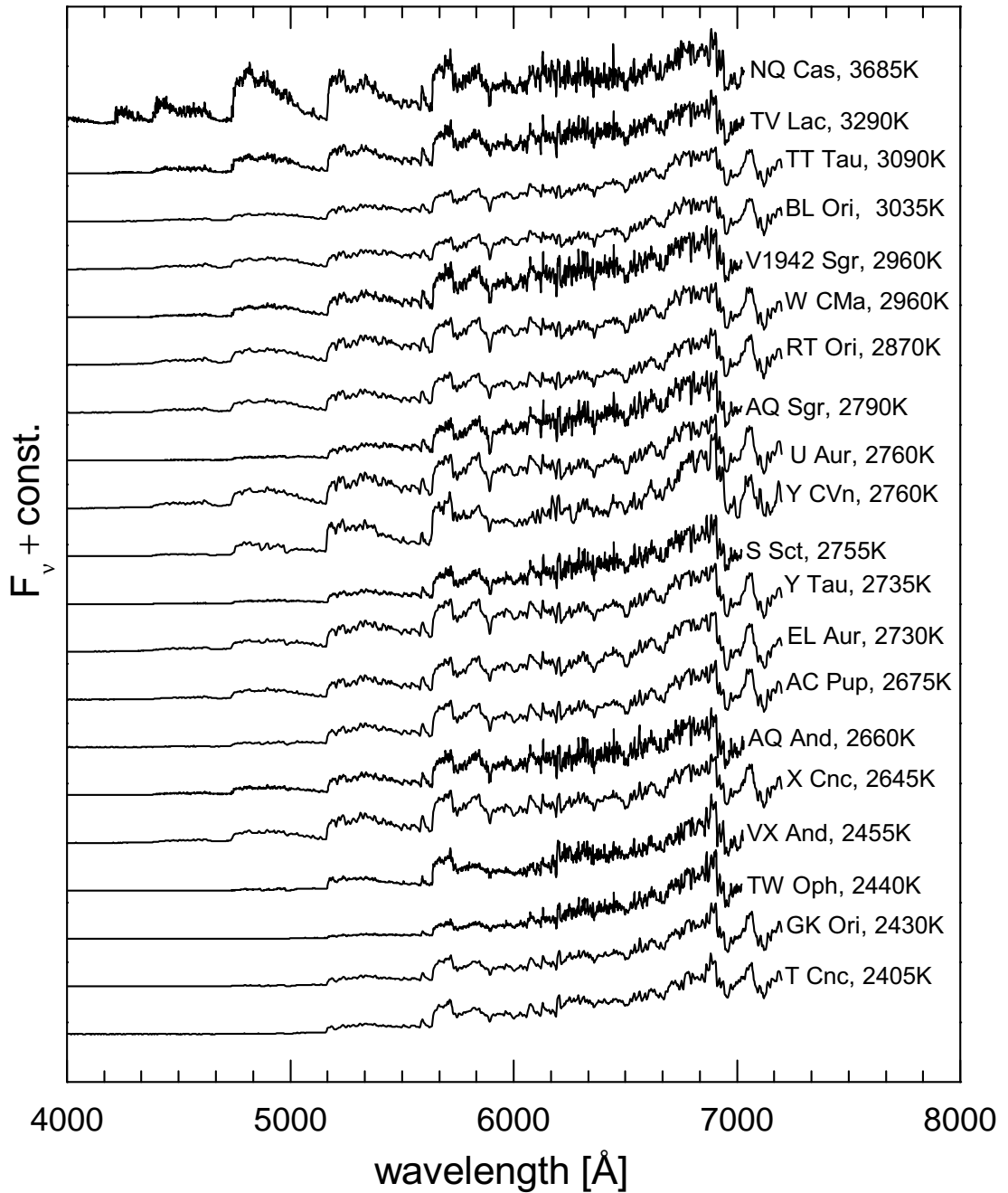


Figure 8.2: Visible spectra (taken from Barnbaum et al. (1996, [6])) of the investigated stars. Also shown are the effective temperatures from Bergeat et al. (2001, [8]).

8.2 Abstract

In this thesis we test the consistency of two different approaches to describe carbon stars. The first method deals with the determination of important parameters of stars (the effective temperature, the surface gravity, the mass and the chemical composition (C/O ratio and metallicity)) by a comparison of observed spectra to synthetic ones. The latter are produced by spherical, hydrostatic COMARCS atmospheres which are based on the MARCS-code. Another output of the model calculation in addition to the synthetic spectrum is the intensity distribution. It gives the wavelength dependent center to limb intensity variation which is needed for the second method. This method uses the interferometric observation of carbon stars. Astronomical interferometers measure the visibility of fringes at a spatial frequency which depends on the baseline and the observed wavelength. The Van-Cittert-Zernike theorem gives the relationship between the visibility function and the intensity distribution. It states that the contrast and the phase of the interference pattern (the visibility) corresponds to the Fourier-transform of the source intensity distribution at the spatial frequencies. Therefore, the visibility functions can be computed as a function of the spatial frequencies by a Fourier transform of the intensity distributions (which are a result of the hydrostatic model calculations). These visibility functions can be compared to observed visibilities.

Carbon stars are located on the asymptotic giant branch in the Hertzsprung-Russell diagram. They are variable stars and they change their state variables and the appearance of their spectra more or less periodic. The larger the variability amplitude of a star, the more the assumption of hydrostatic equilibrium is violated. For this reason our list of investigated carbon stars is limited by a maximum photometric amplitude of 3 mag. The distances of the stars are also required in this study. Hence, another selection criterion was the existence of Hipparcos parallaxes. For the selected carbon stars, the CHARM catalogue was used to search for stars with existing interferometric observations. From the stars with interferometric observations, we chose V460 Cyg and Z Psc to deal with in more detail. For V460 Cyg, spectroscopic observations of the ISO-satellite have been done in the near to middle infrared. Spectra exist for both stars in the visible spectral range. A comparison of the ISO spectrum to our synthetic ones leads to the model best fitting the absorption features and the overall shape of the observed spectra of V460 Cyg. This has the parameters $T_{eff} = 3075$ K, $\log(g [cm/s^2]) = -0.50$, $M = 2 M_{\odot}$, $Z = Z_{\odot}$ and $C/O = 1.4$. The visibility function of this model can be calculated as a Fourier transform of its intensity distribution and then be compared to the observed visibility of V460 Cyg. They are in very good agreement. For V460 Cyg hydrostatic models allow a consistent description of two independent observables, namely the spectrum and the intensity profile.

A comparison of the visible spectra of V460 Cyg and Z Psc to the model spectra showed that the absorption features are reproduced well from the models. Nevertheless, some problems occurred by defining a best-fit model from the visible spectra. Therefore, we could not determine unique parameters for Z Psc. We could only make a restriction in the parameters by a comparison of the observed visibility to the synthetic one.

Furthermore we studied the intensity distributions and the visibility functions of model atmospheres in narrow band filters and the K-broadbandfilter. We demonstrated that different shapes in the intensity distributions have their main influence on the amplitude of the second lobe of the visibility functions. Then we tested different calculations of model visibility functions in broadband filters: 1.) We made a comparison of the K-band model visibilities with and without considering the real transmission profile of the K-band filter in the visibility calculation. 2.) Astronomical interferometers measure squared

visibilities. Therefore we tested the differences if using linear or squared visibilities in the visibility calculation in broad band filters.

Another wavelength dependent effect has to be considered if model visibilities are compared to observed ones: At the baseline of the interferometric observation each monochromatic wavelength in the filter bandwidth induces one visibility function. The resulting visibility function is a superposition of all monochromatic visibility profiles. This effect is called bandwidth smearing. It is shown that the deviations which occur either from the bandwidth smearing or from the different calculations of the model visibilities are much lower than the uncertainties in the interferometric observations.

We also discussed the dependence of some physical quantities like the temperature, the opacity, the density, the gas pressure and the abundances of some important molecules on the atmospheric depth in hydrostatic models. We found that there are correlations between the center to limb intensity variations, the Rosseland opacity and the partial pressure behaviour of C_2H_2 , HCN and C_3 .

8.3 Abstract - German

In dieser Diplomarbeit haben wir zwei unterschiedliche Ansätze zur Beschreibung von Kohlenstoffsternen auf ihre Übereinstimmung überprüft. Die erste Methode behandelt die Bestimmung wichtiger Sternparameter (Effektivtemperatur, Oberflächenbeschleunigung, Masse und chemische Zusammensetzung (C/O Verhältnis und Metallizität)) durch einen Vergleich von beobachteten Spektren mit Synthetischen. Letztere wurden durch sphärische, hydrostatische COMARCS Atmosphären basierend auf dem MARCS-Code generiert. Von den Modellrechnungen erhält man weiters die Intensitätsverteilung eines Sterns. Diese gibt die wellenlängenabhängige Mitte zu Rand Variation der emittierten Strahlung an, welche für die zweite Methode benötigt wird. Dabei handelt es sich um die interferometrische Beobachtung von Kohlenstoffsternen. Astronomische Interferometer messen die Visibility bei einer räumlichen Frequenz, welche von der Basislinie und der beobachteten Wellenlänge abhängig ist. Das Van-Cittert-Zernike Theorem gibt allgemein die Beziehung zwischen der Visibility-Funktion und der Intensitätsverteilung an. Es besagt, dass der Kontrast und die Phase des Interferenzmusters (die Visibility) die Fouriertransformierte der Intensitätsverteilung der Quelle als Funktion der räumlichen Frequenzen ist. Aus den Intensitätsverteilungen ermittelt aus den hydrostatischen Modellrechnungen können daher die Visibility-Funktionen in Abhängigkeit der räumlichen Frequenzen über eine Fouriertransformation ermittelt werden. Diese können mit gemessenen Visibilities verglichen werden.

Kohlenstoffsterne befinden sich am asymptotischen Riesenast im Hertzsprung-Russell-Diagramm. Sie sind variable Sterne und ändern daher ihre Zustandsgrößen und das Aussehen ihres Spektrums mehr oder weniger periodisch. Da die Beschreibung dieser Sterne durch hydrostatische Modelle mit zunehmender Variabilität immer realitätsferner wird, wurden in dieser Arbeit nur Kohlenstoffsterne bis zu einer photometrischen Amplitude von 3 mag untersucht. Ebenso wurden für diese Arbeit die Entfernungen der Sterne benötigt. Ein weiteres Auswahlkriterium war daher das Vorhandensein von Hipparcos-Parallaxen. Die so ausgewählten Sterne wurden im CHARM-Katalog auf das Vorhandensein von interferometrischen Beobachtungen untersucht. Aus den Gefundenen wurden die Sterne V460 Cyg und Z Psc für eine detaillierte Untersuchung ausgewählt. Für den Stern V460 Cyg liegen spektroskopische Beobachtungen des ISO-Satelliten im nahen bis mittleren Infrarot vor. Für beide Sterne existieren Spektren im Sichtbaren. Ein Vergleich des ISO-Spektrums von V460 Cyg mit unseren hydrostatischen Modellatmosphären und anschließender Auswahl des die Absorptionsbanden bzw. den Gradienten des Kontinuums des ISO-Spektrums am besten beschreibenden Modellspektrums lieferte die Parameter des Sterns V460 Cyg ($T_{eff} = 3075\text{K}$, $\log(g [cm/s^2]) = -0.50$, $M = 2 M_{\odot}$, $Z = Z_{\odot}$, $C/O = 1.4$). Aus der Intensitätsverteilung dieses Modells erhält man über eine Fouriertransformation die Visibility-Funktion. Diese wird mit der gemessenen Visibility von V460 Cyg verglichen. Für V460 Cyg zeigt sich eine sehr gute Übereinstimmung dieser Beiden, was die Möglichkeit der Beschreibung dieses Sterns durch ein hydrostatisches Modell grundsätzlich bestätigt.

Beim Vergleich der beobachteten sichtbaren Spektren mit den Modellspektren zeigte sich eine qualitativ gute Übereinstimmung des Verlaufs des Spektrums. Allerdings war die eindeutige Bestimmung der Parameter für V460 Cyg und Z Psc aufgrund gewisser Abweichungen nicht möglich. Daher konnten für Z Psc auch keine eindeutigen Parameter ermittelt werden. Für diesen Stern konnte nur eine gewisse Einschränkung in den Modellparametern durch Vergleich der beobachteten Visibility mit den Synthetischen angegeben werden.

Weiters wurden in dieser Diplomarbeit die Intensitätsverteilungen und die Visibility-

Funktionen von Modellatmosphären in Schmalbandfiltern sowie dem K-Breitbandfilter genauer untersucht. Es wurde gezeigt, dass sich unterschiedliche Formen in den Intensitätsverteilungen hauptsächlich auf die Amplitude des 'second lobes' der Visibility-Funktionen auswirken. Auch wurden die Folgen von unterschiedlichen Berechnungen der Modell-Visibilities in Breitbandfiltern untersucht: 1.) Es wurde ein Vergleich der Visibilities mit bzw. ohne Berücksichtigung des wahren Transmissionsprofils des K-Bandfilters in der Berechnung durchgeführt. 2.) Astronomische Interferometer messen quadratische Visibilities. Daher wurde getestet inwiefern sich die berechneten Modell-Visibilities in Breitbandfiltern unterscheiden, wenn bei der Berechnung entweder quadratische oder lineare monochromatische Visibilities verwendet werden.

Wenn Visibilities (berechnet aus den Intensitätsverteilungen von hydrostatischen Modellen) mit Gemessenen verglichen werden muss ein weiterer wellenlängenabhängiger Effekt berücksichtigt werden: Jede monochromatische Wellenlänge im Filter resultiert bei interferometrischen Messungen in einer Visibility-Funktion. Gemessen wird daher eine Überlagerung dieser Funktionen. Dieser Effekt wird als 'bandwidth smearing' bezeichnet. Es zeigte sich allerdings, dass die Abweichungen die entweder durch das bandwidth smearing oder durch unterschiedliche Berechnungen der Modellvisibilities auftreten, viel geringer sind als der Fehler der aus den Beobachtungen resultiert.

Weiters wurden der Verlauf der Temperatur, der Opazität, der Dichte, des Gasdrucks und der Partialdrücke von in Kohlenstoffsternen wichtigen Molekülen in Abhängigkeit der atmosphärischen Tiefe in hydrostatischen Modellen untersucht. Es stellte sich heraus, dass Korrelationen zwischen der Form der Intensitätsverteilung, der Rosseland Opazität und der Verläufe der Partialdrücke der Moleküle C_2H_2 , HCN und C_3 vorhanden sind.

PERSÖNLICHE DATEN

Name: Schneiderbauer Stefan
Adresse: 4111 Walding, Kreuzweg 20
Geburtstag: 23.06.1979
Handy: 0650/7320755
Email: schneiderbauer@astro.univie.ac.at

AUSBILDUNG

- 03/03-10/08: Studium der Astronomie an der Universität Wien.
Schwerpunktfächer: Stellare Astrophysik, Extragalaktische Astronomie
Diplomarbeitsthema: Carbon Stars, Hydrostatic Models and Optical/Near
Infrared Interferometry
- 10/99-07/06: Studium der Kulturtechnik und Wasserwirtschaft an der Universität für
Bodenkultur, Wien
Schwerpunktfächer: Alpine Naturgefahren, Angewandte Geologie,
Hydrologie
Diplomarbeitsthema: Experimentelle Untersuchung von Murschüben in
einer vertikal drehenden Trommel und in einem Förderband
- 10/05-02/06: Ausbildung zum Sprengbefugten
- 09/93-06/98: HTBLA für Elektrotechnik, Linz
- 09/89-07/93: Stiftsgymnasium Wilhering
- 09/85-07/89: Volksschule Walding

PUBLIKATIONEN

Kaitna R., Rickenmann D., Schneiderbauer, S. (2006): Comparative rheologic investigations in a vertically rotating flume and a "moving-bed" conveyor belt flume, WIT Trans. Ecol. Environ. 90: 89-96

Kaitna R., Rickenmann D., Schneiderbauer, S. (2007): Flow experiments in a rotating drum and a conveyor belt flume, EGU General Assembly 2007, 15.-20.4.2007, Wien

Wien, 12.10.2008